Universidade Federal do Rio Grande – FURG

Instituto de Oceanografia

Programa de Pós-Graduação em Oceanologia

HIDRODINÂMICA, TURBULÊNCIA E MISTURA NA DESEMBOCADURA DA LAGOA DOS PATOS

DÉBORA QUEIROZ GADÊLHA DE BARROS

Tese apresentada ao Programa de Pós-Graduação em Oceanologia, como parte dos requisitos para obtenção do Título de Doutor.

Orientador: *Prof. Dr*. Carlos Augusto Schettini
Universidade Federal do Rio Grande (FURG), Brasil

Co-orientadora: *Prof. Dra*. Lauren Ross
University of Maine, USA

Rio Grande, RS, Brasil

Maio 2026

HIDRODINÂMICA, TURBULÊNCIA E MISTURA NA DESEMBOCADURA DA LAGOA DOS PATOS

Tese apresentada ao Programa de Pós-Graduação em Oceanologia, como parte dos requisitos para obtenção do Título de Doutor.

por

DÉBORA QUEIROZ GADÊLHA DE BARROS

Rio Grande, RS, Brasil

Maio 2026

© A cópia parcial e a citação de trechos desta tese são permitidas sobre a condição de que qualquer pessoa que a consulte reconheça os direitos autorais do autor. Nenhuma informação derivada direta ou indiretamente desta obra deve ser publicada sem o consentimento prévio e por escrito do autor.

B277h Barros, Débora Queiroz Gadêlha de
Hidrodinâmica, turbulência e mistura na desembocadura da lagoa dos patos / Débora Queiroz Gadêlha De Barros. – 2026.
208f.

Tese (Doutorado) – Universidade Federal do Rio Grande – Programa de Pós-Graduação em Oceanologia, 2026.

Orientador: Dr. Carlos Augusto Schettini
Co-orientadora: Dra. Lauren Ross

1.Estuários – Hidrodinâmica 2. Lagoa do Patos (RS). 3. Mistura turbulenta. 4. Estratificação. 5. Plumas fluviais. I. Schettini, Carlos Augusto. II. Ross, Lauren. III. Título

CDU 551.46

Catalogação na fonte: Bibliotecária Doris Santana CRB10/1806

UNIVERSIDADE FEDERAL DO RIO GRANDE - FURG
IO – INSTITUTO DE OCEANOGRAFIA
PROGRAMA DE PÓS-GRADUAÇÃ0 EM OCEANOLOGIA
E-mail: ccpofqg@furg.br – home-page: www.ppgo.furg.br

ATA ESPECIAL DE DEFESA DE TESE DE DOUTORADO – 01/2026

Às quatorze horas do dia vinte e oito de maio do ano dois mil e vinte e seis, no Auditório João Rocha – IO/FURG-Carreiros, reuniu-se a Comissão Examinadora da Tese de **DOUTORADO** intitulada: **"HIDRODINÂMICA, TURBULÊNCIA E MISTURA NA DESEMBOCADURA DA LAGOA DOS PATOS"**, da **Acad. DÉBORA QUEIROZ GADÊLHA DE BARROS.** A Comissão Examinadora foi composta pelos seguintes membros: Prof. Dr. Carlos Augusto França Schettini - Orientador – (PPGO/IO/FURG); Profa. Dra. Lauren Ross – Coorientadora - (University of Maine/USA); Prof. Dr. José Henrique Muelbert. - (IO/FURG); Prof. Dr. Ivan Pérez-Santos – (Universidade de Los Lagos/Chile) e Prof. Dr. Oscar Álvarez-Silva – (Universidad del Norte/Colombia). Dando início à reunião, a Coordenadora do PPGO, Profa. Dra. Grasiela Lopes Leães Pinho, agradeceu a presença de todos e fez a apresentação da Comissão Examinadora. Logo após esclareceu que a candidata teria um tempo de 45 a 60 min para explanação do tema, e cada membro da Comissão Examinadora, um tempo máximo de 30 min para perguntas. A seguir, passou à palavra a candidata que apresentou o tema e respondeu às perguntas formuladas. Após ampla explanação, a Comissão Examinadora reuniu-se em reservado para discussão do conceito a ser atribuído a candidata. Foi estabelecido que as sugestões de todos os membros da Comissão Examinadora, que seguem em pareceres em anexo, foram aceitas pela Orientadora/Candidata para incorporação na versão final da Tese. Finalmente, a Comissão Examinadora considerou a candidata APROVADA, por unanimidade. Nada mais havendo a tratar, foi lavrada a presente ATA, por mim, Clabisnei Moura de Melo – Secretário PPGO, que após lida e aprovada, será assinada pela Comissão Examinadora, pela Candidata e pela Coordenadora do Programa de Pós-Graduação em Oceanologia.

Prof. Dr. Carlos Augusto França Schettini

Profa. Dra. Lauren Ross

Prof. Dr. Ivan Pérez-Santos

Prof. Dr. Oscar Álvarez-Silva

Prof. Dr. José Henrique Muelbert

Acad. Débora Queiroz Gadêlha de Barros

Profª. Drª Grasiela Lopes Leães Pinho
Coordenadora PPGO

Agradecimentos

Primeiramente, agradeço à minha família, meu alicerce e presença constante em todos os momentos da minha vida.

Aos meus pais, por tudo. Por terem me dado oportunidades que eles próprios não tiveram, por sempre incentivarem meus estudos, desde a graduação até o doutorado, e por nunca medirem esforços para que eu pudesse seguir esse propósito. Agradeço também pelo apoio no dia a dia, pela ajuda com meus filhos e com o trabalho, sendo fundamentais para que eu conseguisse chegar até aqui.

Ao meu marido, Gabriel, que estava ao meu lado quando a ideia do doutorado surgiu, ainda como uma semente. Mesmo sabendo de todas as exigências, da dedicação, das ausências e dos desafios que viriam, ele não apenas me apoiou, mas me incentivou desde o início. Esteve presente em todos os momentos, especialmente nos mais difíceis, muitas vezes assumindo ainda mais responsabilidades para que eu pudesse seguir em frente. Este trabalho também é fruto do seu esforço.

Aos meus filhos, Isabela e Henrique, minha maior motivação. São vocês que me impulsionam a querer ser melhor todos os dias e a dar o exemplo de perseverança, superação e paixão pelo conhecimento. Sei que um grande legado foi a experiência ímpar que vivemos como família durante o período do doutorado sanduíche e que aquele ano jamais será esquecido e é parte da história da nossa família. Espero que fique o ensinamento de que, com amor e dedicação, vocês também serão capazes de alcançar seus sonhos. Esta tese é, acima de tudo, para vocês.

Agradeço também às minhas irmãs e cunhados, por todo apoio ao longo dessa etapa, principalmente através das inúmeras visitas que tanto alegraram meu coração e renovaram minha energia para continuar a caminhada. À

Bárbara, em especial, como inspiração sempre, e a todos os familiares que, de alguma forma, contribuíram para que eu chegasse até aqui.

Durante a trajetória acadêmica, reencontrei antigos amigos e conheci muitos outros. Começo agradecendo aos professores Zeca e Mônica Muelbert, que foram meus primeiros contatos, esclarecendo minhas dúvidas iniciais, me apresentando o programa de pós-graduação da FURG e sempre me impulsionando ao longo do doutorado. Assim como aos meus sogros, Lélia e Alcione, que, como oceanógrafos, sempre me apoiaram a prosseguir e celebram essa conquista que hoje se consolida.

Ao meu orientador, Guto Schettini, por ter sido a primeira pessoa a ver algum potencial em mim, mesmo sem eu ter uma formação original em oceanografia. Ele acreditou no que eu seria capaz, me tirou do “vale do desespero” (Dunning–Kruger) e não me deixou desistir. Agradeço imensamente por tudo que me ensinou, pela confiança, pelo incentivo constante e por me tratar hoje como uma colega cientista, com respeito e parceria. Ao longo desse percurso, tornou-se não apenas meu orientador, mas também um grande amigo. Obrigada por acreditar em mim.

À minha coorientadora, Lauren Ross, que me acolheu em outro país, junto com a minha família, ampliando meus horizontes acadêmicos e pessoais. Sua generosidade abriu portas, criou oportunidades e, assim como o Guto, me conectou a uma rede de pesquisadores que hoje fazem parte desse processo. Mais do que isso, tornou-se também uma grande amiga, e levarei essa relação para além da vida acadêmica.

Ao Professor Ivan, cuja parceria começou em uma saída de campo e se fortaleceu ao longo do tempo, culminando na organização do LAPECO no Chile e, hoje, em sua participação como membro da minha banca. Ao Professor Oscar, pelas discussões científicas enriquecedoras, que contribuíram significativamente

para o desenvolvimento deste trabalho e selam esse ciclo com sua participação nesta etapa final.

À minha banca de acompanhamento, Profs. Osmar Möller e Elisa Fernandes, pelas suas valiosas contribuições para esse trabalho, durante as apresentações de Seminários.

À Praticagem da Barra do Rio Grande, pelo apoio fundamental ao longo deste trabalho, viabilizando as campanhas de campo por meio do suporte logístico, disponibilização de embarcação, equipamentos, dados e equipe. Agradeço também pela compreensão e flexibilidade em conciliar as demandas profissionais com o desenvolvimento do doutorado.

Aos meus treinadores, por me ajudarem a manter o equilíbrio físico e mental durante esse processo, oferecendo uma válvula de escape essencial em meio às exigências do doutorado. E também a Vavá, pelo apoio diário, cuidando de mim quando eu mesma não tinha tempo.

A todos os amigos e colegas que, mesmo diante das minhas ausências e do estresse ao longo desse período, estiveram presentes, trazendo suporte e leveza nos bons momentos que pudemos compartilhar para descontrair entre um prazo apertado e outro.

A minha gratidão se estende também a todos que, de alguma forma, contribuíram para a realização deste trabalho, mesmo que não estejam aqui nomeados individualmente. Cada gesto de apoio e incentivo foi fundamental para que eu alcançasse esse objetivo.

Acima de tudo, agradeço a Deus por me conceder saúde e força para percorrer esta jornada. Sou grata por Ele ter me cercado das melhores pessoas possíveis em cada momento: da família onde cresci à que construí com meu marido e filhos. Em cada desafio na vida pessoal, no trabalho e na vida acadêmica, Ele colocou as pessoas certas ao meu lado, e isso faz toda a diferença, pois ninguém faz nada sozinho.

Big whorls have little whorls

Which feed on their velocity,

And little whorls have lesser whorls

And so on to viscosity.

— Lewis Fry Richardson

Table of Contents

AGRADECIMENTOS ..... **IV**

LIST OF FIGURES ..... **X**

LIST OF TABLES ..... **XVIII**

LIST OF ACRONYMS, ABBREVIATIONS, AND SYMBOLS ..... **XX**

CHAPTER I: INTRODUCTION **25**

1.1 The Physics of Estuaries and Mixing 25
1.2 Turbulence: Mechanisms and Theoretical Challenges 27
1.3 Methodological Evolution of Quantifying Turbulence 31
1.4 The Knowledge Gap: Microtidal Systems and the Spatial Evolution of Turbulence 33
1.5 Study Area: The Patos Lagoon Estuary (PLE) 36

CHAPTER II: HYPOTHESIS **40**

CHAPTER III: OBJECTIVES **41**

3.1 General Objective 41
3.2 Specific Objectives 41

CHAPTER IV: MATERIALS AND METHODS **42**

4.1 Observational Strategy 42
4.2 Instrumentation and Data Acquisition 44
4.2.1 Hydrodynamics and water properties 44
4.2.2 Microstructure and Turbulence 45
4.2.3 Environmental Forcing 45
4.3 Data Processing and Analysis 47
4.3.1 ADCP Processing 47
4.3.2 MCTD Processing 48
4.4 Dataset Integration and Derived Parameters 48
4.5 Channel Morphology 50
4.6 Scope and Limitations 52

CHAPTER V: TURBULENCE AND MIXING ALONG A MICROTIDAL AND STRATIFIED ESTUARY-SHELF TRANSITION **53**

5.1. Introduction 56
5.2. Study Area 60
5.3. Materials and Methods 65
5.3.1. Fieldwork Design and Data Collection 65
5.3.2. Data Analysis 69
5.4. Results 77
5.4.1. Environmental Conditions and Inner Channel Dynamics (The Transect Segment) . 77
5.4.2 Estuary–Shelf Transition and Near-Field Plume (The Drift Segment) 80
5.4.3. Adjacent Inner Shelf Baseline (the Jetties Segment) 93

5.5. Discussion 95
5.5.1. Representative Snapshot and Forcing Dominance 95
5.5.2. Morphological Control and Multi-regime Dynamics 96
5.5.3. Hydraulic Regime and Internal Froude Number Analysis 100
5.5.4. Spatial Comparison and Estuarine Context 104
5.5.5. Turbulence and Mixing Processes 108
5.6. Conclusions 111

CHAPTER VI: SPATIAL VARIABILITY OF TURBULENT MIXING IN A HIGHLY STRATIFIED SYSTEM 113

6.1. Introduction 116
6.2. Study Area 119
6.3. Methods 122
6.3.1. Data Collection 122
6.3.2. Field Data Analysis 125
6.4. Results 130
6.4.1. Ambient Conditions 130
6.4.2. Salinity, temperature and density 132
6.4.3. Along-channel and cross-channel velocity 133
6.4.4. Mixing Parameters 135
6.5. Discussion 141
6.5.1. Circulation, Density, and Mixing Variability along the Inlet 142
6.5.2. Consequence of convergence on flow velocity and mixing 151
6.6. Conclusions 152

CHAPTER VII: SUMMARY OF CONCLUSIONS 155

7.1 Main Findings 155
7.2 Broader Implications 158
7.3 Future Perspectives 160

REFERENCES 161

APPENDIX A – MICROSTRUCTURE DATA PROCESSING WORKFLOW 185

A.1 Overview 185
A.2 Understanding MATLAB Functions and General Workflow 186
A.3 Initial Data Inspection and Quality Control 194
A.4 Microstructure Processing and ϵ Estimation 203
A.5 Data Integration and Synchronization with ADCP Measurements (Python) 203
A.6 Computation of Derived Parameters and Visualization 205
A.7 Reproducibility and Data Availability 206

List of Figures

Note: Figures are numbered independently within each chapter. In chapters based on published or submitted articles, they retain their original numbering to preserve consistency with the source material.

Chapter I: Introduction

Figure 1. Global distribution of microtidal estuaries (< 2 m tidal range) discussed in this study. The Patos Lagoon Estuary (Brazil), highlighted in red, is presented as the primary study site. Additional microtidal systems from different regions (e.g., North America, South America, and Europe) are shown in blue to provide a comparative geographical context. The inset highlights European sites for clarity. Tidal classification follows Davies (1964)……..……..34

Figure 2. Study area and sampling design integration. **(a)** Regional setting showing the Patos Lagoon choked system and its connection to the South Atlantic Ocean via the Rio Grande Channel; adapted from Barros et al. (2026). **(b)** Detailed view of sampling stations for Chapter V, including the longitudinal track (Drift), baseline stations near the breakwaters (Jetties), and the cross-channel section (Transect). **(c)** Cross-section positions (T1, T2, and T3) for Chapter VI, including the Rio Grande Pilot Station (source for meteorological and water level data) and distances from the estuary mouth; adapted from Barros et al. (2025). Panel (a) is based on XYZ tiles from Esri National Geographic. Panels (b) and (c) are based on the Brazilian Navy nautical chart No. 2110, available as a GeoTIFF at: https://www.marinha.mil.br/chm/dados-do-segnav/cartas-raster.....38

Chapter IV: Materials and Methods

Figure 1. Methodological scheme for channel morphology analysis. (Left) Spatial distribution of the 57 cross-sections along the main channel. (Right) Example of a reconstructed bathymetric profile used for the wetted area calculation, showing the polygon integration between the bed and the free surface. Bathymetric data were collected in 2024 using a single-beam echosounder and DGPS positioning……51

Chapter V: Turbulence and mixing along a microtidal and stratified estuary-shelf transition

Figure 1: Study area location and sampling design. **(a)** Regional setting showing the Patos Lagoon choked system and its connection to the South Atlantic Ocean via the Rio Grande Channel. **(b)** Detailed view of the estuarine–shelf transition; yellow dots represent the Lagrangian track (Drift), orange dots indicate the baseline stations near the breakwaters (Jetties), and red dots show the cross-channel section (Transect). The green triangle (PS) indicates the Rio Grande Pilot Station, the source for meteorological and water level data. Bathymetric contours and the nautical chart emphasize the jetty-constrained morphology. **(c)** Sampling stations overlaid on a Sentinel-2 true-colour image acquired on 18 July 2022, displaying the turbid surface plume during the survey period. This figure was created using QGIS. Panel (a) is based on the XYZ tiles from Esri National Geographic. Panel (b) is based on Brazilian Navy nautical chart No. 2110, available as a GeoTIFF at: https://www.marinha.mil.br/chm/dados-do-segnav/cartas-raster……..……..….64

Figure 2: Environmental conditions between 15 and 21 July 2022, with the vertical yellow bar representing the survey period. **(a)** Gauged river discharge of the Patos Lagoon (m^3 s^{-1}), **(b)** Water level (m) measured in the channel, where

the three vertical lines indicate the start moment of each section: Drift, Jetties, and Transect. **(c)** Vector plot of wind velocity (m s^{-1}) in meteorological notation, where blue represents southerly winds (blowing towards the north) and red represents northerly winds (blowing towards the south). **(d)** Hovmöller diagram of the along-channel current velocity (m s^{-1}) measured in the channel, where red indicates inflow (flood) and blue indicates outflow (ebb)……79

Figure 3: Cross-sectional distribution of **(a)** along channel current velocity (m s^{-1}; negative values indicate outflow) and **(b)** salinity (g kg^{-1}) at the Transect segment, characterizing the lagoon outflow during the survey.……80

Figure 4. Spatial distributions of **(a)** salinity (g kg^{-1}), **(b)** temperature (ºC), and **(c)** density (kg m^{-3}). The dashed line indicates the interface position between layers. The vertical dotted line marks the position of the mouth (inlet). Distance (km) is measured from the first upstream profile within the channel.……82

Figure 5. Temperature–Salinity (T–S) diagram and frequency histograms of salinity (top) and temperature (right) for the Drift segment. The central panel shows temperature (°C) versus salinity (g kg^{-1}), with dotted vertical lines indicating density anomaly (σ_t) values of 6, 9, 12, 15, and 18 kg m^{-3} (referenced to 1000 kg m^{-3}). The colour bar distinguishes data from the Channel (warm tones) and the Shelf (cold tones), with shading representing the sampling depth (m)....84

Figure 6. Vertical density profiles (kg m^{-3}) across the channel-to-shelf transition. Lines are colour-coded by distance (km) from the starting point of the drift segment. Red tones represent profiles within the inner channel (0-8.5 km) and blue tones represent profiles in the shelf region (9-13.5 km). ……86

Figure 7. Spatial distributions of **(a)** along-channel and **(b)** cross-channel velocity components (m s^{-1}) synchronized with the MCTD profiles. The dashed line indicates the interface position between layers. The vertical dotted line marks the position of the mouth (inlet). Distance (km) is measured from the first upstream profile within the channel.....……..……...……88

Figure 8. Spatial distribution of the turbulent kinetic energy dissipation rate (ϵ, log10(W kg^{-1})). The dashed line indicates the interface position between layers. The vertical dotted line marks the position of the mouth (inlet). Distance (km) is measured from the first upstream profile within the channel.…….……89

Figure 9. Spatial distributions of **(a)** buoyancy frequency (N^2, s^{-2}), **(b)** squared vertical shear (S^2, s^{-2}), and **(c)** gradient Richardson number normalized by its critical value (R_i/0.25). The dashed line indicates the interface position between layers. The vertical dotted line marks the position of the mouth (inlet). Distance (km) is measured from the first upstream profile within the channel. ……..….91

Figure 10. Spatial distributions of **(a)** the vertical eddy viscosity (A_z, m^2 s^{-1}), and **(b)** the buoyancy Reynolds number (Re_b). The dashed line indicates the interface position between layers. The vertical dotted line marks the position of the mouth (inlet). Distance (km) is measured from the first upstream profile within the channel.…….……93

Figure 11. Vertical profiles of **(a)** current velocity (u, m s^{-1}), **(b)** water density (ρ, kg m^{-3}), **(c)** TKE dissipation rate (ϵ, W kg^{-1}), and **(d)** vertical eddy viscosity (A_z, m^2 s^{-1}) at the three baseline stations in the Jetties segment. Green, blue, and yellow lines represent Stations 1 (outermost), 2 (intermediate), and 3 (innermost), respectively. The x-axis tick labels in panels (c) and (d) indicate the logarithmic exponents. ……..…..……..95

Figure 12. Longitudinal distribution of depth-average TKE dissipation rate (log 10 (ϵ), W kg^{-1}) and channel cross-sectional area (m^2) as a function of distance. The red line (left Y-axis) represents the average dissipation rate, while the blue line (right Y-axis) indicates the cross-sectional area along the Drift segment. The dotted vertical line marks the initial channel widening, and the dash-dotted vertical line indicates the maximum constriction point (mouth) at the estuary–shelf interface. ……..98

Figure 13. Two-layer parameters and Internal Froude Number as a function of distance. The figure consists of four vertical panels: **(a)** Vertical density gradient ($\Delta\rho$, kg m^{-3}) across depth; **(b)** Layer velocities, displaying the horizontal velocity (U, m s^{-1}) for upper (U_1) and lower (U_2) layers; **(c)** Layer velocity difference (ΔU, m s^{-1}); and **(d)** Pycnocline depth (h_1, m, right axis) and the Internal Froude Number (Fr_i, left axis). The dashed horizontal line in panel (d) indicates the critical threshold (Fr_i = 1). The vertical dotted line marks the point of maximum constriction at the estuary–shelf interface……..……103

Chapter VI: Spatial variability of turbulent mixing in a highly stratified system

Figure 1: Study area: **(a)** Location of the Patos Lagoon in relation to South America. **(b)** Patos Lagoon and its complex system with the Mirim Lagoon and other rivers and their watersheds. **(c)** Patos Lagoon and the location of the inlet. (d) Position of the three cross-sections and the Rio Grande Pilot Station where wind, current, and tide data were collected. The distance in km shows the spatial variability using T1 as a reference……121

Figure 2: Example output from one station. **(a)** Example profile of ϵ (black line) after bootstrapping the ϵ estimates from the 5 casts from both shear probes (10 profiles total). The dashed lines represent a 95% confidence interval. **(b)** Example wave number spectra with noise removed showing the shear estimates from each probe (thick blue and red lines), the theoretical Naysmyth spectra (black line) the limits of integration in wave number space for each shear probe to estimate ϵ (blue and red triangles), and the vertical temperature gradient (yellow and green lines)……127

Figure 3: Ambient conditions over a one-week interval, with the vertical yellow bar representing the field period. **(a)** Estimated discharge of the main tributaries of Patos Lagoon (blue line representing the total main tributaries discharge and

black dotted line at the bottom of the diagram representing the average estimated discharge for July 2022); **(b)** vector plot of wind, where blue represents northwards winds and red represents southwards winds; **(c)** water level, where the three vertical lines indicate the moments when the cross-sections were conducted; **(d)** Hovmöller diagram of current velocity, where red indicates inflow and blue indicates outflow……131

Figure 4: Cross-sectional distributions of **(a)** salinity, **(b)** temperature, and **(c)** density, looking landward in the cross-sections T1 (left), T2 (center), and T3 (right). The color bar scales are different for each transect to magnify the variability……..……133

Figure 5: (a) Along-channel and **(b)** cross-channel velocities measured by vessel-mounted ADCP at the three cross-sections. Note that transects share the same color scale. In (a), positive values represent inward flow, while negative values indicate outward flow. In (b), positive values correspond to westward flow (left to right), and negative values indicate eastward flow (right to left)……134

Figure 6: Calculated parameters for T1: **(a)** squared vertical shear (S^2); **(b)** buoyancy frequency (N^2); **(c)** gradient Richardson number (R_i), with the solid lines representing the values of R_i=0.25 and the dotted lines representing R_i = 1; **(d)** TKE dissipation (ϵ). The black x's denote the MCTD stations throughout the distance (m); **(e)** vertical eddy viscosity (A_z); and **(f)** buoyancy Reynold number (Re_b), with the solid lines representing the values of Re_b = 200. All subplots show log10 values and the x-axis depicts the distance in meters from the beginning of the transect and the y-axis depicts depth in meters……..……136

Figure 7: Calculated parameters for T2: **(a)** squared vertical shear (S^2); **(b)** buoyancy frequency (N^2); **(c)** gradient Richardson number (R_i), with the solid lines representing the values of R_i=0,25 and the dotted lines representing R_i = 1; **(d)** TKE dissipation (ϵ). The black x's denote the MCTD stations throughout the distance (m); **(e)** vertical eddy viscosity (A_z); and **(f)** buoyancy Reynold number (Re_b), with the solid lines representing the values of Re_b =200. All subplots show

log [10] values and x-axis depicts the distance in meters from the beginning of the transect and the y-axis depicts depth in meters.……138

Figure 8: Calculated parameters for Transect 3: **(a)** squared vertical shear (S^2); **(b)** buoyancy Frequency (N^2); **(c)** gradient Richardson Number (R_i), with the solid lines representing the values of R_i=0.25 and the dotted lines representing R_i = 1; **(d)** TKE dissipation (ϵ). The black x's denote the MCTD stations throughout the distance (m); **(e)** vertical eddy viscosity (A_z); and **(f)** buoyancy Reynold number (Re_b), with the solid lines representing the values of Re_b200 and dotted lines representing values = 15. All subplots show log [10] values and x-axis depict the distance in meters from the beginning of the transect and the y-axis depicts depth in meters……..140

Figure 9: Spectrogram of the sea level and current velocity (sampling interval = 5 minutes) during the entire month of July 2022. The vertical red lines serve as references for various tidal cycles, including QD (quarter-diurnal), SD (semi-diurnal), and D (diurnal), as well as 3-day and 15-day cycles.....142

Figure 10: Comparison between mixing parameters of one vertical profile of cross-section T3. **(a)** Along-channel velocity; **(b)** density; **(c)** solid line representing buoyance frequency (N^2), dotted line representing squared vertical shear (S^2) and dashed line representing vertical eddy viscosity (A_z). The x-axis in subplot (c) show log [10] values of the parameters and the y-axis depicts depth in meters. ……..…….148

Appendix A – Microstructure Data Processing Workflow

Figure 1: Comparison between the default *ql_info* configuration and the customized *ql_info_patos* used in this study. Highlighted parameters indicate the main modifications applied to adapt the processing to the conditions of the Patos Lagoon inlet. In particular, adjustments to *diss_length* and *fft_length* reflect

changes in the temporal resolution of ε estimates, while modifications to *profile_min_P* and *profile_min_duration* allow the inclusion of shorter and shallower valid segments. The selection of *op_area* = *'tidal_ch'* represents the confined and high-shear conditions characteristic of the study area……...192

Figure 2: Pressure record for the entire data file, with the selected profile highlighted in red. ……..…..……196

Figure 3: Kinematic properties of a representative MCTD profile. **(a)** Roll angle (θx) measured by the onboard inclinometer; acceptable values are typically within ±5°, with smaller variations indicating a stable, near-vertical descent. **(b)** Vertical descent velocity expressed as dP/dt; the instrument is expected to accelerate toward its nominal operating speed of approximately 0.8 dbar s^{-1}, with values between ~0.7 and 0.9 dbar s^{-1} considered acceptable. ……198

Figure 4: Vertical profiles obtained from the conductivity–temperature (CT) sensor (JFE Advantech, JAC). **(a)** temperature, **(b)** conductivity, **(c)** salinity, and **(d)** potential density anomaly (σθ), all shown as functions of pressure……...199

Figure 5: **(a)** Wavenumber spectra and **(b)** frequency spectra obtained from MCTD measurements. In panel (a), shear spectra are shown in blue and red, with thick lines indicating signals corrected for coherent noise and thin lines representing uncorrected spectra. Triangular markers denote the upper wavenumber limits used in the integration for ϵ estimation. Black curves represent theoretical Nasmyth spectra for the corresponding dissipation rates. In panel (b), vibration sensor spectra are shown as thick lines, while shear and temperature gradient spectra follow the same color scheme as in panel (a). ……..…201

Figure 6: Vertical profile of the turbulent kinetic energy dissipation rate (ϵ) estimated from shear probe measurements. Independent estimates from the two probes (ϵ_1 and ϵ_2) are shown in blue and red, respectively; close agreement between the two indicates good data quality……..……202

List of Tables

Note: Tables are numbered independently within each chapter. In chapters based on published or submitted articles, they retain their original numbering to preserve consistency with the source material.

Chapter IV: Materials and Methods

Table 1. Summary of instrumentation and sampling specifications……..….46

Chapter V: Turbulence and mixing along a microtidal and stratified estuary-shelf transition

Table 1: Range of hydrodynamic and turbulent parameters observed inside the channel and on the adjacent shelf. Values represent the absolute minimum and maximum recorded during the drift survey.....…..……...……105

Table 2: Global comparison of maximum TKE dissipation rates (ϵ) and tidal regimes across different estuarine systems.....…..……...……..107

Chapter VI: Spatial variability of turbulent mixing in a highly stratified system

Table 1: Order of magnitude comparison between lateral baroclinic pressure gradient, and acceleration due to curvature for the cross-sections…….……150

Table 2: Summary of results of along-channel velocity, velocity shear, eddy viscosity (A_Z), for the cross-sections.……..……..……...152

Appendix A – Microstructure Data Processing Workflow

Table 1: List of main channel ids and their corresponding sensors and signals. Reproduced from Lueck et al. (2020).……..……..……...188

Table 2: List of derived signals and parameters in the mat-files. Reproduced from Lueck et al. (2020)…….……..……..……..189

List of Acronyms, Abbreviations, and Symbols

A

ADCP – Acoustic Doppler Current Profiler

A_z – Vertical eddy viscosity [$m^2\ s^{-1}$]

B

BBL – Bottom Boundary Layer

C

CTD – Conductivity, Temperature, and Depth

F

Fr_i – Internal Froude number [dimensionless]

G

GPS – Global Positioning System

K

k – Wave number [m^{-1}]

L

L_o – Ozmidov length scale [m]

L_k – Kolmogorov length scale [m]

M

MCTD or MicroCTD – Micro-structure profiler

N

N^2 – Buoyancy frequency (or Brunt-Väisälä frequency) [s^{-2}]

NE – Northeast

P

PLE – Patos Lagoon Estuary

R

R – Radius of curvature [m]

Re_b – Buoyancy Reynolds number [dimensionless]

R_f – Richardson flux number [dimensionless]

R_i – Richardson number [dimensionless]

S

S^2 – Squared vertical shear [s^{-2}]

S – South

SSE – South-Southeast

SE – Southeast

SW – Southwest

T

T1 – Transect 1 (Upstream cross-section)

T2 – Transect 2 (Mid-channel cross-section)

T3 – Transect 3 (Downstream cross-section)

TKE – Turbulent Kinetic Energy [$J\ kg^{-1}$]

U

u – Zonal velocity component (East-West) [$m\ s^{-1}$]

V

v – Meridional velocity component (North-South) [$m\ s^{-1}$]

Z

z – Vertical coordinate [m]

GREEK SYMBOLS

ϵ – Dissipation rate of turbulent kinetic energy [$W\ kg^{-1}$]

ν – Kinematic viscosity of seawater [$m^2\ s^{-1}$]

ρ – Density of seawater [$kg\ m^{-3}$]

ρ_0 – Reference density [$kg\ m^{-3}$]

Ψ – Velocity shear spectrum [$m\ s^{-2}$]

Γ_m – Mixing coefficient [dimension less]

Resumo

Esta tese investiga como a morfologia do canal, a estratificação e as forçantes externas controlam a dinâmica do escoamento e os processos de turbulência e mistura na transição estuário-plataforma em um sistema micromareal. Foram realizadas medições in situ de alta resolução com um perfilador de microestrutura (MCTD), permitindo a estimativa direta da taxa de dissipação da energia cinética turbulenta (ϵ) sob diferentes condições hidrodinâmicas, incluindo cenários de alta descarga fluvial e de forte estratificação do tipo cunha salina. Os resultados mostram que, em condições de alta descarga, a morfologia do canal acelera o escoamento, promovendo elevados níveis de dissipação de energia, comparáveis a sistemas meso- e macromareais, favorecendo a mistura ao longo da transição estuário-plataforma. Em contraste, sob forte estratificação, o aumento das velocidades e do cisalhamento não resulta necessariamente em maior mistura, pois a presença da cunha salina suprime a turbulência e limita a troca vertical, mesmo em regiões de alto cisalhamento. Esses resultados demonstram que a relação entre intensidade do escoamento e mistura é fortemente modulada pelo balanço entre produção de turbulência por cisalhamento e supressão por estratificação. Em escalas curtas, o sistema apresenta elevada variabilidade, podendo transitar, em menos de 24 horas, entre regimes parcialmente misturados e altamente estratificados, controlados principalmente por vento e descarga fluvial. Este trabalho apresenta as primeiras medições diretas de mistura turbulenta na Lagoa dos Patos, preenchendo uma lacuna sobre estuários micromareais. Ao explorar um sistema com reduzida influência da maré, esta tese permite isolar os mecanismos fundamentais que controlam a mistura, contribuindo para uma melhor compreensão desses processos, com implicações para outros sistemas estuarinos.

Palavras-chave: hidrodinâmica; mistura turbulenta; estratificação; plumas fluviais; estuário-plataforma; cunha salina; micromaré.

Abstract

This thesis investigates how channel morphology, stratification, and external forcing control flow dynamics, turbulence, and mixing across the estuary–shelf transition in a microtidal system. High-resolution in situ measurements were conducted using a microstructure profiler (MCTD), allowing for the direct estimation of the turbulent kinetic energy dissipation rate (ϵ) under different hydrodynamic conditions, including high river discharge and strongly stratified salt-wedge regimes. Results show that under high-discharge conditions, channel morphology accelerates the flow and generates elevated dissipation rates comparable to those observed in meso- and macrotidal systems, thus promoting mixing along the estuary–shelf transition. In contrast, under strong stratification, increased velocities and shear do not necessarily lead to enhanced mixing, as the presence of a salt wedge suppresses turbulence and limits vertical exchange, even in the regions of highest shear. These findings demonstrate that the relationship between flow intensity and mixing is strongly modulated by the balance between shear production and buoyancy suppression. Furthermore, the system exhibits pronounced short-term variability, transitioning within less than 24 hours between partially mixed and highly stratified regimes, primarily controlled by wind forcing and river discharge. This study provides the first direct in situ measurements of turbulent mixing in the Patos Lagoon, addressing a significant gap in microtidal estuaries. By investigating a system with reduced tidal influence, this work isolates the fundamental processes controlling mixing and contributes to a broader understanding of estuarine dynamics, with implications for other estuarine environments.

Keywords: hydrodynamics; turbulent mixing; stratification; river plumes; estuary-shelf; salt wedge; microtidal.

Chapter I: Introduction

1.1 The Physics of Estuaries and Mixing

In physical terms, estuarine mixing is the process by which different water masses exchange properties. This mechanism is primarily driven by turbulence, which transfers energy from larger to smaller scales, where it is dissipated as heat (Thorpe, 2007). Eddies deform density interfaces and increase the interfacial area available for molecular diffusion, which ultimately governs the redistribution of properties between fresh and salt water. In this context, stratification modulates vertical mixing by suppressing turbulent exchanges (Geyer and MacCready, 2014).

The implications of turbulent mixing extend beyond physical processes, dictating the broader biogeochemical functions of estuaries and coastal environments. Estuarine systems serve as critical filters at the land–ocean interface, where circulation and mixing patterns govern the transport, retention, and export of materials (Burchard et al., 2008). For instance, vertical mixing acts as a primary control on ecosystem productivity by modulating the availability of light and nutrients (Cloern, 2001). Conversely, when stratification suppresses mixing, it can lead to severe environmental consequences, such as the isolation and retention of subpycnocline waters, resulting in oxygen depletion and hypoxic conditions (Rabouille et al., 2008). Ultimately, while residence time is primarily controlled by advective processes and external forcing, mixing plays a key role in modulating water mass retention and flushing by redistributing properties both laterally and vertically, with important implications for water quality and biophysical modeling (MacCready and Geyer, 2010).

In addition to the physical and ecological controls described above, mixing in estuaries and their associated plumes plays a central role in coastal carbon cycling. These plumes are defined as buoyant coastal outflows where estuarine waters spread onto the inner shelf (Horner-Devine et al., 2015). As dynamic interfaces, these systems modulate air–sea CO_2 exchange through terrestrial inputs of nutrients and organic matter that stimulate intense biological activity (Cai et al., 2013; Lohrenz et al., 2013). Enhanced primary production and subsequent respiration within the estuary–plume continuum can shift these systems

between CO_2 source and sink regimes, depending on the balance between biological processes and physical mixing (Wu et al., 2023). Recent evidence suggests that while biological activity dominates the variability of CO_2 concentrations, physical processes such as vertical mixing exert a significant influence by regulating the ventilation of subsurface waters, with lateral mixing redistributing dissolved gases across the coastal zone (Sims et al., 2022). In this context, turbulent mixing is a fundamental regulator linking hydrodynamics, carbon cycling, and oxygen dynamics in estuarine and plume systems.

1.2 Turbulence: Mechanisms and Theoretical Challenges

Turbulence, first characterized by Osborne Reynolds in the late 19th century, remains one of the most complex phenomena in fluid mechanics, given its chaotic nature and the semi-empirical basis of its governing theory (Simpson and Sharples, 2012). In estuaries, the hydrodynamic functioning is governed by the along-channel momentum balance, where forcing mechanisms such as pressure gradients and advection are primarily opposed by vertical turbulent stress. According to the classical formulation by Geyer and MacCready (2014), this balance can be expressed as:

$$\frac{\partial u}{\partial t} + u \,.\, \nabla u \; - fv = -g\frac{\partial \eta}{\partial x} \; - \frac{g}{\rho_0} \int_z^{\eta} \frac{\partial \rho}{\partial x} d\hat{z} + \; \frac{\partial}{\partial z} \left(A_z \frac{\partial u}{\partial z}\right), \qquad (1)$$

where *u* and *v* are the along-channel and cross-channel velocity components, *f* is the Coriolis parameter, ρ is the water density, *g* is gravitational acceleration, ρ_0 is a reference density, and A_z is the vertical eddy viscosity, commonly used as a proxy for mixing.

In the equations of motion, turbulence emerges through fluctuations, the Reynolds stresses ($\tau = -\rho\overline{u'w'}$), representing the vertical transport of momentum. In practice, these unresolved turbulent motions are parameterized using the vertical eddy viscosity (A_z), which represents the efficiency of vertical transport in structuring the overall circulation (Monismith, 2010) and links these fluctuations to the large-scale flow structure.

While these fluctuations are challenging to resolve directly, the intensity of turbulence can be fundamentally characterized by the turbulent kinetic energy (TKE) dissipation rate (ϵ). This parameter quantifies the rate at which energy is extracted from the mean flow and converted into heat at the smallest scales (Thorpe, 2007), serving as a key measure of turbulent activity in stratified flows. Theoretically, the relationship between energy loss (ϵ) and the efficiency of momentum transport (A_z) is established through the vertical shear ($S = \partial u/\partial z$) and the mixing efficiency (Γ_m), following the approach used by Ross et al. (2019a) and Huguenard et al. (2015):

$$A_z = \Gamma_m \frac{\epsilon}{S^2} \quad (2)$$

Although ϵ and A_z represent different aspects of the turbulent process, the former focusing on energy loss and the latter on momentum transport, both are essential for describing how stratified environments dissipate energy and drive vertical transport (Collignon and Stacey, 2013).

Nevertheless, the application of these concepts in estuarine systems is challenged by the complex spatial and temporal variability of turbulence. As demonstrated by Ross et al. (2021), the relative importance of these momentum terms can shift along the estuary, as variations in geometry and bathymetry modulate the balance between friction and advection. The actual distribution of ϵ remains poorly understood, as it is strongly influenced by the interaction between topography, stratification, and shear. In general, estuarine mixing is driven by three primary mechanisms: (a) shear at the bed, (b) interfacial shear and instabilities, and (c) wind stress at the surface (Monismith, 2010). In the bottom boundary layer (BBL), vertical shear is typically strongest due to bottom friction. Close to the bed, a well-mixed region can develop in which shear-driven turbulence production is not significantly influenced by stratification (Stacey et al., 1999; Ross et al., 2019a).

Furthermore, mixing is not solely a bottom-up process, as it can also be generated by shear instabilities directly at the pycnocline, occurring

independently of bed-generated turbulence (Peters, 1997; Huguenard et al., 2015). However, the presence of an overlying pycnocline can limit the vertical transfer of turbulent kinetic energy (TKE) to the rest of the water column if the stratification is sufficiently strong to overcome the homogenizing power of shear production (e.g., Turner, 1973; Ivey et al., 2008).

Historically, turbulent kinetic energy dissipation rates (ϵ) have often been estimated through indirect methods, such as the covariance of velocity fluctuations or the beam variance method using Acoustic Doppler Current Profilers (ADCP) (Trowbridge et al., 1999; Stacey et al., 1999). These approaches rely on velocity measurements and assume flow homogeneity across the sampling volume. While these acoustic techniques revolutionized field oceanography by providing continuous time series of turbulence, they often suffer from limitations in highly stratified or high-energy environments, where acoustic noise and departures from this assumption can introduce significant uncertainties in the TKE estimates.

1.3 Methodological Evolution of Quantifying Turbulence

Historically, turbulent kinetic energy dissipation rates (ϵ) have often been estimated through indirect methods, such as the covariance of velocity fluctuations or the beam variance method using Acoustic Doppler Current Profilers (ADCP) (Trowbridge et al., 1999; Stacey et al., 1999). These approaches rely on velocity measurements and assume flow homogeneity across the sampling volume. While these acoustic techniques revolutionized field oceanography by providing continuous time series of turbulence, they often suffer from limitations in highly stratified or high-energy environments, where acoustic noise and departures from this assumption can introduce significant uncertainties in the TKE estimates.

Complementary indirect estimates of TKE can also be derived via the inertial dissipation method, based on spectral fitting within the inertial subrange, or through the calculation of Thorpe scales from density overturns (Thorpe, 2007). In the latter case, ϵ is inferred from density structure rather than velocity, assuming that observed overturns result from turbulent mixing and can be related to dissipation through empirical relationships. Nevertheless, these approaches, whether based on velocity fluctuations or density structure, are often limited in their ability to resolve the non-stationary nature of estuarine turbulence.

To overcome these methodological limitations, the use of microstructure shear profilers, such as the MicroCTD (MCTD), have become the primary approach for quantifying mixing. Unlike acoustic methods that estimate turbulence from larger-scale velocity fluctuations, microstructure profilers allow for the direct quantification of the TKE dissipation rate (ϵ) by resolving the vertical shear of velocity at scales approaching the Kolmogorov microscale (millimeter to centimeter range) (Collignon and Stacey, 2013). This high-resolution view is essential for capturing the rapid decay of turbulence in transient features like fronts and plumes, where energy is lost to viscous scales at rates that indirect methods often fail to capture (Spicer, 2022).

The adoption of microstructure technology has significantly advanced estuarine research. For instance, Huguenard et al. (2015) and Ross et al. (2019a) utilized direct dissipation measurements to investigate the complex interaction between tidal straining and interfacial mixing, respectively. Furthermore, in fjord-like and highly stratified systems, Pérez-Santos et al. (2018) demonstrated that high-resolution MCTD observations are vital for linking physical turbulence to biological processes, showing how localized mixing events contribute to the oxygenation of hypoxic layers. In the context of river plumes, where mixing occurs in thin, sheared layers, Spicer (2022) emphasized that direct measurements are crucial for validating the mixing efficiency in numerical models, which often overestimate these processes in the absence of high-resolution observational constraints. Therefore, the implementation of MCTD profiling in the Patos Lagoon

Estuary represents a critical step in surpassing the observational limitations of the past, providing the first direct evidence of how energy is dissipated in this unique microtidal environment.

1.4 The Knowledge Gap: Microtidal Systems and the Spatial Evolution of Turbulence

To date, the majority of research on estuarine mixing has focused on partially mixed meso-tidal or macrotidal environments, where tidal straining and bed shear are the primary drivers of turbulence (Peters, 1999; Ross et al., 2019a, Stacey et al., 1999; Trowbridge et al., 1999; Giddings et al., 2011). Consequently, microtidal systems remain comparatively understudied, leaving a significant gap in our understanding of how wind and river discharge, rather than tides, regulate the dissipation of TKE (Fig.1).

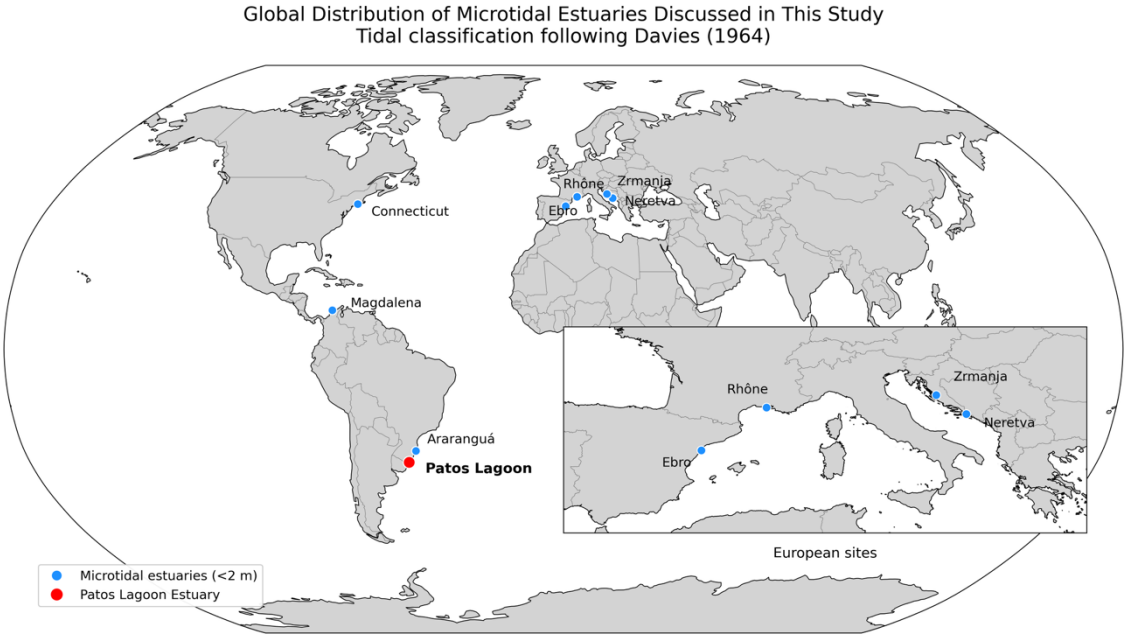


Figure 1. Global distribution of microtidal estuaries (<2 m tidal range) discussed in this study. The Patos Lagoon Estuary (Brazil), highlighted in red, is presented as the primary study site. Additional microtidal systems from different regions (e.g., North America, South America, and Europe) are shown in blue to provide a comparative geographical context. The inset highlights European sites for clarity. Tidal classification follows Davies (1964).

Although the dynamics and structure of river plumes have been widely investigated (e.g., O'Donnell et al., 2008; Hetland, 2005; Horner-Devine et al., 2015), and some studies have incorporated direct turbulence measurements (e.g., MacDonald and Geyer, 2004; MacDonald et al., 2007; Stacey et al., 2012; Spicer et al., 2022), these investigations are typically limited to specific regions or process-oriented analyses. As a result, there remains limited observational

evidence resolving the continuous longitudinal evolution of turbulence from the estuarine inlet into the near-field plume as a connected system, particularly across the transition from source-dominated to buoyancy-influenced flow regimes.

This thesis addresses these gaps by using the Patos Lagoon Estuary (PLE) as a strategic natural laboratory (Fig. 1 and 2). Unlike typical estuaries where intense tidal cycles often mask secondary forcing, the microtidal nature of the PLE, where circulation is dominated by meteorological forcing rather than astronomical tides, provides an ideal setting to isolate the mechanisms governing turbulence. By minimizing tidal complexity, this system allows for a process-based investigation into how river discharge, wind forcing, and geomorphological constraints modulate the spatial evolution of turbulent kinetic energy dissipation (ϵ). In particular, this approach enables the investigation of (i) the evolution of turbulence across the estuary–plume transition; (ii) the influence of geomorphology on the spatial distribution of turbulence; and (iii) the longitudinal spatial variability of turbulence in a salt-wedge estuary. These characteristics, which will be detailed in the following chapter, provide new insights into mixing processes in stratified, high-energy microtidal systems.

1.5 Study Area: The Patos Lagoon Estuary (PLE)

The Patos Lagoon Estuary (PLE) in southern Brazil is a prime example of a microtidal environment (Fig. 1). It features a micro-tidal range of approximately 0.4 m, where astronomical signals are easily overridden by meteorological forcing (Möller et al., 2007; Santa-Rosa and Schettini, 2024). Spectral analyses have confirmed that both water level variability and circulation in this region are dominated by meteorological components associated with synoptic-scale processes (Barros et al., 2025). In particular, the passage of extratropical cyclones and their associated atmospheric fronts modulate the regional wind field and sea-level pressure, establishing the primary forcing for the Patos Lagoon at subtidal scales (Miranda et al., 2026).

Under this meteorologically-driven regime, predominant northeasterly winds favor freshwater outflow and plume expansion, whereas southwesterly winds, typically associated with the passage of cold fronts (Machado and Calliari, 2016), promote coastal sea-level rise and landward flow (Möller et al., 2001; Miranda et al., 2026). However, this wind-driven modulation is strongly dependent on the hydrological state, with mean river discharge of approximately 2,400 $m^3\ s^{-1}$, frequently increasing to 12,000 $m^3\ s^{-1}$ during seasonal flood episodes (Vaz et al., 2011; Marques et al., 2014), while recent extreme events have exceeded these historical peaks (Simão et al., 2026). During high river discharge periods, the fluvial forcing can overcome the effect of southwesterly winds, maintaining a persistent ebb regime (Möller et al., 2001; Monteiro et al.,

2011). Depending on the balance between river discharge and wind-driven pressure gradients, the Rio Grande Channel can transition rapidly between well-mixed conditions and highly stratified salt-wedge patterns (Hartman and Schettini, 1991; Möller & Castaing, 1999).

The circulation is further modulated by the geomorphology of the lower estuary. The PLE presents an inverted morphology compared to traditional drowned valley estuaries, with a funnel shape that tapers towards the lagoon mouth (Fig.2). This geometric configuration induces a "nozzle effect" that intensifies current velocities at the terminal constriction (Armi and Farmer, 1986). Furthermore, the presence of long jetties profoundly alters the local hydrodynamics, extending the influence of the estuarine jet onto the shelf and acting as a physical constraint that can either weaken stratification through increased shear or promote hydraulic control (Franzen et al., 2023).

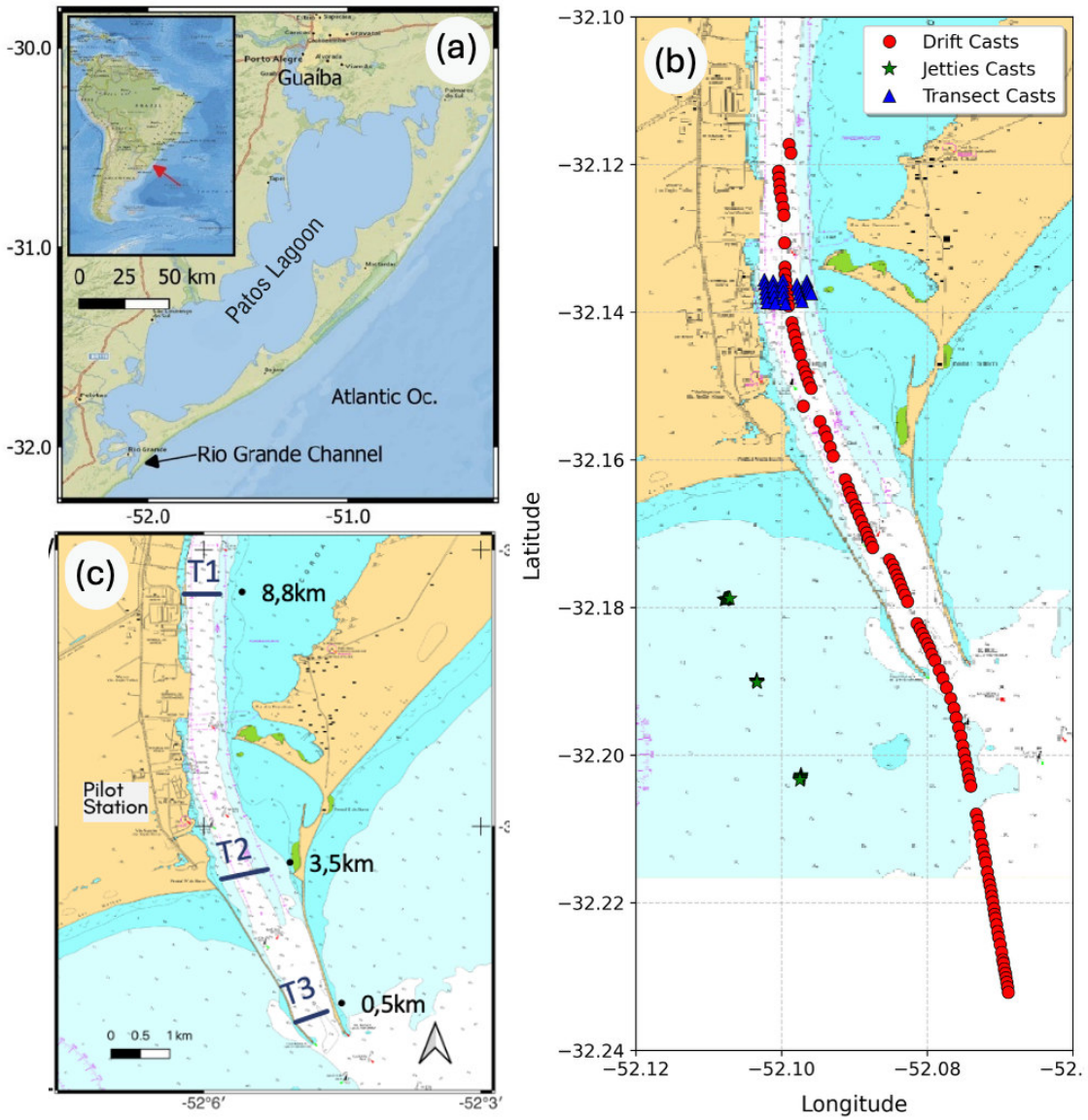


Figure 2. Study area and sampling design integration. **(a)** Regional setting showing the Patos Lagoon choked system and its connection to the South Atlantic Ocean via the Rio Grande Channel; adapted from Barros et al. (2026). **(b)** Detailed view of sampling stations for Chapter V, including the longitudinal track (Drift), baseline stations near the breakwaters (Jetties), and the cross-channel section (Transect). **(c)** Cross-section positions (T1, T2, and T3) for

Chapter VI, including the Rio Grande Pilot Station (source for meteorological and water level data) and distances from the estuary mouth; adapted from Barros et al. (2025). Panel (a) is based on XYZ tiles from Esri National Geographic. Panels (b) and (c) are based on the Brazilian Navy nautical chart No. 2110, available as a GeoTIFF at: https://www.marinha.mil.br/chm/dados-do-segnav/cartas-raster.

Despite the PLE's regional importance as a major conduit for freshwater, sediments, and biogeochemical fluxes to the adjacent shelf, including the export of exceptionally large suspended loads during extreme discharge events (Simão et al., 2026), the impacts of these hydrodynamic conditions on turbulence and energy dissipation scales (ϵ) have never been quantified through direct observations. Research has been predominantly based on remote sensing and numerical modeling of coastal transport and surface circulation (Piola et al., 2005; Marques et al., 2010; Kirinus et al., 2012; Zavialov et al., 2018). While these studies have advanced the understanding of surface plume dynamics and seasonal variability, there remains a lack of direct field-based observations to quantify the subsurface mixing rates and associated turbulence structure.

Chapter II: Hypothesis

Considering that turbulence in estuarine flows is primarily generated by velocity shear and modulated by stratification, and given the microtidal nature of the Patos Lagoon Estuary, which allows the influence of geomorphological constraints on flow dynamics to be more clearly isolated, the hypothesis of this study is:

"The convergent morphology at the mouth of the Patos Lagoon enhances seaward flow velocities, thereby intensifying turbulence and consequently increasing vertical mixing."

Chapter III: Objectives

3.1 General Objective

Investigate how convergent channel morphology controls flow dynamics, turbulence, and mixing across the estuary–shelf transition in a stratified microtidal system.

3.2 Specific Objectives

- Quantify the influence of channel morphology on circulation and on the along-channel structure of velocity and density fields from the estuary to the buoyant plume.
- Evaluate how the interplay between shear production and buoyancy suppression controls the generation and vertical distribution of turbulence and mixing along the inlet and plume.
- Compare the hydrodynamic and mixing behavior of the Patos Lagoon inlet with other estuarine systems, including microtidal, mesotidal, and macrotidal environments, in order to place the observed processes within a broader physical context.

Chapter IV: Materials and Methods

4.1 Observational Strategy

Measuring turbulence in estuarine environments is inherently challenging due to its intermittency, strong vertical gradients, and the need for high-resolution observations capable of resolving small-scale processes (Thorpe, 2007; Geyer and MacCready, 2014). Several approaches are available to estimate turbulence, including indirect methods based on velocity structure or stratification, as well as direct measurements using microstructure sensors (Simpson and Sharples, 2012; Lueck et al., 2013).

In this study, a direct microstructure-based approach was adopted to obtain reliable estimates of turbulent kinetic energy dissipation (ϵ), particularly under strongly stratified and energetic regimes. Field measurements were

designed to resolve the spatial variability of hydrodynamics, stratification, and turbulence across the estuary–shelf transition of the Patos Lagoon Estuary (PLE). Given the microtidal nature of the system, where circulation is primarily controlled by wind forcing and river discharge, the sampling strategy prioritized spatial coverage over tidal phase. This approach allows datasets to be interpreted as quasi-synoptic representations of the flow conditions.

Two field campaigns were analyzed in this thesis. Chapter 5 (Barros et al., 2026) focuses on the estuary–shelf transition under high-discharge conditions, while Chapter 6 (Barros et al., 2025) examines internal estuarine dynamics under stratified (salt-wedge) conditions. Together, these datasets provide complementary observations of turbulence and mixing under contrasting hydrodynamic regimes.

This chapter provides an overview of the methodological approach adopted in this thesis, while detailed, study-specific procedures are presented in the subsequent chapters and further described in Appendix A.

4.2 Instrumentation and Data Acquisition

The observational dataset combines high-resolution measurements of velocity, water properties, and turbulence, complemented by environmental forcing data. A summary of the instrumentation and sampling characteristics used across both field campaigns is provided in Table 1.

4.2.1 Hydrodynamics and water properties

Current velocities were measured using vessel-mounted Teledyne RDI Workhorse 1200 kHz Acoustic Doppler Current Profiler (ADCP) operating in bottom-tracking mode. The instrument was configured with a ping interval of 0.5 s and a vertical bin size of 0.25 m, with the first measurement bin located approximately 1.5 m below the surface. Horizontal positioning was determined via a GPS unit directly connected to the ADCP system, with an estimated positional uncertainty of ~5 m.

Water properties, including salinity and temperature, were recorded using a Conductivity-Temperature Combo Sensor (JAC CT) integrated into the microstructure profiler. Additionally, a Rinko Profiler CTD (JFE Advantech LTD) was used during the campaigns to provide complimentary vertical profiles and ensure data redundancy. These instruments allowed for the characterization of

water mass structure and density stratification across the different sampling segments.

4.2.2 Microstructure and Turbulence

Turbulence measurements were acquired using a Rockland Scientific Micro-CTD (MCTD), a free-falling microstructure profiler. The MCTD was equipped with two orthogonally mounted high-frequency shear probes sampling at 512 Hz, enabling the direct estimation of the turbulent kinetic energy (TKE) dissipation rate (ϵ). During both campaigns, the MCTD was deployed in downward profiling mode using a weighted collar to ensure a controlled descent speed of approximately 0.8 m s^{-1} and an angle of attack below 5°, ensuring high-quality shear measurements (Lueck et al., 2013).

4.2.3 Environmental Forcing

Additional environmental data were obtained to provide the synoptic context for the surveys:

- *Meteorological and Eulerian Data:* Wind speed and direction (Davis Vantage Pro 2), water level, and currents (moored Sontek Argonaut-XR 1.5 MHz ADCP) were obtained from the Rio Grande Pilot Station.

- *River Discharge*: Estimates of freshwater discharge were based on daily records from the primary tributaries (Jacuí, Taquari, Caí, Sinos, and Camaquã rivers) retrieved from the ANA Hidroweb database, following the aggregation methodology of Santa-Rosa and Schettini (2024). Discharge from the São Gonçalo Channel was provided by the Mirim Lagoon Agency (ALM/UFPel).

Table 1. Summary of instrumentation and sampling specifications

Parameter	Instrument	Sampling Mode	Resolution/Frequency
Current Velocity	ADCP (Teledyne RDI 1200 kHz)	Vessel-mounted (Bottom-track)	0.25 m bins / 2 Hz (0.5 s)
Water properties	CTD (Rinko Profiler / JAC CT)	Profiling /Yo-Yo	24 Hz
TKE dissipation	MCTD (Rockland Scientific)	Profiling / Free-fall	512 Hz
Moored Currents	ADCP (Sontek Argonaut-XR)	Fixed (17 m depth)	1.5 m bins / 5 min avg
Wind Velocity	Davis Vantage Pro 2	Fixed Station	5 min (hourly avg)
River Discharge	Jacuí, Taquari, Caí, Sinos, and Camaquã rivers	Daily Records	National Database (ANA)

Detailed descriptions of the sampling configuration, deployment procedures, and data acquisition for each field campaign are provided in Sections 5.3.1 and 6.3.1.

4.3 Data Processing and Analysis

4.3.1 ADCP Processing

Velocity data from the vessel-mounted ADCP were inspected and exported using WinRiver II software. Following the field campaigns, the raw data were exported as ASCII files according to the standardized protocols described by Schettini (2021). Subsequent pre-processing and analysis were implemented using custom Python routines (Barros et al., 2026) and is described in detail in Appendix A.5.1.

Data quality control involved trimming the bottom 10% of the profiles to mitigate side-lobe interference and excluding velocities exceeding 5% of the maximum flow. Furthermore, ensembles with a signal return (correlation) lower than 85% were removed (Ross et al., 2019a). To ensure directional accuracy, a compass calibration was performed by comparing instrument bottom-track velocities with GPS data (Joyce, 1989; Valle-Levinson et al., 2015).

The resulting East-West (u) and North-South (v) velocity components were rotated using Principal Component Analysis (PCA) (Thomson and Emery, 2014) to align with the primary direction of the flow. While the PCA ensures the longitudinal component represents the main flow axis in both studies, the specific

spatial references used for coordinate alignment (e.g., channel sectors or coastline orientation) are detailed in Sections 5.3.2 and 6.3.2.

4.3.2 MCTD Processing

The microstructure data were pre-processed in Matlab following the protocols described by Schettini (2021) (further detailed in Appendix A.4), and a preliminary visual inspection of data quality (Appendix A.3). Subsequently, TKE dissipation rates (ϵ) were derived from measurements of velocity shear assuming locally isotropic turbulence, following the spectral integration method and Equation 1 presented in Sections 5.3.2.2 and 6.3.2.2.

The processing routines included automated filters for profiler vibration (Goodman et al., 2006) and the enforcement of operational thresholds, such as an angle of attack limited to 5^{o} and a descent speed of approximately 0.8 m s^{-1}. Profiles failing these criteria were excluded to ensure the reliability of the turbulence estimates.

4.4 Dataset Integration and Derived Parameters

Following the initial extraction of raw MCTD data in Matlab (Appendix A.4) and the pre-processing of both ADCP and MCTD data in Python (Appendix A.5),

the datasets were synchronized in time and space into a single integrated dataset. This consolidated data structure was used to calculate a set of derived parameters to characterize the interaction between shear, stratification, and turbulence.

The core physical parameters, including their mathematical formulations and conceptual definitions, are presented in detail in Sections 5.3.2.3 and 6.3.2.3. These include:

- *Squared vertical shear* (S^2, Eq. 2);
- *Buoyancy frequency* (N^2, Eq. 3);
- *Mixing efficiency and coefficients* (R_f and Γ_m, Eqs. 4–5);
- *Vertical eddy viscosity* (A_z, Eq. 6);
- *Buoyancy Reynolds number* (Re_b, Eq. 7).

Additional calculations specific to the analyses in Chapter 5 (Barros et al., 2026), such as the internal Froude number (Fr_i, Eq. 8) are further described and defined in Sections 5.3.2.4. Together, these parameters quantify flow stability, turbulence intensity, and mixing efficiency, providing the basis for the analyses presented in the following chapters and enabling the identification of different dynamical regimes across the estuarine system.

4.5 Channel Morphology

To assess the influence of channel geometry on the flow structure, cross-sectional areas were calculated at multiple locations along the lower estuary. This analysis is based on a high-resolution bathymetric survey conducted in 2024 using a single-beam echosounder and DGPS positioning, ensuring an updated representation of the bed morphology.

The inner channel was discretized into 57 cross-sections. For each section, a reference line was defined, and bathymetric data within a ±50 m buffer were projected onto a local coordinate system to reconstruct the channel profile (Fig. 1). The wetted area was then estimated by constructing a closed polygon bounded by the bathymetric profile and a locally horizontal free surface.

The spatial variability of these cross-sectional areas allows for the evaluation of the relationship between channel constriction, flow acceleration, and associated variations in turbulence and energy dissipation (ϵ). This quantification is essential because surface-level convergence (i.e., width reduction) may not necessarily result in a reduction of the total cross-sectional area if accompanied by significant changes in channel depth. Thus, the 3D geometry, combining bathymetric deepening and lateral narrowing, must be resolved to confirm whether physical constriction and subsequent flow acceleration actually occur as the flow approaches the inlet. The mathematical procedures for these projections and the integration method used for area

calculations are defined by Equations 9 and 10, with further methodological details provided in Section 5.3.2.5.

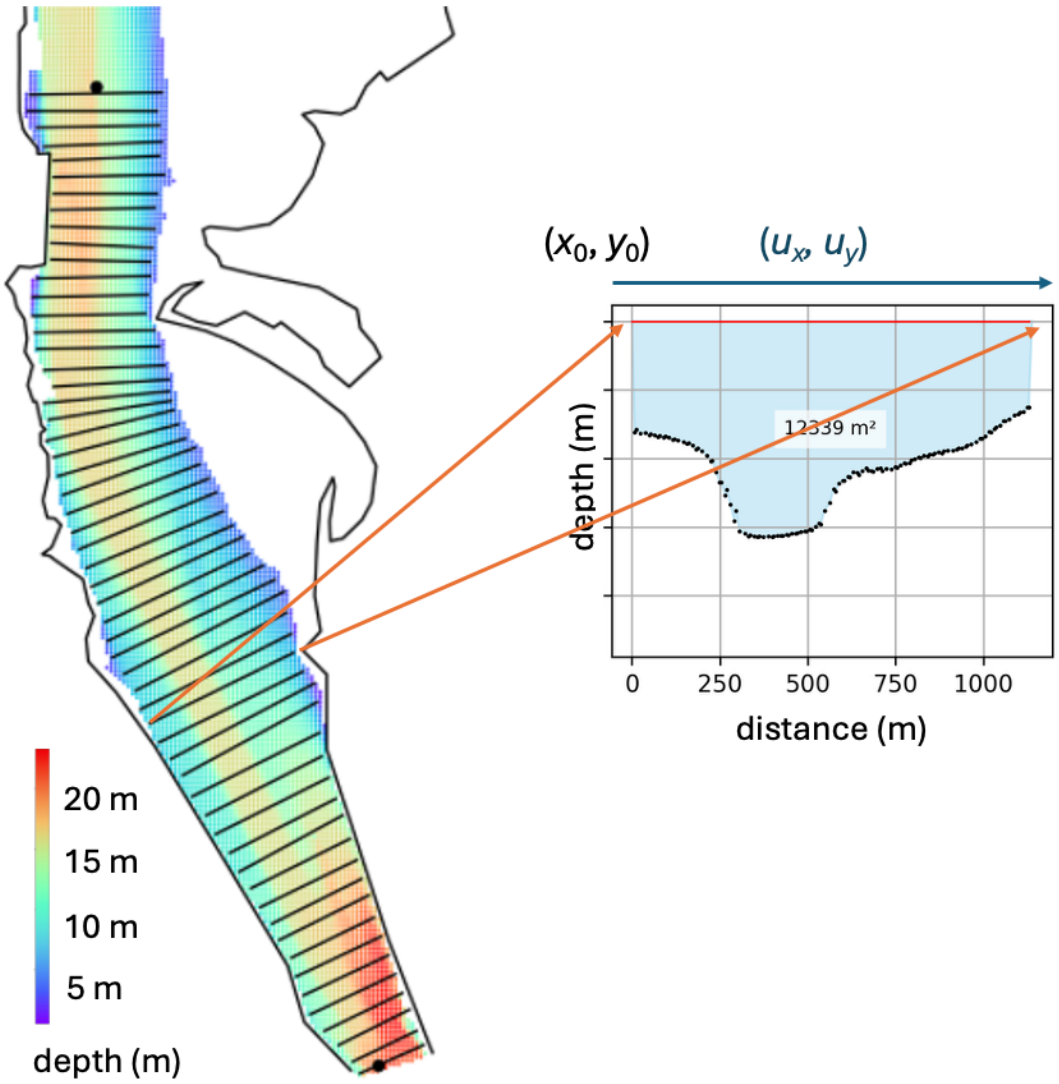


Figure 1. Methodological scheme for channel morphology analysis. (Left) Spatial distribution of the 57 cross-sections along the main channel. (Right) Example of a reconstructed bathymetric profile used for the wetted area calculation, showing the polygon integration between the bed and the free surface. Bathymetric data were collected in 2024 using a single-beam echosounder and DGPS positioning.

4.6 Scope and Limitations

The methodological approach adopted here emphasizes high spatial resolution observations across the estuary–shelf transition under quasi-stationary conditions. While this strategy does not resolve the full temporal variability of the system, the microtidal characteristics of the Patos Lagoon Estuary minimize the influence of tidal variability during surveys. This environment allows for the relative isolation of river discharge and wind effects, providing a clearer assessment of how channel morphology modulates turbulence.

Furthermore, intrinsic limitations of microstructure profiling must be considered. Due to the profiler's need to reach a stable descent rate and vertical orientation, the uppermost layers of the water column (typically the first 1.5 to 2.0 meters) are excluded from the analysis. Similarly, measurements near the seabed are limited to ensure instrument safety; the profiler is prevented from impacting the bed to preserve the integrity of the shear probes and avoid spurious data.

Despite these near-boundary limitations, free-falling microstructure profiling remains the standard approach for direct estimation of the turbulent kinetic energy dissipation rate (ϵ), providing high-resolution measurements that cannot be achieved through indirect methods.

Chapter V: Turbulence and mixing along a microtidal and stratified estuary-shelf transition

The research presented in this chapter characterizes the estuary-shelf transition during intense ebb discharge, revealing how inlet morphology and inertial dominance redefine mixing. Using high-resolution Lagrangian observations, the study identifies the Patos Lagoon inlet as a morphological 'nozzle' that forces the flow into an extremely energetic state, with dissipation levels (10^{-3} W/kg) comparable to macrotidal systems. A central finding of this work is the persistently supercritical flow ($Fr_i > 1$) throughout the sampled area, which blocks internal disturbances. Trends in Fr_i and pycnocline depth suggest that the hydraulic adjustment to a subcritical regime occurs beyond the surveyed

zone. Furthermore, the study demonstrates that the buoyancy Reynolds number (Re_b) is a more robust indicator of the mixing state, accurately identifying turbulence suppression and revealing areas of vigorous, fully developed turbulence at the plume's frontal interface. By deconstructing these mechanisms, this work advances the understanding of how morphology modulates the hydrodynamic regimes of river plumes in high-discharge, microtidal settings worldwide.

This manuscript is authored by Débora Barros, Lauren Ross, and Carlos A.F. Schettini, and is titled ***'Turbulence and mixing along a microtidal and stratified estuary-shelf transition'***. The manuscript is currently under review for publication in ***Ocean Science*** and is available as a preprint at https://doi.org/10.5194/egusphere-2026-1840.

Abstract. This study investigates the hydrodynamic and mixing processes at the estuary–shelf transition of a microtidal system, and the buoyant plume generated at the Patos Lagoon mouth (Brazil). Using measurements of turbulent kinetic energy (TKE) dissipation (ϵ), current velocities, salinity, and temperature collected during a high-discharge period (~9,400 $m^3\ s^{-1}$), we characterize the spatial evolution of turbulence and mixing along the channel, from the source to the buoyancy-driven plume region. Observations show that the jetty-constrained inlet acts as a morphological nozzle, forcing the flow to remain supercritical (*Fri* > 1) for several kilometres onto the inner shelf. Despite strong stratification, intense shear-driven turbulence was observed, with TKE dissipation rates (ϵ) reaching 10^{-3} W kg^{-1} near the mouth, comparable to values reported in high-energy mesotidal and macrotidal systems. Analysis of the buoyancy Reynolds number (Re_b) and the gradient Richardson number (R_i) indicates that inertial forcing overcomes buoyancy suppression, maintaining a predominantly turbulent regime (Re_b > 200) at the plume front. These results demonstrate that, in narrow, high-discharge estuarine outlets, morphological confinement and sustained supercritical flow govern the near-field evolution of buoyant plumes, maintaining vigorous mixing even under pronounced density stratification.

5.1. Introduction

Buoyant plumes are critical hydrodynamic structures in coastal environments, as they represent the primary interaction in the flow transition between laterally constrained estuaries and the adjacent shelf (Fennel and Mutzke, 1997). Plumes are responsible for the injection of freshwater and momentum into the inner shelf, transporting suspended sediments, organic matter, nutrients, and pollutants (Horner-Devine et al., 2015). These inputs play a key role in regulating the coastal carbon budget by stimulating biological production and respiration on the inner shelf (Schettini et al., 1998; Cai et al., 2013; Lohrenz et al., 2013), thereby highlighting the importance of physical mixing in modulating these processes (Sims et al., 2022; Wu et al., 2023).

The dynamics of plumes are driven primarily by the density gradient between the low-salinity freshwater discharge and the denser coastal waters, as well as the momentum associated with the estuarine outflow (Horner-Devine et al., 2015; McPherson et al., 2019). These mechanisms control the plume's basic structure, including its lateral spreading, vertical layering, and the efficiency of mixing with the surrounding ocean.

From a structural perspective, plume dynamics have classically been described in terms of two regions: the near-field (or inner-field) and the far-field (or outer-field) (Jirka et al., 1981). Within the near-field, the low-density discharge

maintains high velocities and is heavily influenced by momentum, characterizing it as a buoyant jet. In this region, momentum dominates over buoyancy, driving high levels of turbulence and intense mixing with the adjacent coastal waters. During the initial stage of plume evolution, the vertical structure is highly stratified, featuring a relatively thin, low-density surface layer flowing energetically over a higher-density ambient water mass.

As the plume moves away from the near-field region, a regime shift occurs in which the initial jet momentum is progressively dissipated, allowing buoyancy to exert greater control over the flow. According to Hetland (2005), this transition between the near-field and the far-field happens when inertial forces cease to dominate the system in favour of gravitational forces. This point is defined by the Froude number decreasing below unity, marking the shift from a supercritical to a subcritical regime and representing a structural change in the balance of forces governing the plume.

The regime transition zone is particularly relevant regarding mixing processes, as it may be linked to the occurrence of internal hydraulic jumps. These features represent areas of intense energy dissipation, playing a crucial role in momentum redistribution and driving vertical mixing between layers. Internal hydraulic jumps can account for up to one-third of the total momentum dissipation in the interfacial layer of stratified estuarine systems (McPherson et al., 2020). Despite their importance, the morphology, structure, and spatial

variability of these mechanisms remain poorly understood in complex natural environments (Thorpe et al., 2017).

Horner-Devine et al. (2015) propose a more detailed approach to the evolution of buoyant plumes, expanding the classical two-region regime of Jirka et al. (1981). This classification defines four distinct regions: (i) the source region, strongly controlled by the mouth geometry and estuarine conditions; (ii) the buoyancy-forced plume region, where barotropic and baroclinic pressure gradients, along with turbulence and mixing, govern the flow; (iii) the mid-field region, characterized by a diminishing influence of initial momentum and the increasing importance of Earth's rotation, friction, wind, and bathymetric interaction; and (iv) the far-field, associated with larger spatial scales, quasi-geostrophic dynamics, and alongshore transport.

Mixing plays a central role in the plume's spatial and temporal evolution, eroding vertical gradients and dissipating kinetic energy. This mixing occurs primarily through instabilities at the fluid interface, as well as through frontal processes and wind forcing (Ivey et al., 2008; Stacey et al., 2012; Spicer et al., 2022). However, direct turbulence measurements within the plume itself are notoriously difficult to perform, despite being fundamental for identifying and understanding the physical mechanisms responsible for mixing (Geyer et al., 2010). Observational studies of buoyant plumes remain scarce at both temporal and spatial scales, limiting a detailed description of plume water transport and

mixing processes, especially in the frontal region (Cole et al., 2020; Delatolas et al., 2023). In addition, most existing studies of plume dynamics and turbulence are concentrated in mesotidal and macrotidal estuaries (MacDonald and Geyer, 2004; MacDonald et al., 2007; Wang et al., 2020; Spicer et al., 2022), whereas comparatively few have focused on microtidal systems (Alvarez-Silva et al., 2026). This highlights an important gap, as microtidal environments provide a valuable framework to isolate and investigate non-tidal forcings and their role in controlling plume structure and mixing dynamics. Furthermore, there is a lack of comparative studies integrating turbulence measurements across different estuarine systems, which could reveal fundamental relationships between plume parameters and the transverse distribution and magnitude of TKE dissipation (ϵ) (Delatolas et al., 2023).

Given the aforementioned gaps, this study aims to investigate the source and buoyancy-forced plume regions through in-situ observations, assessing how mouth morphology modulates the hydrodynamic regime, turbulence, and mixing at the estuary-shelf transition zone. To this end, the following research questions are addressed: (1) How does channel morphology affect the along-channel density and velocity fields of a buoyant river plume from a microtidal estuarine system? (2) How does the interplay between buoyancy suppression and shear production vary along the plume? (3) How does this balance influence the spatial evolution of turbulent kinetic energy dissipation (ϵ) across the transition from the estuarine channel into the plume?

This paper is organized as follows: Section 5.2 describes the study area and its primary characteristics; Section 5.3 outlines the methods; Sections 5.4 and 5.5 discuss the results and their physical implications; and finally, Section 5.6 concludes the study by proposing a conceptual interpretation of the plume's energetic state and the morphological controls governing the estuary-shelf transition.

5.2. Study Area

The study area comprises the Rio Grande Channel, at the mouth of the Patos Lagoon, and the adjacent coastal region in Southern Brazil (32° S / 52° W; Fig. 1). The Patos Lagoon is the world's largest choked coastal lagoon, with an area of approximately 10,000 km², roughly 250 km in length, up to 40 km in width, and an average depth of 5 m (Kjerfve & Magill, 1989; Miranda et al., 2002). At its southern end, the system discharges into the South Atlantic Ocean through the Rio Grande Channel. This region constitutes a critical estuarine-to-shelf transition zone, hereafter referred to as the Patos Lagoon inlet for the purpose of geophysical comparison with other outflow systems.

Flow discharge is forced through a narrow 500 m wide channel, approximately 20 m deep, marking the narrowest cross-section of the system

(Fig. 1b, c). The inlet is fixed by jetties extending roughly 4 km offshore. These structures constrain the flow, accelerating currents and directly shaping the spatial distribution of the effluent jet. Previous geomorphological and hydrodynamic research suggests that mouth morphology and bathymetric variability are key factors in structuring the flow and the system's hydrodynamic response (Kirinus et al., 2012). As a result, the discharge is predominantly ebb-directed, carrying low-salinity waters and generating a buoyant plume on the adjacent shelf (Möller et al., 2001; Cruz & Schettini, 2025).

The local astronomical tide is microtidal and mixed, with a diurnal dominance, featuring a mean range of 0.4 m (Möller et al., 2007). The influence of the astronomical tide on local circulation is minor compared to the effects of atmospheric forcing and river discharge. Water level variability and circulation in the region are dominated by meteorological components associated with synoptic systems (cold fronts), which control the inflow and outflow of water through the mouth (Santa-Rosa and Schettini, 2024; Barros et al., 2025; Miranda et al., 2026).

The system's mean river discharge is on the order of 2,400 $m^3 s^{-1}$ (Vaz et al., 2011), exhibiting strong interannual variability, with values reaching approximately 12,000 $m^3 s^{-1}$ during intense flood periods (Hartmann and Schettini, 1991; Marques et al., 2014), reflecting the system's capacity to export large volumes of freshwater and suspended material to the adjacent shelf (Simão

et al., 2026). Most of the fluvial input occurs through the Guaíba system at the northern end of the lagoon (Fig. 1a). Notably, there is no direct relationship between river discharge and the water flux through the mouth, as the latter is primarily determined by wind conditions (Santa-Rosa and Schettini, 2024).

Local winds affect water level variability within the lagoon, while remote winds dominate the circulation in the estuary–shelf transition zone (Hartmann and Schettini, 1991; Möller et al., 1996; Möller et al., 2001; Fernandes et al., 2005). Predominant north-easterly winds induce an oceanward barotropic pressure gradient, intensifying freshwater discharge and favouring plume expansion onto the continental shelf. In contrast, south-westerly winds promote coastal sea-level rise through Ekman transport, establishing a landward pressure gradient and favouring flood conditions within the estuary. During high river discharge episodes (exceeding approximately 4,000 $m^3 s^{-1}$), however, the south-west wind effect is overcome by the fluvial forcing, resulting in a persistent ebb regime (Möller et al., 2001; Monteiro et al., 2011). Prevailing winds in the region are aligned along the N-NE and S-SW quadrants, roughly parallel to the main axis of the Patos Lagoon, which promotes efficient hydrodynamic responses throughout the lagoon system (Möller and Castaing, 1999). This geometric configuration contributes to the strong modulation of estuarine circulation and the coastal plume by synoptic events, affecting plume orientation, extent, and persistence, as well as its interaction with shelf circulation (Ávila and Calil, 2018).

Previous studies on the Patos Lagoon plume have been predominantly based on numerical modelling. Initial research investigated the structure and seasonal variability of the regional plume using hydrodynamic models with relatively limited spatial and temporal resolution (Piola et al., 2005; Soares et al., 2007a,b). Subsequent investigations furthered the understanding of the physical mechanisms controlling plume formation and behaviour, highlighting the roles of wind forcing, stratification, and three-dimensional circulation (Marques et al., 2009; Monteiro et al., 2011). Additionally, studies have addressed the importance of straining and advection processes in modulating stratification within the Patos Lagoon coastal plume (Marques et al., 2010).

Burrage et al. (2008) and Zavialov et al. (2018) explored the interaction between the Patos Lagoon plume and the Rio de la Plata buoyancy currents using remote sensing. While these studies enhanced the understanding of surface dynamics, direct in-situ measurements of the plume's sub-surface structure remain lacking, especially in the near-field zone. Although the internal dynamics within the Rio Grande Channel were recently detailed by Barros et al. (2025), describing the inlet as a highly energetic and stratified environment, the region immediately seaward of the mouth (Fig. 1) remains poorly sampled. In this area, the interplay between synoptic forcing, high river discharge, and complex bathymetry drives intense hydrodynamic variability. Consequently, this region is particularly relevant for investigating mixing processes, energy dissipation, and plume dynamics at the estuary–shelf interface.

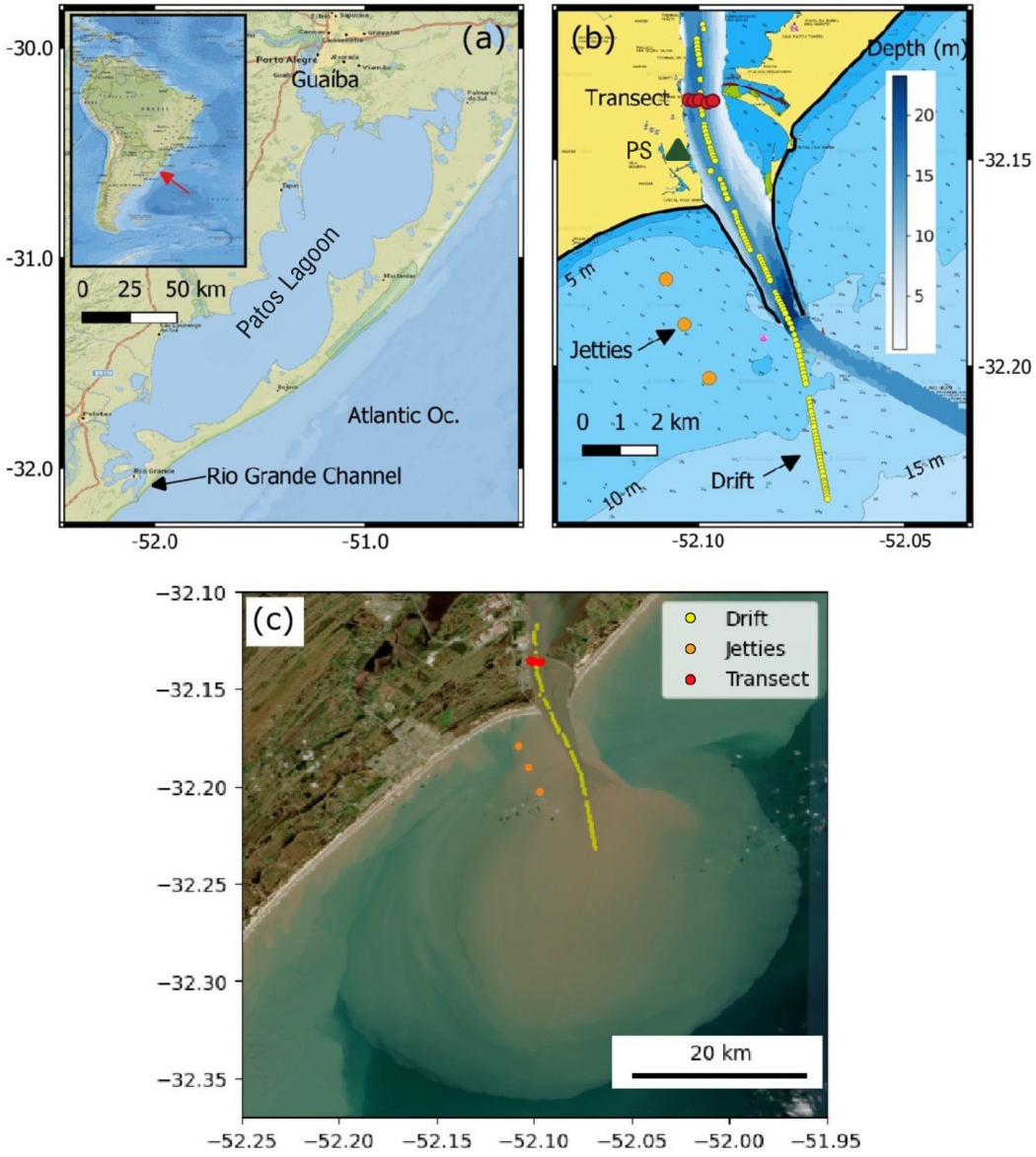


Figure 2: Study area location and sampling design. **(a)** Regional setting showing the Patos Lagoon choked system and its connection to the South Atlantic Ocean via the Rio Grande Channel. **(b)** Detailed view of the estuarine–shelf transition; yellow dots represent the Lagrangian track (Drift), orange dots indicate the baseline stations near the breakwaters (Jetties), and red dots show the cross-

channel section (Transect). The green triangle (PS) indicates the Rio Grande Pilot Station, the source for meteorological and water level data. Bathymetric contours and the nautical chart emphasize the jetty-constrained morphology. **(c)** Sampling stations overlaid on a Sentinel-2 true-colour image acquired on 18 July 2022, displaying the turbid surface plume during the survey period. This figure was created using QGIS. Panel (a) is based on the XYZ tiles from Esri National Geographic. Panel (b) is based on Brazilian Navy nautical chart No. 2110, available as a GeoTIFF at: https://www.marinha.mil.br/chm/dados-do-segnav/cartas-raster.

5.3. Materials and Methods

5.3.1. Fieldwork Design and Data Collection

The fieldwork was designed to capture the spatial variability of the vertical structure of current velocities, water properties, and mixing along the thalweg over the transition from the lagoon inlet and channel to the adjacent shelf, and into the buoyant plume beyond the jetties. The survey was conducted on 18 July 2022, coinciding with a Sentinel satellite overpass with clear-sky conditions, enabling a spatial match between in-situ data and the surface extent of the plume (Fig. 1c). During the field survey, outflow currents predominated, consistent with the conditions described in Section 2, where inflow and outflow at the mouth are

primarily modulated by a subtidal wind-driven regime, with astronomical tides playing a minor role.

Considering the limited influence of astronomical tides in the region, the sampling strategy prioritized spatial coverage over tidal phase, and the field campaign was organized into three segments: thalweg drift (Drift), inner shelf outside the jetties (Jetties), and cross-sectional transect (Transect), as referred to hereafter (Fig 1). The Drift segment collected over ~2h and 20min (11:21-13:40 LT) represents the main dataset of the experiment, aiming to capture the longitudinal transition from channelized flow to the early buoyant plume evolution. This segment involved a Lagrangian drift along the thalweg of the channel (with the boat moving passively with the outflow), represented by yellow dots in Figure 1b and 1c, totalling 108 microstructure profiles collected over approximately 13 km. While small adjustments were required inside the channel to compensate for wind-induced drag and maintain the boat within the thalweg, no corrections to the track were made once outside the inlet. The microstructure profiles were collected with a Rockland Scientific MCTD, which will be elaborated upon later in this section.

Subsequently, two complementary sampling segments were performed to characterize the boundary conditions. The Jetties segment (14:30-14:50 LT) was conducted on the inner shelf adjacent to the jetties (orange dots, Fig. 1b and 1c) to provide baseline values of TKE dissipation outside the buoyant plume,

comprising 17 microstructure profiles across three stations. Finally, the Transect segment (15:45-16:30 LT) consisted of a cross-channel section at the upstream portion of the study area (red dots, Fig. 1b and 1c). This segment included 26 profiles distributed across five stations (~ 5 profiles per station), designed to capture cross-channel hydrographic variability and quantify the volume outflow discharge during the survey.

During the Drift, Transect and Jetties sampling, current velocities were recorded concurrently using a vessel-mounted Teledyne RDI Workhorse 1200 kHz Acoustic Doppler Current Profiler (ADCP) operating in bottom-tracking mode. The instrument was configured with a ping interval of 0.5 s and a vertical bin size of 0.25 m, with the first measurement bin located approximately 1.5 m below the water surface. Horizontal positioning was determined via a GPS unit directly connected to the ADCP system, with an estimated positional uncertainty of ~5 m. The ADCP operated continuously throughout the field campaign, providing uninterrupted velocity measurements along the survey track. The total water flow across the transect segment was obtained from direct measurements using an ADCP, processed with the WinRiver II software provided by Teledyne RDI.

Salinity and temperature vertical profiles were recorded with a Rinko Profiler CTD (by JFE Advantech LTD) and with a Conductivity-Temperature Sensor (JAC CT) integrated into a Rockland Scientific microstructure profiler (MCTD). The MCTD recorded shear by two orthogonally mounted shear probes

operating at a sampling rate of 512 Hz. The shear profiles were used to estimate turbulence in terms of TKE dissipation rate (ϵ).

The MCTD was deployed a total of 152 times in the downward profiling mode at the locations indicated in Figure 1b and 1c, and lowered vertically using a weighted collar to ensure a controlled descent speed of approximately 0.8 m s^{-1} and an angle of attack below 5° (Lueck, 2013; Lueck et al., 2013; Ross et al., 2019a, Barros et al., 2025). The MCTD data were georeferenced and synchronized with the ADCP data. For each MCTD cast, there is a corresponding vertical profile of horizontal velocities, *u* and *v*, time-averaged over a one-minute interval.

Additional environmental data, including wind, water level, and Eulerian current measurements, were obtained from the Rio Grande Pilot Station (Fig. 1b). Wind observations were collected by a Davis Vantage Pro 2 meteorological station, recording at 5-minute intervals and averaged hourly. Water level and current velocity were measured with a moored Sontek Argonaut-XR 1.5 MHz ADCP, deployed at approximately 17 m depth. This instrument recorded 5-minute averaged profiles with a vertical bin size of 1.5 m.

Estimates of freshwater discharge into the Patos Lagoon were also incorporated, based on daily records from the primary tributaries. Discharge data were retrieved from Brazil's National Water Agency (ANA) Hidroweb database

(www.snirh.gov.br/hidroweb), using gauge stations from the Jacuí (85900000), Taquari (86720000), Caí (87170000), Sinos (87382000), and Camaquã (87905000) rivers. Additionally, discharge from the São Gonçalo Channel, which connects the Mirim Lagoon to the estuarine system, was provided by the Mirim Lagoon Agency (Agência da Lagoa Mirim – ALM/UFPel). The methodology used to aggregate and estimate river discharge followed the approach described by Santa-Rosa and Schettini (2024).

5.3.2. Data Analysis

5.3.2.1. Vessel-mounted ADCP data

The current velocity data recorded by the ADCP were trimmed within 10% of the bottom to remove erroneous data due to side-lobe effects. Velocities greater than 5% of the maximum flow were excluded, and any data ensemble with a signal return less than 85% good data was removed (Ross et al., 2019a). The resulting velocity time series for East-West (u) and North-South (v) components were rotated using principal component analysis (Thomson and Emery, 2014) to align with the longitudinal direction of the flow. For the data recorded in the channel, the decomposition considered two sectors with relatively similar orientation, up to the inlet. Seaward of the inlet, the currents were decomposed into cross-shelf and along-shelf components based on the coastline

orientation, determined by two reference points located approximately 10 km on either side of the jetties.

5.3.2.2. MCTD data

The rate of dissipation (ϵ) of TKE is derived from the measurements of velocity shear recorded by the shear probes on the MCTD (Lueck et al., 2020). Assuming that the turbulence is isotropic, the TKE dissipation rate is given by:

$$\epsilon = \frac{15}{2}\nu\overline{\left(\frac{\partial u}{\partial z}\right)^2} = \frac{15}{2}\nu\int_0^\infty \Psi(k)dk, \quad (1)$$

where ν is the kinematic molecular viscosity (10^{-6} m^2 s^{-1}), Ψ is the velocity shear spectrum, and k is the wave number (m^{-1}) (Lueck, 2013). This ϵ is expressed as the rate of dissipation of TKE per unit mass (W kg^{-1}, or equally, m^2 s^{-3}) (Thorpe, 2007).

The estimates of ϵ from each of the two shear probes affixed to the instrument were compared at each depth and if the value differed more than a factor of 2, the larger estimate was removed (Stips, 2005). Only two vertical profiles were discarded due to deviations from the operational thresholds of the angle of attack being more than 5° or the descent speed deviating from 0.8 m s^{-1}, representing less than 1.3% of the total casts. Correction for profiler vibration

was made using the method of Goodman et al. (2006). Individual wave number spectra for each component were calculated using a Fast Fourier Transform (FFT) with a length of 0.5 m and a time span of 2 s for each estimate of the rate of dissipation. Both calculated ϵ data sets were averaged and then used to quantify the vertical eddy viscosity (A_z). The calculations were done using the Matlab scripts provided by Rockland Scientific, and further pre-processed with Python (Schettini, 2021). Subsequently, all turbulence analysis and the computation of dimensionless stability metrics were performed using a dedicated Python codebase developed for this study (Barros, 2026). This secondary processing stage ensures the reproducibility of the mixing estimates and hydraulic parameters presented hereafter.

5.3.2.3. Turbulence Parameters and Vertical Mixing

To estimate vertical eddy viscosity (A_z) as a proxy for vertical mixing, the following procedure was adopted. First, along-channel and cross-channel velocity components from each transect were used to calculate the squared vertical shear (S^2), defined as:

$$S^2 = \left(\frac{\partial u}{\partial z}\right)^2 + \left(\frac{\partial v}{\partial z}\right)^2, \quad (2)$$

where *u* and *v* are the longitudinal and lateral flow components, respectively, and the coordinate *z* is positive upward. The buoyancy frequency (N^2) was used to estimate the stratification and is quantified as:

$$N^2 = -\frac{g}{\rho_o}\frac{\partial \rho}{\partial z}, \quad (3)$$

where *g* is the gravitational acceleration (9.8 m s^{-2}), and ρ_o is a reference density (1025 kg m^{-3}). The stratification stability parameter, also known as the dimensionless gradient Richardson number, is expressed as the ratio of buoyancy frequency to squared vertical shear, $R_i = N^2/S^2$, and was calculated to quantify the influence of stratification on mixing (Monismith, 2010).

From R_i, the flux Richardson number was obtained following Venayagamoorthy & Koseff, 2016, as a scale for mixing efficiency (Holleman et al., 2016; Gregg et al., 2018; Ross et al., 2019a):

$$R_f = 0.25\ (1 - e^{-7R_i}\ ). \quad (4)$$

According to Kay and Jay, 2003, in stable stratified flow, R_f is the fraction of total TKE production that is lost to buoyancy, increasing the potential energy of the water column. The mixing coefficient Γ_m is denoted by the mixing efficiency R_f.

$$\Gamma_m = \frac{R_f}{1-R_f}. \quad (5)$$

The vertical eddy viscosity, a proxy of mixing, was calculated as follows (Kay and Jay, 2003; Huguenard et al., 2015; Ross et al., 2019a):

$$A_z = \Gamma_m \frac{\epsilon}{S^2} \ . \quad (6)$$

The buoyancy Reynolds number is calculated as:

$$Re_b = \left(\frac{L_o}{L_k}\right)^{4/3} = \frac{\epsilon}{\nu N^2} \quad (7)$$

where the L_o / L_k is the ratio between the Ozmidov length scale and the Kolmogorov length scale (larger scale over smaller scale of turbulence). The Re_b is a parameter used to indicate the impact of density stratification on turbulence (Barros et al., 2025) and may be referred to in the literature by different names such as the turbulent activity parameter, activity number, strain-based Froude number, Gibson number, or buoyancy Reynolds number (Stacey et al.,1999; Shih et al., 2005; Monismith, 2010; Holleman et al., 2016). The magnitude of Re_b defines distinct regimes in the interaction between buoyancy and turbulence: for $Re_b > 200$, small-scale turbulence is unaffected by stratification; for $15 < Re_b < 200$, the effect of stratification progressively extends to smaller and smaller scales; and for $Re_b < 15$, stratification becomes dominant, resulting in the

complete suppression of turbulence (a phenomenon often referred to as 'killing turbulence') (Gargett et al., 1984; Ivey et al., 2008; Monismith, 2010).

5.3.2.4. Internal Froude Number Calculation

The internal Froude number (Fr_i) is a dimensionless measure of the ratio between inertial and buoyancy forces. It was calculated following (Hetland, 2010; McPherson et al., 2020):

$$Fr_i = \frac{U}{\sqrt{g'h}} \quad (8)$$

where U is the mean velocity of the upper layer relative to the lower layer, and h is the thickness of the low-density surface layer. The term $\sqrt{g'h}$ represents the internal wave speed, where g' is the reduced gravity, defined as $g' = g(\Delta\rho/\rho_0)$.

Determining h requires identifying the pycnocline depth. Within the channel, this was defined by the maximum vertical density gradient ($\partial\rho/\partial z$) for each density profile. In the offshore region, however, the strongest vertical density gradient occurs in the plume layer. The upper layer thickness in the offshore profiles was determined using a profile-shape criterion, defined as the depth at which the density profile transitions from a strongly stratified upper layer (plume) to a nearly homogeneous underlying water mass (coastal water). This approach

identifies the base of the buoyant plume while avoiding spurious detection of near-surface gradients.

The flow regime is considered subcritical if $Fr_i < 1$, indicating that buoyancy forces dominate over inertia (potential energy dominance). In this state, stratification is strong, and internal waves can propagate upstream; the plume tends to be stable and spread horizontally (Nash and Moum, 2005; Hetland, 2010). Conversely, if $Fr_i > 1$, the flow is supercritical, meaning inertial forces dominate (kinetic energy dominance). In this regime, stratification is insufficient to constrain the flow, potentially leading to turbulent mixing and density jumps (Horner-Devine et al., 2015; Geyer et al., 2017). A hydraulic jump may occur during an abrupt and turbulent transition where the flow shifts from a supercritical to a subcritical state (Dorrell et al., 2016; Thorpe et al., 2017).

5.3.2.5. Channel Morphology

In order to understand the influence of channel morphology on the measured and derived variables, cross-sectional areas along the channel were calculated. The inner channel was divided into 57 cross-sections, and the area of each section was estimated by constructing a closed polygon bounded above by the water surface and below by a high-resolution bathymetric survey conducted in 2024 using a single-beam echosounder and DGPS positioning (Fig. 1b).

For each section, a reference line was defined between two control points, and all bathymetric data within a lateral buffer of ±50 meters from this line were considered. To project the bathymetric points onto the local reference frame of the transect, each point (*x, y*) was expressed in terms of its longitudinal ($d_{\parallel}$) and perpendicular ($d_{\perp}$) distances:

$$d_{\parallel} = (x - x_0).u_x + (y - y_0).u_y \quad (9)$$

$$d_{\perp} = \left|(x - x_0)(-u_y) + (y - y_0)u_x\right| \quad (10)$$

where (x_0, y_0) is the starting point of the transect, and (u_x, u_y) is the unit vector in the direction of the transect. Points satisfying $0 \leq d_{\parallel} \leq L$ and $d_{\perp} < 50$ meters (with L being the transect length) were retained for area calculation.

The bathymetric profile was ordered along the transect axis to form the lower boundary of the polygon, while the water surface was assumed to be locally horizontal and defined by a straight line between the transect endpoints. This assumption is reasonable for short cross-sections and allows the area to represent a first-order approximation of the wet section at the time of sampling. The polygon was constructed by concatenating the surface line with the reversed bathymetric profile.

5.4. Results

5.4.1. Environmental Conditions and Inner Channel Dynamics (The Transect Segment)

The environmental conditions during the survey favoured the outflow of lagoon waters and the formation of a buoyant plume. To characterize this state, the river discharge of the main tributaries, along with water level, wind vectors in meteorological convention, and current velocities measured in the channel at the Pilot's Station (Fig. 1b) during the days preceding the survey, are shown in Figure 2. On the day of the fieldwork (18 July 2022), the gauged river discharge was approximately 6,900 $m^3\ s^{-1}$ (Fig. 2a), which is significantly higher than the estimated average flow of 3,707 $m^3\ s^{-1}$ for the same month.

The gauged river discharge represents the freshwater inflow to the lagoon; however, it does not necessarily correspond to the discharge at the lagoon mouth due to storage, mixing, and exchange processes within the lagoon (Santa Rosa and Schettini, 2024). The total discharge at the lagoon mouth, measured across the Transect segment, reached 9,400 $m^3\ s^{-1}$, with an average salinity of 6 $g\ kg^{-1}$ (Fig. 3b). Using the observed coastal salinity during the survey (~28 $g\ kg^{-1}$) as a reference, the freshwater discharge was estimated at 7,650 $m^3\ s^{-1}$. The difference between the gauged river discharge and the actual freshwater flow at the lagoon's mouth can be attributed to wind-driven water level variations along the lagoon and the residence time of water parcels within the system.

Water level variability during the survey was minimal, fluctuating by approximately 0.20 m (Fig. 2b). Wind speeds were relatively weak compared to the preceding days (Fig. 2c), blowing from NNW to W and ranging between 1.8 and 5.4 m s^{-1}. The current flowed seaward throughout the entire water column during the fieldwork (Fig. 2d), with velocities ranging from 0.8 m s^{-1} near the bottom to 2.2 m s^{-1} near the surface, without reversal. These results from the moored ADCP corroborate the Transect observations (Fig. 3a), showing outflow across the entire water column, with higher velocities of approximately 2 m s^{-1} concentrated at the surface and along the main axis of the channel. Nevertheless, this condition represented a significant variation compared to the previous days in the interval, during which the current had been flowing in the opposite direction due to the passage of a frontal system with up-estuary winds. This high-discharge, outflow-dominated state provides the boundary conditions for the plume development analysed in the following section.

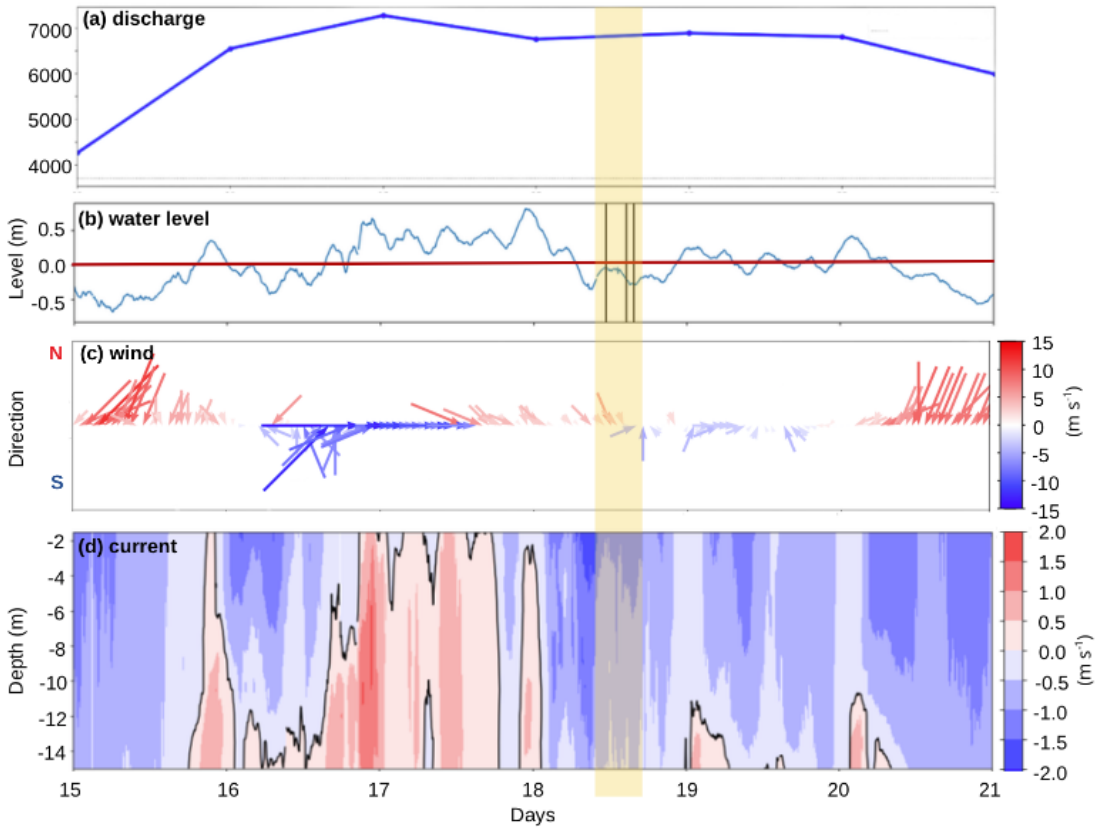


Figure 2: Environmental conditions between 15 and 21 July 2022, with the vertical yellow bar representing the survey period. **(a)** Gauged river discharge of the Patos Lagoon (m^3 s^{-1}), **(b)** Water level (m) measured in the channel, where the three vertical lines indicate the start moment of each section: Drift, Jetties, and Transect. **(c)** Vector plot of wind velocity (m s^{-1}) in meteorological notation, where blue represents southerly winds (blowing towards the north) and red represents northerly winds (blowing towards the south). **(d)** Hovmöller diagram of the along-channel current velocity (m s^{-1}) measured in the channel, where red indicates inflow (flood) and blue indicates outflow (ebb).

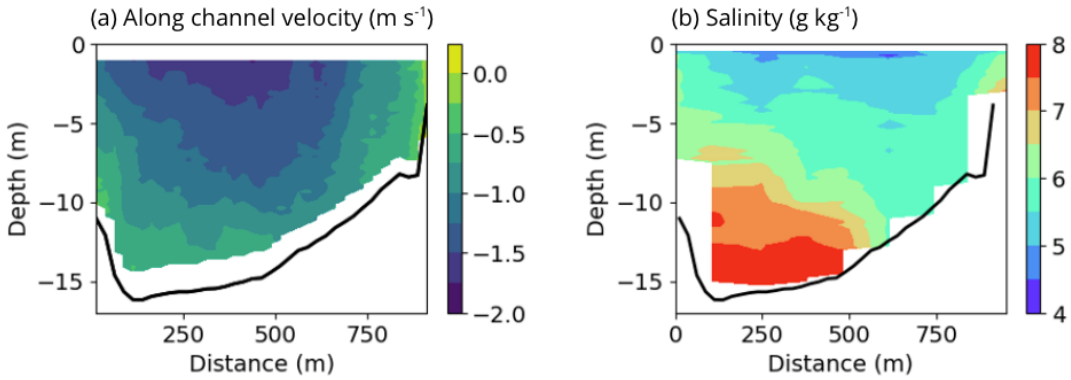


Figure 3: Cross-sectional distribution of **(a)** along channel current velocity (m s^{-1}; negative values indicate outflow) and **(b)** salinity (g kg^{-1}) at the Transect segment, characterizing the lagoon outflow during the survey.

5.4.2 Estuary–Shelf Transition and Near-Field Plume (The Drift Segment)

The spatial distributions along the Drift segment are presented in scatter plot diagrams, where vertical profiles feature a 0.5 m resolution and horizontal positioning corresponds to each cast's location. This graphical representation underscores the extensive sampling density achieved during the campaign and allows for the identification of spatial coherence between neighbouring profiles. Such high-resolution visualization is particularly relevant for properties with strong spatial variability, such as TKE dissipation (ϵ) and the Richardson number (R_i), ensuring that the observed structures reflect genuine physical features captured at the sampling sites.

5.4.2.1. Water Mass Characterization and Vertical Structure

The spatial distribution of temperature, salinity, and density across the Drift segment illustrates the horizontal and vertical development of the estuarine plume as it exits the channel. Within the channel (distance ≤ ~8.5 km), salinity (Fig. 4a) ranged from 7 to 13 g kg^{-1}, with a relatively clear vertical distinction at the density interface (black dashed line in Fig. 4a-c). In the outer region (distance ≥ ~8.5 km), vertical variability intensifies, with values spanning 7 to 28 g kg^{-1} near the mouth, followed by a gradual increase in surface salinity as the plume disperses offshore. Temperature (Fig. 4b) shows less variability than salinity (< 1°C) but remains consistent with salinity patterns. Consequently, the density distribution (Fig. 4c) closely mirrors salinity, ranging from 1005 to 1021 kg m^{-3}.

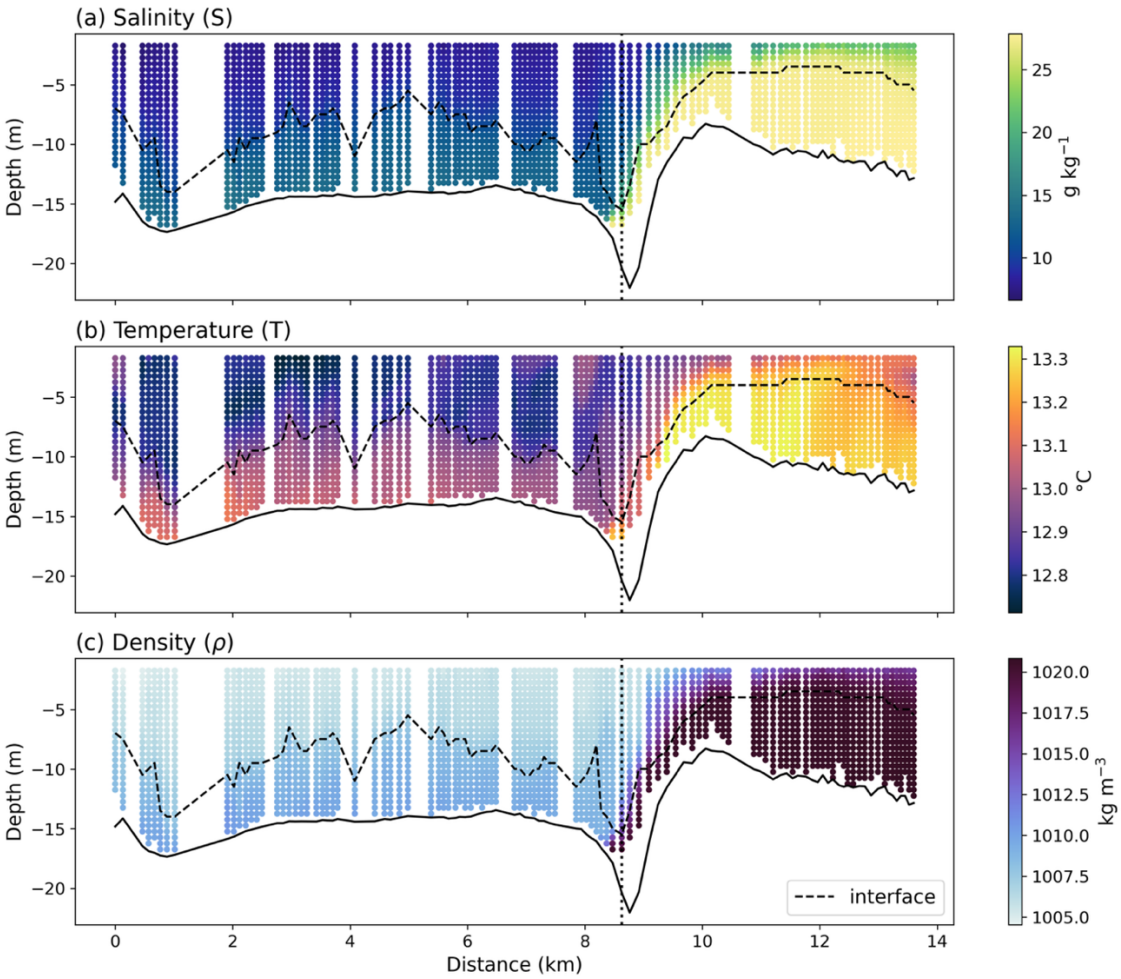


Figure 4. Spatial distributions of **(a)** salinity (g kg^{-1}), **(b)** temperature (ºC), and **(c)** density (kg m^{-3}). The dashed line indicates the interface position between layers. The vertical dotted line marks the position of the mouth (inlet). Distance (km) is measured from the first upstream profile within the channel.

The transition from the laterally constrained channel flow to the unconstrained shelf environment is marked by significant morphological changes and baroclinic adjustments (Chao and Boicourt, 1986; Valle-Levinson et al., 1996). The T-S diagram (Fig. 5) illustrates the thermohaline structure resulting

from these adjustments and the subsequent mixing stages of the sampled waters, distinguishing the inner region (warm tones) from the outer region (cold tones), with colour shading indicating depth. The distribution reveals three primary water masses: (i) low-salinity (< 15 g kg^{-1}), representing estuarine water influenced by river discharge and meteorological forcing; (ii) an intermediate salinity range (15-27 g kg^{-1}), reflecting active mixing between estuarine and coastal waters; and (iii) high-salinity (> 27 g kg^{-1}), representing relatively homogeneous coastal water.

The low-salinity partially mixed estuarine water (< 15 g kg^{-1}) is composed of two main branches: the first with a vertical shape (yellow, with salinity < 8 g kg^{-1}) represents near-surface estuarine water, while the second (red, with salinity ranging from 8 to 15 g kg^{-1}) exhibits a diagonal trend, representing the deeper estuarine layer. The intermediate mixing region (majority of blue points, 15-27 g kg^{-1}), shows the data also along a well-defined diagonal trend, reflecting coupled variations in temperature and salinity and thus active conservative mixing between estuarine and coastal waters, representing the plume waters over the shelf. At higher salinities, the distribution becomes more vertically clustered again (purple cluster, > 27 g kg^{-1}), representing a second, relatively homogeneous water mass associated with coastal waters. This most saline and deeper water represents the regional coastal water under the influence of the La Plata River plume, a buoyant coastal current that flows northward along the southwestern Atlantic shelf and episodically reaches the study area, modulating the

thermohaline structure of the adjacent coastal waters, particularly during winter (Campos et al., 2008).

The geometry of these branches indicates the nature of the mixing processes (Miranda et al., 2002). Additionally, the marginal histograms (Fig. 5) highlight the sampling density, where the bimodal salinity distribution underscores the clear separation between the estuarine core and the coastal water. In contrast, the more continuous temperature distribution, given its relatively small range (~0.6 °C) reflects the subtle thermal gradient across the plume, confirming that density remains primarily salinity-driven in this near-field region.

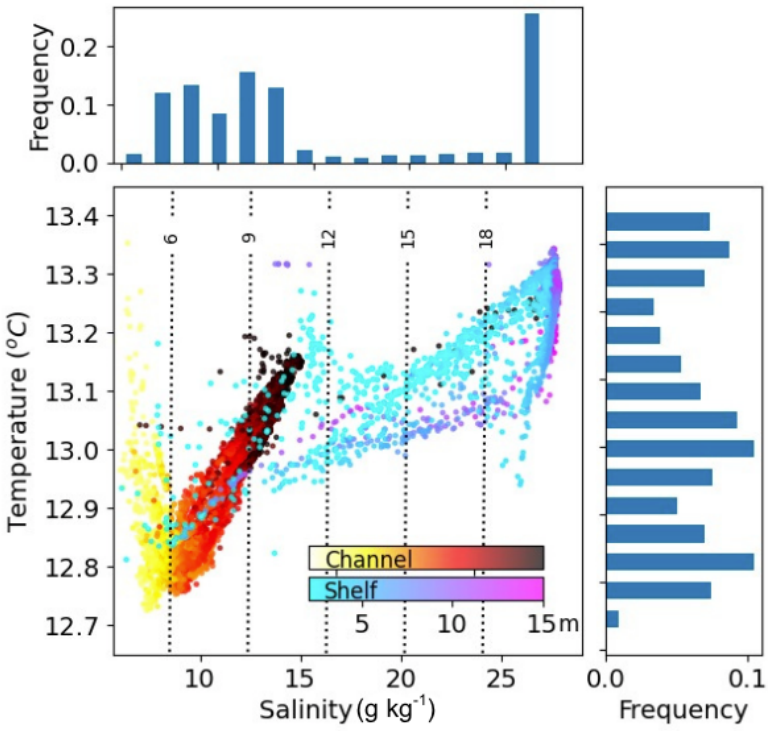


Figure 5. Temperature–Salinity (T–S) diagram and frequency histograms of salinity (top) and temperature (right) for the Drift segment. The central panel

shows temperature (°C) versus salinity (g kg^{-1}), with dotted vertical lines indicating density anomaly (σ_t) values of 6, 9, 12, 15, and 18 kg m^{-3} (referenced to 1000 kg m^{-3}). The colour bar distinguishes data from the Channel (warm tones) and the Shelf (cold tones), with shading representing the sampling depth (m).

The high-resolution vertical density profiles exhibit the structural evolution of the water column across the channel-to-shelf transition (Fig. 6). Within the channel (red-toned lines), profiles are clustered between 1005 and 1010 kg m^{-3}, with relatively weak vertical density gradients, especially when compared to other conditions in the same system (Barros et al., 2025), indicating a partially mixed water column. As the flow exits the jetties into the shelf (blue-toned lines), a sharp two-layer stratification emerges. In this outer region, surface density increases to 1012-1021 kg m-3, while the pycnocline rises and stabilizes at depths shallower than 5 m. Below this interface, density converges to values between 1020 and 1021 kg m^{-3}. This transition from a less stratified channel flow to a more strongly stratified near-field plume provides the physical context for the flow and mixing results presented next.

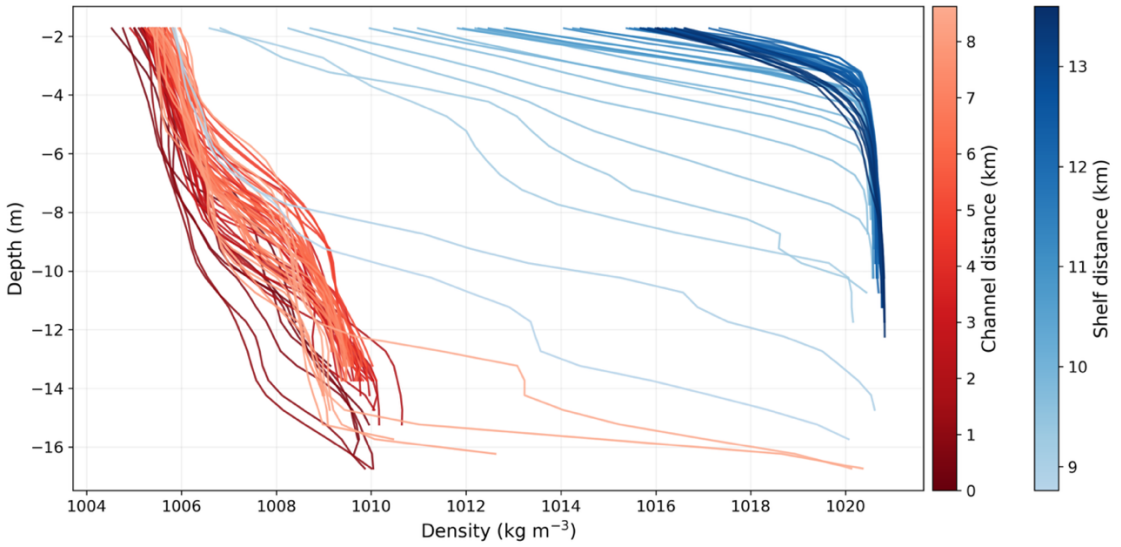


Figure 6. Vertical density profiles (kg m^{-3}) across the channel-to-shelf transition. Lines are colour-coded by distance (km) from the starting point of the drift segment. Red tones represent profiles within the inner channel (0-8.5 km) and blue tones represent profiles in the shelf region (9-13.5 km).

5.4.2.2. Flow Dynamics and Velocity Structure

The longitudinal velocity component (Fig. 7a) shows a predominantly seaward-directed (negative) flow throughout the entire water column, with higher velocities at the surface (up to ~1.8 m s^{-1}) that decrease with depth. A vertical gradient of the along-channel velocity occurs at the interface between the two density layers, indicated by the dashed line in Fig. 7a. Although this observation is subtle in the velocity data alone, it becomes more evident when viewed alongside the water property observations (Fig.4). However, beyond the inlet (km

8.5), this vertical gradient becomes more pronounced. The intensity of the outflow in the upper layer intensifies, exceeding 2.0 m s^{-1} just after the mouth at the estuary–ocean connection. The upper layer loses momentum as its thickness increases farther offshore (beyond km 11), while moving away from the source region. Below the interface, the velocity is significantly lower (typically < 0.5 m s^{-1}, representing less than 25% of the surface magnitude) and a flow reversal (positive values) occurs near the bottom in the outermost portion.

The cross-channel velocity component (Fig. 7b) within the inner channel exhibits magnitudes ranging from –0.51 to 0.41 m s^{-1}, reflecting a flow primarily aligned with the longitudinal axis. These lateral flow patterns change direction (shifting between positive and negative values) across the water column, especially along the layer interface, particularly in the region of highest constriction (approx. km 8). Once on the shelf (beyond km 9), the cross-shelf signal becomes dominant, reaching magnitudes of –0.68 m s^{-1} and showing consistency throughout the water column. This shift reflects that, once outside the channel's confinement, the plume's lateral flow responds mainly to shelf forcing, whereas the inner channel circulation reflects local morphological adjustments.

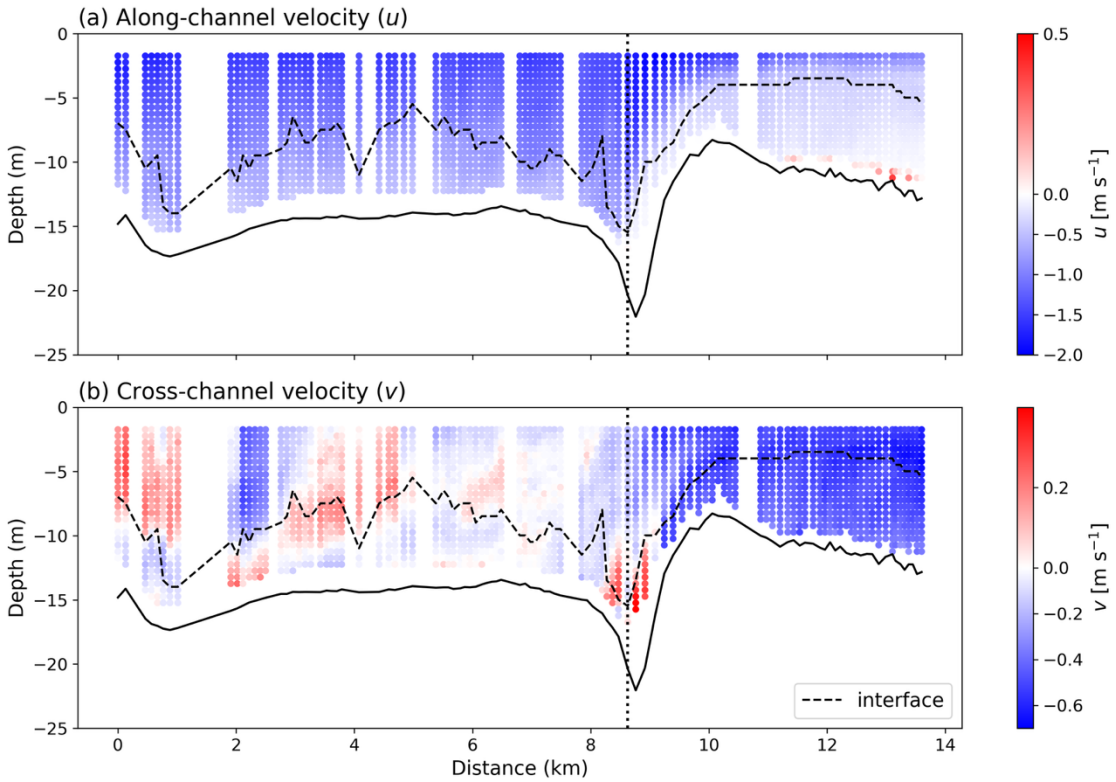


Figure 7. Spatial distributions of **(a)** along-channel and **(b)** cross-channel velocity components (m s^{-1}) synchronized with the MCTD profiles. The dashed line indicates the interface position between layers. The vertical dotted line marks the position of the mouth (inlet). Distance (km) is measured from the first upstream profile within the channel.

5.4.2.3. Turbulent Regimes and Stability Parameters

The turbulent kinetic energy dissipation rate (ϵ) along the section is presented in Figure 8. The values of ϵ vary across four orders of magnitude, ranging from 10^{-7} to 10^{-3} W kg^{-1}. The highest values were recorded in the region

immediately following the mouth (km 9-10) throughout the entire water column. This zone of high dissipation extends offshore within the surface layer above the interface. Below the interface on the shelf, dissipation values were relatively lower (10^{-6} W kg^{-1}). The lowest dissipation values (< 10^{-7} W kg^{-1}) were recorded within the channel in the mid-water column between km 5 and 7, in the vicinity of the density interface. This zone corresponds to the wider section that precedes the narrowing of the jetties towards the mouth.

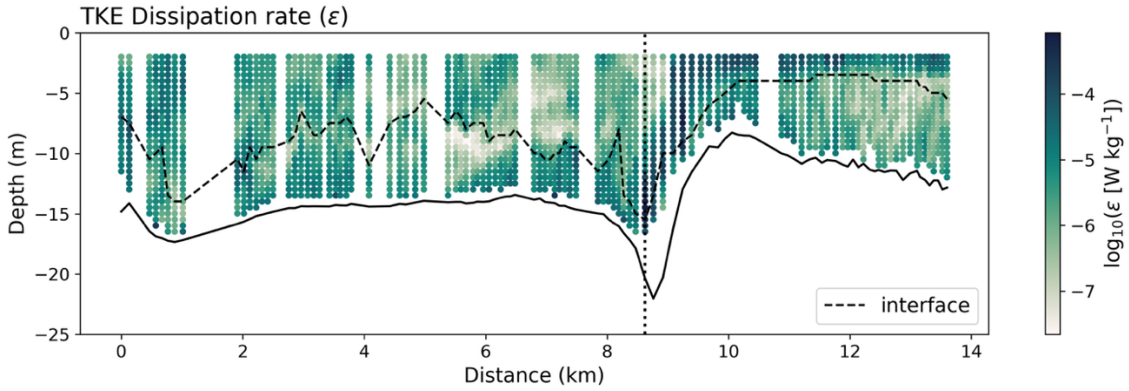


Figure 8. Spatial distribution of the turbulent kinetic energy dissipation rate (ϵ, log10(W kg^{-1})). The dashed line indicates the interface position between layers. The vertical dotted line marks the position of the mouth (inlet). Distance (km) is measured from the first upstream profile within the channel.

The spatial distributions of buoyancy frequency (N^2) and squared vertical shear (S^2), and the gradient Richardson (R_I) are presented in Figure 9. The buoyancy frequency (Fig. 9a) shows lower variability along the channel, with higher values coinciding with the pycnocline (interface). On the shelf, a more

intense vertical gradient is observed between the surface layer, presenting higher values (~10^{-1} s^{-2}), and the bottom layer (~10^{-5} s^{-2}). The spatial distribution of the squared vertical shear (Fig. 9b) is relatively consistent with the N^2 patterns. The highest S^2 values also occur at the transition between the inlet and the shelf, as well as within the shelf's surface layer (~10^{-1} s^{-2}). The largest S^2 values in the channel were co-located with the pycnocline.

The gradient Richardson number, R_i, was rescaled as log10(R_i /0.25), such that positive values reflect R_i > 0.25 and negative values reflect R_i < 0.25 (Fig. 9c), where Ri ≈ 0.25 represents a classical threshold below which stratified shear flows become susceptible to instability (Miles, 1961). Within the inner region of the inlet, values below 0.25 are predominantly concentrated in the surface layer, while values above this threshold occur especially around the interface. Near the mouth (vicinity of km 8.5), nearly the entire water column exhibits values above 0.25, forming a stable vertical barrier. In the outer region, a vertical decoupling is observed where the surface plume and the near-bottom layer present values below 0.25, whereas a persistent layer of values above 0.25 follow the stratified interface region, effectively isolating the plume from the deeper shelf waters.

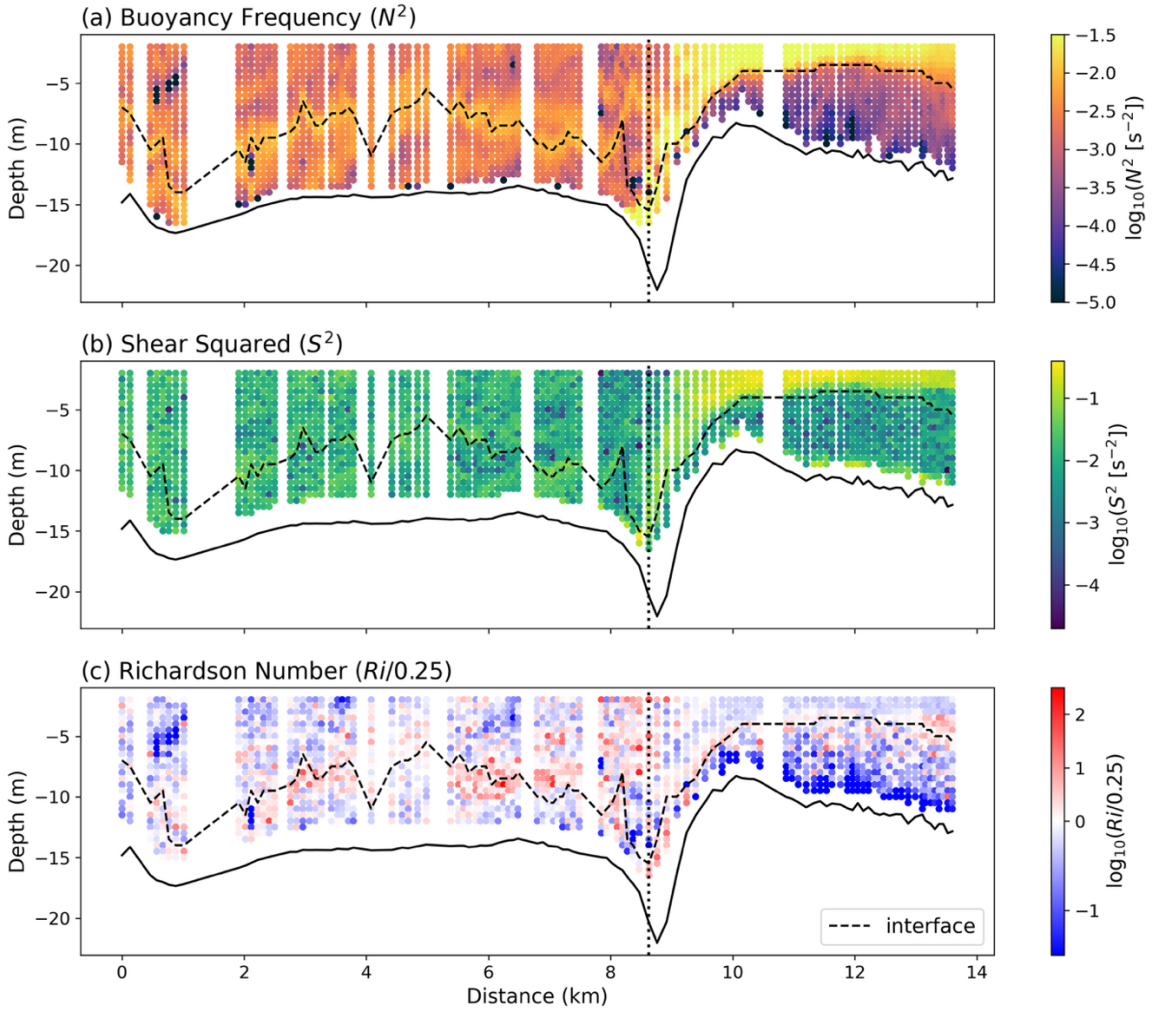


Figure 9. Spatial distributions of **(a)** buoyancy frequency (N^2, s^{-2}), **(b)** squared vertical shear (S^2, s^{-2}), and **(c)** gradient Richardson number normalized by its critical value (R_i/0.25). The dashed line indicates the interface position between layers. The vertical dotted line marks the position of the mouth (inlet). Distance (km) is measured from the first upstream profile within the channel.

The spatial distributions of the vertical eddy viscosity (A_z) and the buoyancy Reynolds number (Re_b) are presented in Figure 10. The vertical eddy viscosity exhibits values ranging from 10^{-6} to 10^{-1} m^2 s^{-1}, showing significant

vertical and longitudinal variability along the section (Fig. 10a). The lowest values occur primarily in the mid-water column between km 5 and 7. In contrast, the highest values are found near the seabed on the shelf, adjacent to the mouth at km 9.

The buoyancy Reynolds number was calculated as an indicator of the degree to which stratification suppresses turbulence. High Re_b values are observed throughout most of the channel (Fig.10b), particularly in the region between km 9 and 10, where values remain above 200 over the water column. Values between 15 and 200, which indicate that stratification is actively constraining turbulence, are specifically found in the mid-water column between km 5 and 7.5, as well as along the density interface in the channel, and near the offshore end of the section (km 13). Values lower than 15 appear at isolated points along the interface, with a notable cluster occurring within the pycnocline between km 5 and 7.5, which indicate that stratification is fully suppressing turbulence at these locations.

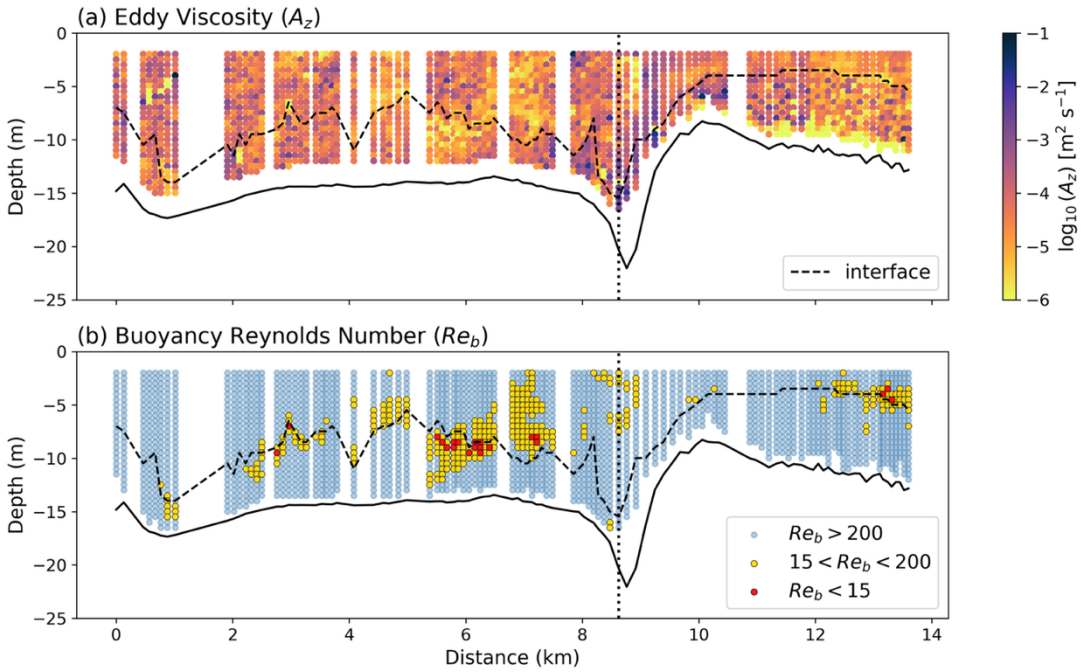


Figure 10. Spatial distributions of **(a)** the vertical eddy viscosity (A_z, m^2 s^{-1}), and **(b)** the buoyancy Reynolds number (Re_b). The dashed line indicates the interface position between layers. The vertical dotted line marks the position of the mouth (inlet). Distance (km) is measured from the first upstream profile within the channel.

5.4.3. Adjacent Inner Shelf Baseline (the Jetties Segment)

To contextualize the magnitude of the turbulence observed within the plume, the vertical profiles conducted in the Jetties segment serve as a baseline reference for the adjacent inner shelf. Compared to the high-velocity jet observed in the Drift segment, the current velocity profiles at the Jetties segment (Fig. 11a)

exhibit distinctly lower magnitudes and greater vertical uniformity, averaging to approximately 0.2 m s^{-1}. Nevertheless, the upper layer at Station 1 (green line), which is the outermost (most seaward) location, exhibited larger variations, reaching over 0.4 m s^{-1} at the surface. This behaviour is consistent with the density profiles (Fig. 11b), which indicate a more stratified water column at Station 1 compared to moderate stratification at Station 2 (blue line). Conversely, Station 3 (yellow line), which is located closest to shore, exhibits a nearly vertical density profile, indicating a well-mixed water column with no apparent pycnocline.

Under these conditions, the TKE dissipation rates (ϵ) at these stations (Fig. 11c) are significantly lower than those recorded in the main plume axis, ranging between 10^{-8} and 10^{-6} W kg^{-1}, with the minimum values occurring mid-water column, just below the pycnocline at each station. This is even the case for station 3, which has a nearly uniform density profile, although the values of ϵ are up to a magnitude smaller than the other two stations. Furthermore, *Az* fluctuates between 10^{-5} and 10^{-3} m^2 s^{-1} without a specific vertical pattern (Fig. 11d). The reduced velocities and relative uniformity, combined with the markedly lower stratification and dissipation at these reference points, confirm that the intense turbulent activity described in the Drift segment is an intrinsic process of the plume dynamics rather than a general characteristic of the inner shelf. This contrast highlights the unique turbulent signature of the plume, where internal structures are governed by localized mixing processes at the estuary–shelf interface.

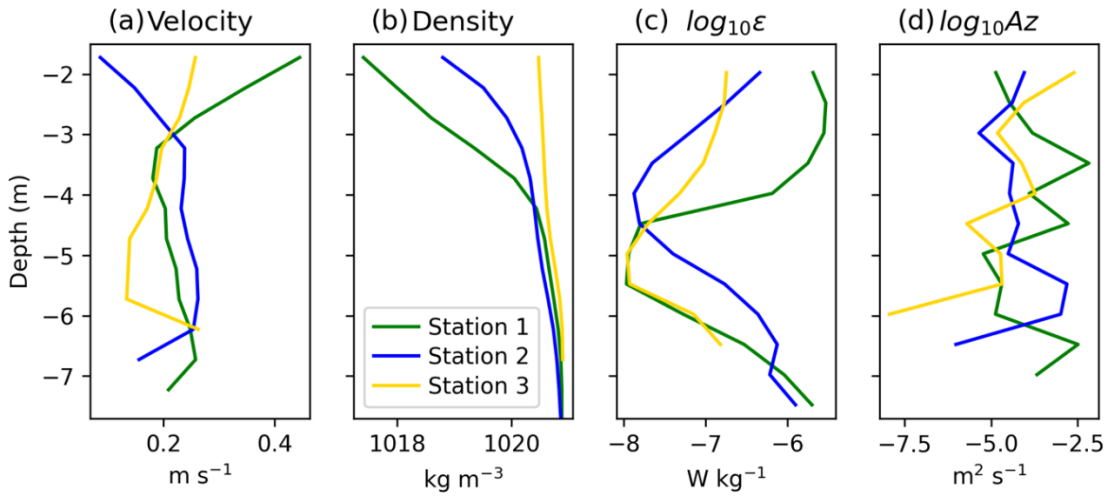


Figure 11. Vertical profiles of **(a)** current velocity (u, m s^{-1}), **(b)** water density (ρ, kg m^{-3}), **(c)** TKE dissipation rate (ϵ, W kg^{-1}), and **(d)** vertical eddy viscosity (A_z, m^2 s^{-1}) at the three baseline stations in the Jetties segment. Green, blue, and yellow lines represent Stations 1 (outermost), 2 (intermediate), and 3 (innermost), respectively. The x-axis tick labels in panels (c) and (d) indicate the logarithmic exponents.

5.5. Discussion

5.5.1. Representative Snapshot and Forcing Dominance

The field data were collected over a 5-hour window, from the beginning of the Drift segment (11:21 LT) to the completion of the Transect (16:30 LT). Despite the time elapsed between surveys, these results represent a quasi-synoptic

snapshot of the hydrodynamic conditions. In estuarine environments where astronomical tides are dominant, sampling designs must strictly adhere to hourly variations to capture tidal phases (Dyer, 1979; Kjerfve, 1990). However, in the Rio Grande Channel, astronomical tides play a secondary role, accounting for less than 20% of the current variance (Santa-Rosa and Schettini, 2024). As established by the spectral characterization for July 2022 (Barros et al., 2025), the system is dominated by low-frequency energy (periods > 25 h) associated with synoptic frontal systems.

This meteorological dominance ensured a quasi-synoptic state during the survey, characterized by minimal water level fluctuations (< 0.20 m; Fig. 2b) and a persistent, uniform ebb-directed flow (Fig. 2d). Such stationarity validates the comparison of data across different sampling moments, allowing the analysis to move beyond temporal variability and focus on the spatial processes and internal plume structure that define the estuary-shelf transition.

5.5.2. Morphological Control and Multi-regime Dynamics

The spatial distribution of the TKE dissipation rate (ϵ) along the drift segment highlights a clear maximum near the mouth and within the buoyant plume's surface layer. These high values align with the plume's 'lift-off' zone (MacDonald and Geyer, 2004) and exhibit a decay proportional to the distance

from the inlet (O'Donnell et al, 2008; McPherson et al., 2019). This maximum dissipation zone, associated with the plume's evolution over the quiescent coastal water, follows expected theoretical patterns for near-field river plumes (Horner-Devine et al., 2015).

Considering the internal channel dynamics a high degree of coupling with the local morphology is observed (Fig. 12). This contrasts with the finding of Barros et al. (2025), collected in the same study area with a 24 h difference (July 19th, 2022), where the presence of a salt wedge and a strong pycnocline acted to decouple the surface flow from the bottom topography and suppress turbulence. However, the present study (July 18th, 2022; Fig. 2) captures a fully flushed, inertia-dominated state, which shows peak discharge conditions that exhibit a more direct response to topographic control.

Within the channel, the localized decrease in ϵ (between ~km 4 and 7) directly corresponds to the expansion of the cross-sectional area, which redistributes kinetic energy and reduces local shear. As the flow approaches the final constriction near the mouth (km 8.5, dashed line), the abrupt reduction in cross-sectional area forces a convergence that drives current velocities to their maximum, resulting in the absolute peak of ϵ on the order of 10^{-3} W kg^{-1}. In this specific case, the morphological forcing is sufficient to overcome the vertical stability, triggering the intense mixing observed at the estuary–shelf interface.

Once the flow exits the jetties and enters the shelf, a reduction in ϵ is recorded (Fig. 12). Although the buoyant plume remains vertically restricted to the upper layer (Fig. 4a, c), the total loss of lateral confinement allows for a rapid horizontal spread. This transition from a topographically constrained jet to an unconfined plume leads to a significant decay in kinetic energy, marking the end of the high-energy near-field regime.

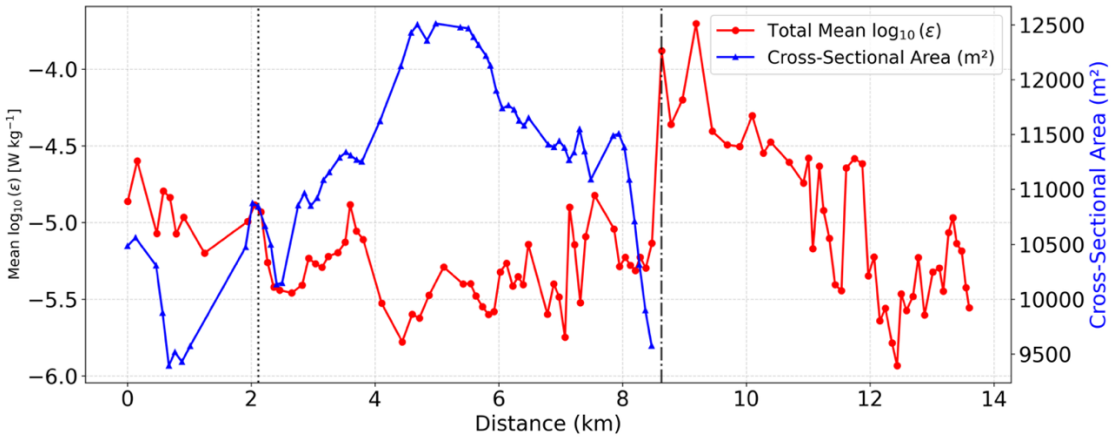


Figure 12. Longitudinal distribution of depth-average TKE dissipation rate (log 10 (ϵ), W kg^{-1}) and channel cross-sectional area (m^2) as a function of distance. The red line (left Y-axis) represents the average dissipation rate, while the blue line (right Y-axis) indicates the cross-sectional area along the Drift segment. The dotted vertical line marks the initial channel widening, and the dash-dotted vertical line indicates the maximum constriction point (mouth) at the estuary–shelf interface.

The rapid transition between the morphology-dominated state described here and the stratification-dominated regime observed on the following day

(Barros et al., 2025) highlights that the Patos Lagoon inlet operates under a highly complex non-stationary regime.

The observations presented here record the peak of a discharge event triggered by the relaxation of a meteorological sea-level set-up. As shown in Fig. 2d, the preceding landward wind stress promoted an inward water accumulation within the lagoon; once this forcing ceased, the resulting pressure gradient drove seaward flushing. This mechanism is a recurrent feature of the system's sub-tidal dynamics, where the passage of frontal systems every 5-7 days dictates the alternation between extreme outflow and salt-wedge intrusion (Möller et al., 2001; Fernandes et al., 2005).

These results suggest that in such microtidal environments, the temporal variability of mixing and turbulence is governed more by synoptic-driven events than by the predictable tidal cycle. The rapid shift observed here, from an inertia-dominated 'flushed' state to a stratified 'salt-wedge' intrusion state within only one day, highlights the importance of high-resolution spatial surveys to capture these transient regimes. In this context, the reduced tidal influence represents a key advantage, as it allows the isolation of wind-, discharge-, and morphology-driven processes that are often masked in strongly tidal systems. Therefore, these observations provide a useful framework for understanding the turbulent dynamics of estuarine–shelf systems, not only in microtidal environments but also in more complex settings where multiple forcings interact.

5.5.3. Hydraulic Regime and Internal Froude Number Analysis

Considering the hydrodynamic transition along the Drift segment, the potential for an internal hydraulic jump was investigated. Based on the vertical density distribution and layer-averaged velocities (Fig. 13a-c), the internal Froude number (Fr_i) was calculated to characterize the flow's criticality (Fig. 13d). Such phenomena are common in estuarine plumes where the flow transitions from a supercritical ($Fr_i > 1$) to a subcritical ($Fr_i < 1$) regime. These transitions are often interpreted through idealized models of internal hydraulic jumps, though their application to natural, high-energy flows requires careful consideration of mixing and layer entrainment (Thorpe et al., 2017).

Despite indicators of intense changes in plume velocity and thickness and interfacial mixing (Fig. 7 and Fig. 8), the results show that the system remained persistently supercritical throughout the entire Drift segment (Fig. 13). Inertial forces heavily dominated this system during the sampling period. High surface velocities (~2 m s^{-1}) resulted in elevated Fr_i values, as the flow's momentum far outweighed the stabilizing effect of buoyancy, even under sharp stratification. This persistent supercriticality along the main axis is consistent with flow dynamics observed in energetic channel-to-plume transition zones, where high inertia and high-velocity discharge prevent immediate hydraulic adjustment to subcritical conditions (Dorrell et al., 2016).

Such momentum implies that the flow is too rapid for internal disturbances to propagate upstream (Nash and Moum, 2005). This observed vertical structure, which is characterized by a thin, high-velocity surface layer over a saltier ambient water mass, follows the conceptual model of strongly stratified river plumes documented in large-scale systems (Nash et al., 2009). While the supercritical flow blocks the upstream migration of internal waves, the intense velocity gradient it creates is precisely what triggers localized mixing. The strong shear at the plume's base may promote Kelvin-Helmholtz (KH) instabilities, which drive the recorded peaks in ϵ, a process consistent with observations in other highly stratified discharge regions (e.g., Spicer et al., 2022).

The absence of a hydraulic jump may indicate that the transition to a subcritical regime likely occurs further offshore. This is supported by the progressive decrease in velocity, the deepening of the surface layer interface (McPherson et al., 2020), and the downward trend of Fr_i observed towards the offshore end of the Drift segment, particularly beyond km 12 (Fig. 13). The persistence of this supercritical state for several kilometres is a known feature of river plumes where the buoyant layer spreads laterally upon entering the ocean (Hetland, 2010; Horner-Devine et al., 2015). In these cases, the lateral straining of the shear layer acts as a sustained forcing mechanism for mixing, consistent with the elevated TKE values found in this region (Fig. 8), delaying the transition to a subcritical state until significant interfacial entrainment and expansion occur (Geyer et al., 2017).

The results indicate that the entire sampled domain (km 0 to 13) remains within the near-field as defined by Jirka et al. (1981), given that the system did not transition to a subcritical regime ($Fr_i > 1$ throughout). However, adopting the more detailed classification of Horner-Devine et al. (2015) allows for a finer distinction of the plume's evolution. The region up to the mouth (km 8.5) corresponds to the source region, where flow is governed by estuarine momentum and geometry. Beyond this point, despite the onset of lateral expansion and intense interfacial mixing (Fig. 8), the plume transitions into the buoyancy-forced region, while remaining persistently supercritical.

No evidence of a transition to the mid-field region, typically associated with reduced inertial dominance and a shift toward subcritical conditions, is observed within the spatial extent of this study. Instead, these results suggest that, in microtidal systems under high-discharge conditions, the near-field plume (Jirka et al., 1981) may extend for several kilometres onto the shelf, with the dynamical transition to subcritical flow occurring further offshore.

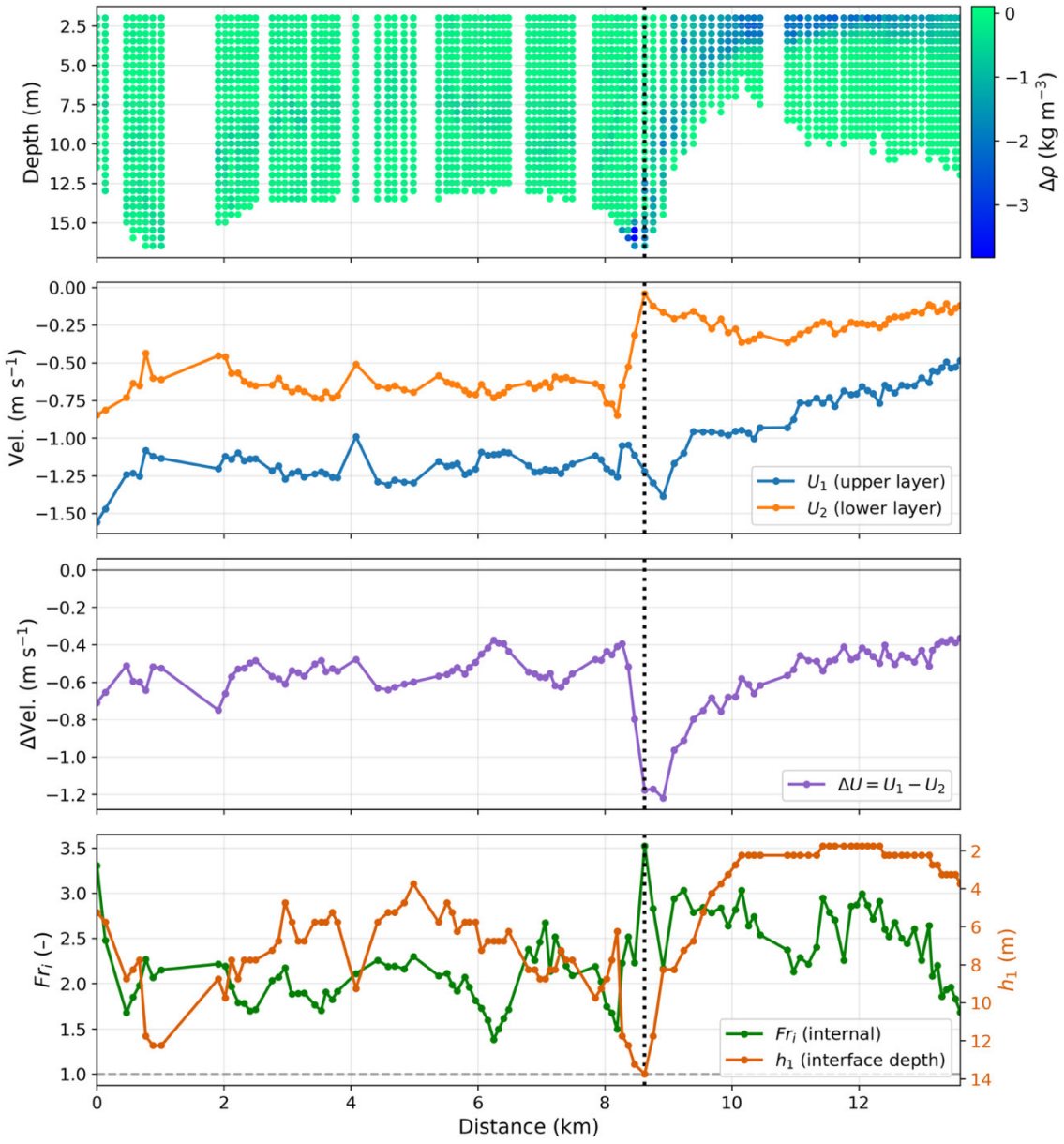


Figure 13. Two-layer parameters and Internal Froude Number as a function of distance. The figure consists of four vertical panels: **(a)** Vertical density gradient ($\Delta\rho$, kg m^{-3}) across depth; **(b)** Layer velocities, displaying the horizontal velocity (U, m s^{-1}) for upper (U_1) and lower (U_2) layers; **(c)** Layer velocity difference (ΔU, m s^{-1}); and **(d)** Pycnocline depth (h_1, m, right axis) and the Internal Froude

Number (Fr_i, left axis). The dashed horizontal line in panel (d) indicates the critical threshold (Fr_i = 1). The vertical dotted line marks the point of maximum constriction at the estuary–shelf interface.

5.5.4. Spatial Comparison and Estuarine Context

To evaluate the magnitude of the mixing processes observed, the maximum and minimum values of the primary hydrodynamic parameters were compared across the transition (Table 1) and contextualized with other estuarine systems globally (Table 2). The high-energy nature of the plume is initially evidenced by a peak in stratification (N^2 ~10^{-1} s^{-2}) and vertical shear (S^2 ~$10^{-0.5}$ s^{-2}) that concentrate in the outer portion of the channel, marking the region of intense interfacial interaction (Fig. 9a, b). These conditions promote elevated TKE dissipation (ϵ), with peaks on the order of 10^{-3} W kg^{-1} recorded immediately adjacent to the mouth (Fig. 8).

Table 1. Range of hydrodynamic and turbulent parameters observed inside the channel and on the adjacent shelf. Values represent the absolute minimum and maximum recorded during the drift survey.

	Drift (Channel)		Drift (Shelf)	
	MAX	MIN	MAX	MIN
Salinity (g kg^{-1})	12.6	6.6	27.9	7.1
Temperature (^0C)	13	12.7	13.3	12.7
Density (kg m^{-3})	1009.1	1004.5	1020.8	1004.9
Along-channel Velocity (m s^{-1})	1.7	0.5	2.0	0.4
N^2 (s^{-2})	10^{-2}	10^{-3}	10^{-1}	10^{-5}
S^2(s^{-2})	10^{-1}	10^{-4}	$10^{-0.5}$	10^{-5}
ϵ (W kg^{-1})	10^{-4}	10^{-6}	10^{-3}	$10^{-7.5}$
A_z (m^2 s^{-1})	10^{-2}	10^{-5}	10^{-1}	10^{-7}

As synthesized in Table 2, the maximum dissipation rates recorded at the Patos Lagoon mouth and its adjacent plume place this microtidal system among the most energetic estuarine environments documented in the literature. The alignment of this highly energetic inlet with world-class systems such as the Gironde and Columbia estuaries (Table 2) confirms that intense topographic constrictions can emulate the turbulent energy of macrotidal environments, even

in the absence of a significant tidal range. Indeed, the dissipation observed is an order of magnitude higher than values reported for other microtidal river plumes, such as Connecticut (O'Donnell et al., 2008), and Magdalena (Álvarez-Silva et al., 2026) rivers. Furthermore, the extreme inertial dominance observed during this survey leads to dissipation rates that match or exceed those recorded in larger meso- and macrotidal systems, such as Gironde (Ross et al. 2019a), Merrimack (MacDonald et al., 2007), Changjiang (Wang et al., 2020), Fraser (MacDonald and Geyer, 2004), and Hudson (Peters and Bokhorst, 2000) rivers. This energy level also significantly surpasses other topographically constrained environments in the Southern Hemisphere, including the Patagonian fjords, where tidal-driven turbulence at sills typically reaches values two orders of magnitude lower than those observed in the present study (Pérez-Santos et al., 2018).

Table 2. Global comparison of maximum TKE dissipation rates (ϵ) and tidal regimes across different estuarine systems.

System	Max. ϵ (W kg^{-1})	Tidal Regime	Reference
Patos Lagoon (Brazil)	10^{-3}	Microtidal	This study
Patos Lagoon (Brazil)	10^{-4}	Microtidal	Barros et al., (2025)
Columbia river (USA)	10^{-3} *	Mesotidal	Spicer (2022)
Gironde estuary (France)	10^{-3}	Macrotidal	Ross et al. (2019a)
Merrimack river (USA)	10^{-3}	Mesotidal	MacDonald et al. (2007)
Changjiang (Yangtze river -China)	10^{-3}	Mesotidal	Wang et al. (2020)
Fraser river (Canada)	10^{-4}	Mesotidal	MacDonald and Geyer (2004)
Hudson river (USA)	10^{-4}	Mesotidal	Peters and Bokhorst (2000)
Connecticut river (USA)	10^{-4}	Microtidal	O'Donnell et al. (2008)
Magdalena river (Colombia)	10^{-4}	Microtidal	Álvarez-Silva et al. (2026)
Patagonian fjords (Chile)	10^{-5}	Mesotidal	Pérez-Santos et al. (2018)

*Transient peaks reaching 10^{-2} W kg^{-1} have been recorded during extreme tidal-front interactions (Spicer, 2022).

Consistent with these high dissipation rates, the vertical eddy viscosity (A_z) reached maximum values of approximately 10^{-1} m² s^{-1} within the plume's interface (Table 1). This magnitude surpasses the maximum value of 10^{-2} m² s^{-1} previously observed in the Patos Lagoon inlet (Barros et al., 2025), reinforcing that under high outflow and specific morphological constraints, the Patos Lagoon inlet functions as a high-energy 'nozzle' that maximizes turbulent transport to the inner shelf.

5.5.5. Turbulence and Mixing Processes

The buoyancy Reynolds number (Re_b) was applied to map the various stages of turbulence along the transect section (Fig. 10b). Dominant values of Re_b > 200 (blue points) are observed throughout most of the water column, indicating that vigorous, fully developed, and isotropic turbulence prevails in the system. In these regions, buoyancy forces are unable to inhibit the vertical transport of mass and momentum, a state that coincides with the high internal Froude number (Fr_i) values recorded (Fig. 13). This competition between shear and buoyancy was previously identified as a key driver of turbulence within the Patos Lagoon inlet (Barros et al., 2025), where Re_b often serves as a more sensitive indicator of mixing states than traditional stability metrics, as it directly scales the turbulence levels relative to the buoyancy-controlled Ozmidov scale (Stacey et al., 2012).

However, turbulence is locally suppressed within thin layers directly associated with the pycnocline interface (dashed line in Fig. 10b). In these specific pockets, particularly between km 4 and 8, $Re_b < 15$ occurs (red points), indicating a regime where stratification inhibits turbulent fluctuations and vertical mixing is restricted toward molecular levels (Shih et al., 2005). Surrounding these suppressed zones, a transitional regime ($15 < Re_b < 200$, yellow points) marks the areas where turbulence is active yet anisotropic. In this zone, mixing efficiency is typically maximized, suggesting that despite the reported sharp stratification, the interfacial shear at the plume front is the primary driver for pycnocline erosion and subsequent saltwater entrainment. Such behaviour demonstrates that the presence of stratification does not necessarily imply the complete suppression of turbulent mixing, even under established stratification (Huguenard et al., 2015).

This spatial distribution suggests that while the plume's massive inertia maintains a state of generalized high-energy mixing, the density interface still acts as a localized, albeit intermittent, barrier to vertical transport. In this context, metrics based on the Richardson number (R_i) provide a consistent view of the potential for stratification-driven stability, particularly near the mouth and along the offshore interface, where it indicates a robust buoyancy barrier (Fig. 9c).

Nevertheless, the presence of these stable R_i layers does not necessarily imply the absence of mixing in such high-energy systems. While $R_i \approx 0.25$ is

commonly interpreted as a classical threshold for the onset of shear instability, this criterion is not sufficient to fully describe mixing in natural environments, as turbulence may be sustained for R_i values approaching unity under energetic forcing conditions (Simpson and Sharples, 2012). As observed between km 9 and 10, even where R_i suggests stability, the buoyancy Reynolds number (Re_b) and elevated ϵ confirm that turbulence remains vigorous enough to dynamically erode the interface. In estuarine environments, this corresponds to an intermediate regime ($0.25 < R_i < 1$), where mixing is not suppressed but instead modulated by the interplay of shear, straining, and advection (Giddings et al., 2011).

These results suggest that the classical R_i threshold alone may not fully capture the complexity of mixing dynamics in this system. Such limitations of the gradient Richardson number as a universal mixing proxy have been recently documented in other diverse high-energy, wind-dominated systems (Arevalo et al., 2022; Álvarez-Silva et al., 2026), where vigorous mixing and asymmetric hydrodynamic structures persist even under seemingly stabilizing density gradients. Therefore, the buoyancy Reynolds number (Re_b) provides a more robust description of turbulent efficiency in this energetically active plume, capturing the full spectrum of mixing states that traditional stability thresholds may overlook.

5.6. Conclusions

This study provides a detailed characterization of the estuary-shelf transition of a buoyant plume during a period of high discharge, revealing how inlet morphology and inertial dominance redefine mixing processes. The Patos Lagoon inlet, despite its microtidal regime, represents a high-energy benchmark for global estuary-shelf transitions, where the terminal jetty constriction acts as a morphological “nozzle” that forces the flow into an extremely energetic state. These high dissipation levels, reaching 10^{-3} W kg^{-1} near the mouth, are comparable to those found in major meso- and macrotidal systems and are driven by surface velocities of ~2 m s^{-1}, where inertial momentum far outweighs the stabilizing effects of buoyancy.

The along-channel evolution of turbulent kinetic energy (TKE) dissipation exhibits morphological control. Dissipation rates (ϵ) are significantly reduced within the inner estuary where the cross-sectional area widens, while maximum values occur near the jetty-confined mouth. Following this peak, ϵ values decrease progressively as the flow spreads offshore and the plume expands laterally. This spatial evolution of turbulence is consistent with the dominant hydrodynamic regime, which remains supercritical (Fr_i > 1) throughout the sampled area. This high-momentum state effectively blocks the upstream propagation of internal disturbances. The observed downward trend of Fr_i offshore and the subsequent deepening of the pycnocline, suggests that the

hydraulic adjustment toward subcritical conditions is displaced several kilometres onto the inner shelf.

Within this high-energy, supercritical regime, the interplay between buoyancy suppression and shear production is more effectively captured by the buoyancy Reynolds number (Re_b). This parameter accurately identifies the turbulence suppression observed near km 6, consistent with the localized minima in TKE dissipation. Furthermore, at the plume's frontal interface (~km 9), Re_b provides a clearer explanation of the mixing state than the Richardson number; while R_i identifies the structural potential for stability along the interface, Re_b reveals a state of vigorous, fully developed turbulence ($Re_b > 200$). This contrast highlights the limitation of relying solely on stability-based metrics to describe mixing in such energetic environments.

The findings of this study underscore the dominant role of inlet morphology in modulating the hydrodynamic and mixing regimes of river plumes, suggesting that similar dynamics may occur in other high-discharge, wind-dominated estuaries, particularly in microtidal systems. While these results provide a detailed characterization of the source and buoyancy-forced plume regions, explicitly closing the momentum budget remains a challenge for future research. In this context, targeted fieldwork focusing on hydraulic adjustments in the mid- to far-field plume will be essential to further elucidate mixing pathways in these active transition zones.

Chapter VI: Spatial variability of turbulent mixing in a highly stratified system

The research presented in this chapter provides a comprehensive analysis of the spatial variability in circulation and mixing dynamics within the Patos Lagoon estuary. Utilizing high-resolution observations from a micro-structure profiler (MCTD) and an Acoustic Doppler Current Profiler (ADCP), this study quantifies turbulent dissipation rates, vertical shear, and mixing efficiency across three strategic transects. The research identifies a complex interplay of driving mechanisms—ranging from channel curvature and differential advection to bottom stress—that modulate mixing even over short spatial scales. Notably, the study investigates how the funnel-shaped morphology influences current

acceleration and the counterintuitive suppression of mixing by stratification. By deconstructing these processes, this work contributes to a deeper understanding of salt-wedge hydrodynamics in microtidal estuaries worldwide.

This manuscript is authored by Débora Barros, Taylor Bailey, Lauren Ross, and Carlos A.F. Schettini, and is titled ***'Spatial variability of turbulent mixing in a highly stratified system'***. It was published in the ***Journal of Marine Systems*** and is available at **https://doi.org/10.1016/j.jmarsys.2025.104071**.

Abstract

This study investigates the lateral variability of circulation, salt distribution, and mixing processes along the highly stratified, micro-tidal Rio Grande Channel, which connects the Patos Lagoon and the Atlantic Ocean. High-resolution observations of current velocities (ADCP), water properties (CTD), and turbulent kinetic energy dissipation (microstructure profiler) were collected at three cross-sections located ~0.5, 3.5, and 8.8 km upstream of the lagoon mouth. The field campaign was carried out during an outflow condition, and the cross-sections capture conditions upstream of the salt intrusion limit (fresh water/vertically homogeneous), at the landward limit of salt intrusion (the tip of the salt wedge), and downstream of the salt intrusion (highly stratified). The results show that different physical mechanisms are responsible for promoting or suppressing mixing at each of the cross-sections. Secondary flows driven by baroclinic pressure gradients and acceleration due to curvature enhanced mixing in the cross-sections. Bottom-generated mixing was evident across all transects; however, vertical shear of the horizontal current velocities at the pycnocline emerged as the primary driving mechanism in the third (most-downstream) cross-section. Stratification as a mixing suppressor proved to be significant at the midstream and downstream cross-sections, with the pycnocline damping turbulence, yet showing elevated mixing immediately above and below its interface. The effects of density stratification inhibiting mixing were so pronounced that, despite a funneling effect of the channel increasing velocity and

shear from upriver to downriver cross-sections, mixing did not increase as expected towards the mouth.

key-words: *pycnocline, secondary flow, micro-tidal, salt wedge, funnel-shape, choked lagoon, mixing.*

6.1. Introduction

Turbulence is a key process in coastal hydrodynamics, with ubiquitous importance in exchanging momentum and mixing water properties. Turbulence essentially arises from the existence of velocity shear in the flow (Thorpe, 2007). The main mechanisms producing turbulent mixing are: (1) turbulence generated from bottom boundary layer shear, and (2) turbulence generated from shear between layers in stratified regimes. Vertical shear in the boundary layer reaches maximum values near the bottom and is independent of density stratification, being the main source of turbulence in tide dominated environments (Peters, 1999; Trowbridge et al., 1999; Geyer et al., 2000; Ralston et al., 2010; Collignon and Stacey, 2013).

Shear and mixing can be produced away from the bottom boundary layer, independent of bottom boundary layer processes. Wind can induce shear at the water surface and produce mixing (Sharples et al., 2003; Grifoll et al., 2014). In

stratified estuaries, vertical shear occurs at the pycnocline (Geyer et al., 2008; Ralston et al., 2010; Holleman et al., 2016). In such situations, mixing may or may not occur, depending on whether there is sufficient energy to overcome the vertical stratification.

Salt-wedge estuaries are known for their strong stratification, where fluvial river waters (salinity = 0 g kg^{-1}) flow over coastal waters (salinity > 30 g kg^{-1}) (e.g., Valle-Levinson et al., 2019). Mixing processes in salt-wedge estuaries are still relatively understudied compared to well-mixed or partially stratified estuaries (Schettini et al., 2006; Fiket et al., 2017). Salt wedge estuaries can occur under tidal-forced conditions (e.g., Paiva and Schettini, 2021), where their dynamics are strongly modulated by tidal variations, and also under conditions where the role of tides is negligible, and the dynamics are primarily determined by the fluvial regime (Geyer and MacCready, 2014). Examples of tidally forced salt-wedge estuaries include the Columbia River (U.S.; Kay and Jay, 2003), Fraser River (Canada; MacDonald and Geyer, 2004), Merrimack River (U.S.; Ralston et al., 2010), Snohomish River (U.S.; Wang et al., 2011), and São Francisco River (Brazil; Paiva and Schettini, 2021). Examples of arrested salt wedge estuaries in micro-tidal regions include the Ebre and Rhone Rivers (Spain and France; Ibañez et al., 1997; Ibañez et al., 1999), Neretva River (Croatia; Krvavica et al., 2021), Zrmanja River (Croatia; Fiket et al., 2017), and Araranguá River (Brazil; Valle-Levinson et al., 2019). Micro-tidal salt wedge estuaries are among the least studied estuarine systems and previous research has primarily focused on

circulation dynamics, highlighting the need for more in-depth studies on mixing processes.

The Patos Lagoon is one of the largest chocked coastal lagoons in the world. It is connected to the Atlantic Ocean through the Rio Grande Channel, which, depending on the environmental conditions, can develop a salt-wedge. Its hydrodynamic processes are primarily determined by the relative contribution of wind and river forcing, with astronomical tides of lesser importance (Hartmann and Schettini, 1991; Moller et al., 1996; Fernandes et al., 2005). The Rio Grande Channel features an inverted morphology compared to a traditional drowned valley estuary, with a funnel shape tapering towards the lagoon mouth. This morphology causes an increase in flow velocity toward the region of reduced cross-sectional area and has been indicated in previous studies as a factor that weakens stratification due to increased shear, being also associated with enhanced mixing (Miranda et al., 2002; Yuk and Aoki, 2007).

This study presents the first investigation into the mixing processes in the Rio Grande Channel based on observations, contributing to the understanding of spatial variability in circulation and mixing in microtidal salt-wedge conditions, with particular focus on the effects of channel convergence on flow acceleration and its implications for mixing. In this manuscript we characterize the cross-channel variability of current velocities, salinity, and mixing along a microtidal, salt-wedge estuary. Two primary research questions are posed: (1) How does

channel morphology affect circulation and mixing along the estuary? and (2) What are the primary drivers of mixing along the inlet? To answer these questions, a field experiment was conducted to collect hydrodynamic data, water properties, and turbulence parameters at three cross-sections, during a period of low winds and outflow conditions.

6.2. Study Area

Patos Lagoon, located in southern Brazil, has an area of approximately 10,000 km², with dimensions of about 250 km in length, 40 km in width, and 5 m in depth (Fig. 1c). It has a single connection to the Atlantic Ocean at its southern end, the Rio Grande Inlet, and is considered one of the largest choked coastal lagoons in the world (Kjerfve and Magill, 1989; Miranda et al., 2002). The mouth was modified and extended by the construction of a 4-km-long jetty in 1910, and it currently has a width of approximately 500 m and a depth of 20 m, making it the narrowest cross-section in the entire system (Fig. 1d).

The regional climate is temperate subtropical-humid according to the Köppen-Geiger classification (Cfa), with no dry season throughout the year and well-distributed rainfall (IBGE, 1977). However, there is high interannual variation in the rainfall regime, partially related to ENSO cycles (Grimm et al., 1998).

The lagoon receives inflow from a drainage basin of 200,000 km² that extends into Uruguay and also includes the Mirim Lagoon (Fig. 1b). The river flow follows the pattern for mid-latitudes, with lower values during summer and autumn and peak values in winter and spring (Moller et al., 2001), with an average flow of approximately 2,400 $m^3 s^{-1}$ (Vaz et al., 2011), affected by interannual variations reaching up to 12,000 $m^3 s^{-1}$ (Hartman and Schettini, 1991; Marques et al., 2014).

The local wind regime is controlled by the South Atlantic high-pressure system, disturbed by mid-latitude planetary waves that generate cold fronts. Northeasterly (NE) winds predominate throughout the year, while the significance of southwesterly (SW) winds increases during autumn and winter as frontal systems become more frequent (Stech and Lorenzetti, 1992). The local wind effect is responsible for most of the observed water level variability within the central and inner regions of the lagoon, while remote wind action typically drives the circulation of the inlet zone, controlling exchanges between the estuarine environment and the adjacent continental shelf (Hartmann and Schettini, 1991; Moeller et al., 1996; Moeller et al., 2001; Fernandes et al., 2005).

The local astronomical tides are mixed micro-tidal with a diurnal predominance (Möller et al., 2007), with a mean range of 0.4 m (Moller and Fernandes, 2010). The morphology of the lagoon causes the tidal signal to attenuate as it moves inland (Moller et al., 1996; Fernandes et al., 2004; Castelão

and Moller, 2006), resulting in negligible tidal currents and water level variations in the inner lagoon.

During periods of high river discharge, outflowing currents prevail over the effects of winds (Moller and Castaing, 1999), and according to Silva et al. (2015), periods of outflow dominate over periods of inflow 80% of the time in the lagoon. However, during periods of moderate river discharge, the local wind influences the internal dynamics of the lagoon and its exchange flow (Möller et al., 2001), with high-frequency variability (<15 days) in salinity and currents being dominated by wind forcing (Bitencourt et al., 2020). The Rio Grande Channel can exhibit different salinity distribution patterns depending on wind conditions and river discharge, ranging from well-mixed to highly stratified salt wedge (Hartman and Schettini, 1991; Moller and Castaing, 1999).

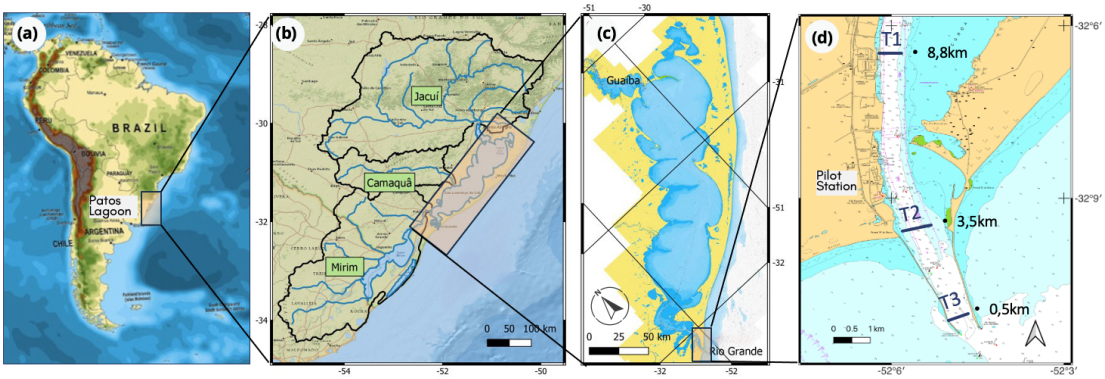


Figure 1: Study area: **(a)** Location of the Patos Lagoon in relation to South America. **(b)** Patos Lagoon and its complex system with the Mirim Lagoon and other rivers and their watersheds. **(c)** Patos Lagoon and the location of the inlet. **(d)** Position of the three cross-sections and the Rio Grande Pilot Station where

wind, current, and tide data were collected. The distance in km shows the spatial variability using T1 as a reference.

6.3. Methods

6.3.1. Data Collection

To capture the spatial variability of current velocities and mixing along the lower stretch of the channel, and to target the predominant condition of seaward currents, the fieldwork was carried out on 19 July 2022 under northeasterly winds. Data collection took place in three cross-sections along the lower stretch of the channel, at 8.8 km, 3.5 km and 0.5 km upstream from the inlet, with 600 m, 1200 m, and 600 m of width, respectively, henceforth, T1, T2, and T3, where 'T' stands for transects (Fig. 1d). Leveraging the secondary importance of the astronomical tides, the data was collected at the three cross-sections consecutively, rather than repeatedly collecting data at each cross-section for a full tidal cycle before moving to the next. This approach permitted the development of a more spatially-oriented assessment as opposed to the conventional temporal approach. The cross-section data was acquired consecutively, with T1 measurements occurring from 13:25 until 14:28, T2 from 14:42 until 15:50 and T3 from 16:00 until 17:03.

Current velocities were recorded with a vessel-mounted Teledyne RDI Workhorse 1200 kHz Acoustic Doppler Current Profiler (ADCP) equipped with bottom-track. The ADCP was setup to record at 0.5 s ping intervals, vertical bin size of 0.25 m, with the first bin at ~1.5 m below the water surface. Positioning was recorded with a GPS receptor attached to the ADCP with estimated error of ~5 m. Salinity and temperature were recorded with a CTD probe by JFE Advantech model Rinko Profiler, and with a Conductivity-temperature Combo Sensor (JAC CT) attached to the micro-structure profiler by Rockland Scientific model Micro-CTD. The latter also is equipped with 2 shear probes, with a sampling rate of 512 Hz, mounted orthogonal to each other which both measures vertical shear of horizontal velocity in two orthogonal directions allowing for the estimation of the turbulence in terms of dissipation (ϵ) of turbulent kinetic energy (TKE).

At each cross-section, the boat made three passes (transects). The first transect was done solely to record currents (ADCP). At the second transect the CTD was lowered and risen sequentially in a yo-yo fashion recording continually during the navigation, allowing for approximately 15 vertical profiles to be obtained per transect, plus the ADCP. The third transect was dedicated to the operation of the Micro-CTD. It was deployed downward with a weighted collar to maintain the descent speed of ~0.8 m/s and an angle of attack of less than 5^{o} (Lueck, 2013; Lueck et al., 2013; Ross et al., 2019a). The boat stopped in at least five sampling stations along the cross-section, where the Micro-CTD was cast at

least five times at each sampling station, with the boat drifting. The data collected at two stations had to be discarded due to the disruption of the measurements by the passage of an external vessel, leaving a total of 83 profiles collected with the MCTD.

Wind, water level, and currents (from a moored ADCP) were obtained from the Rio Grande Pilot Station (Fig. 1d). Wind data is recorded at 5-minute intervals and averaged hourly, collected from a Davis Vantage Pro 2 Meteorological Station. Current and water level are recorded using a Sontek Argonaut-XR 1.5-MHz ADCP, with time averaging every 5 minutes and a vertical bin size of 1.5 m. The ADCP is moored at a depth of approximately 17 m.

River discharge data were estimated from the main tributaries of the lagoon, according to Santa-Rosa and Schettini (2024), using the gauge stations for the following rivers: Jacuí River (station #85900000), Taquari River (station #86720000), Caí River (station #87170000), Sinos River (station #87382000), and Camaquã River (station #87905000). Daily river discharge was obtained from the Hidroweb database of the Brazilian Water Agency (www.snirh.gov.br/hidroweb). Discharge data from the São Gonçalo channel (at the mouth of Mirim Lagoon) was provided by the Mirim Lagoon Agency (Agência da Lagoa Mirim - ALM / UFPel).

6.3.2. Field Data Analysis

6.3.2.1. Vessel-mounted ADCP data

The current velocity data recorded by the ADCP were trimmed within 10% of the bottom to remove erroneous data due to side lobe effects. Velocities greater than 5% of the maximal flow were excluded and any data ensemble with a signal return less than 85% good data were removed (Ross et al., 2019a). A comparison between bottom track velocities measured by the instrument and instrument velocities by the GPS data was made to correct ADCP data compass for directional bias (Joyce,1989; Valle-Levinson et al. 2015). The resulting velocity time series for East-West (u) and North-South (v) components were rotated using principal component analysis (Thomson and Emery, 2014) to align with the primary direction of the flow.

6.3.2.2. MCTD data

The rate of dissipation (ϵ) of Turbulent Kinetic Energy (TKE) is derived from the measurements of velocity shear recorded by the shear probes on the MCTD (Lueck et al., 2020). Assuming that the turbulence is isotropic, the TKE dissipation rate is given by Eq. (1)

$$\epsilon = \frac{15}{2}\nu\overline{\left(\frac{\partial u}{\partial z}\right)^2} = \frac{15}{2}\nu\int_0^\infty \Psi(k)dk\ , \quad (1)$$

where ν is the kinematic molecular viscosity (10^{-6} m s^{-2}), Ψ is the velocity shear spectrum, and *k* is the wave number (m^{-1}) (Lueck, 2013). The ϵ is expressed as the rate of dissipation of TKE per unity mass (W kg^{-1}, or equally, m^2 s^{-3} from Eq. 1) (Thorpe, 2007).

The estimates of ϵ from each of the two shear probes affixed to the instrument were compared at each depth and if the value differed more than a factor of 2, the larger estimate was removed (Stips, 2005). Vertical profiles with angle of attack greater than 5º were also removed, which represented less than 1% of the data. Correction for profiler vibration was made using the method of Goodman et al. (2006). Individual wave number spectra for each component were calculated using a Fast Fourier Transform (FFT) with a length of 0.5 m and a time span of 2 s for each estimate of the rate of dissipation (Fig. 2b). The calculated ϵ data were then interpolated onto a uniform vertical grid. This procedure resulted in at least ten vertical profiles (2 shear probes x 5 casts) of ϵ for each sampling station. The values of each vertical level were then resampled 6,000 times by the bootstrapping method (Efron and Gong, 1983) to provide statistically significant estimates of ϵ (Fig. 2a), which were then used to quantify the vertical eddy viscosity (A_z).

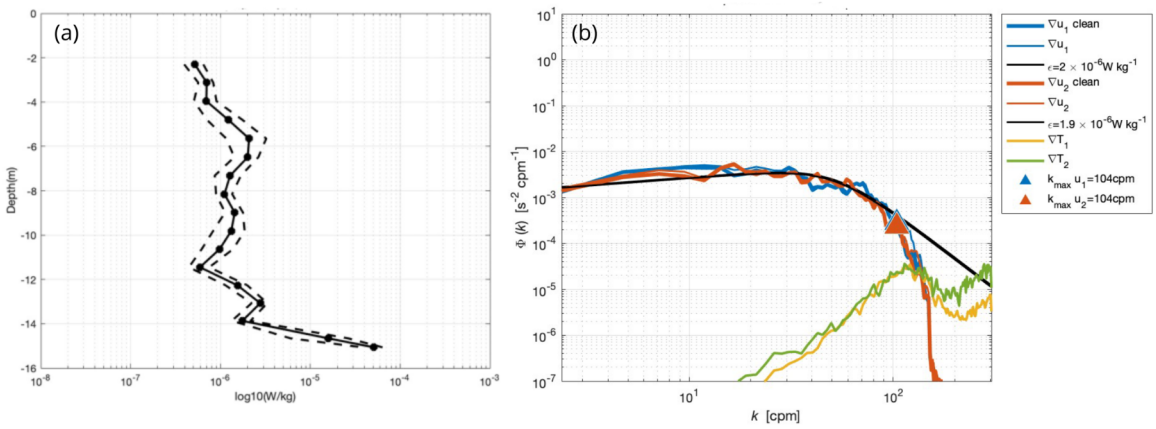


Figure 2: Example output from one station. **(a)** Example profile of ϵ (black line) after bootstrapping the ϵ estimates from the 5 casts from both shear probes (10 profiles total). The dashed lines represent a 95% confidence interval. **(b)** Example wave number spectra with noise removed showing the shear estimates from each probe (thick blue and red lines), the theoretical Nasmyth spectra (black line) the limits of integration in wave number space for each shear probe to estimate ϵ (blue and red triangles), and the vertical temperature gradient (yellow and green lines).

6.3.2.3. Turbulence Parameters and Vertical Mixing

The vertical eddy viscosity (A_Z) and the buoyancy Reynolds number (Re_b) were calculated as proxies for mixing. The following steps were executed to obtain these parameters. First, the along-channel and cross-channel velocities

from each transect were used to calculate the squared vertical shear (S^2) as shown in Eq. (2):

$$S^2 = \left(\frac{\partial u}{\partial z}\right)^2 + \left(\frac{\partial v}{\partial z}\right)^2, \quad (2)$$

where u and v are the longitudinal and lateral flow components respectively, and the coordinate z is positive upward. The stratification was estimated using the buoyancy frequency (N^2), which is quantified by Eq. (3):

$$N^2 = -\frac{g}{\rho_o}\frac{\partial \rho}{\partial z}, \quad (3)$$

where g is the gravitational acceleration, and ρ_o is a reference of density. The gradient Richardson number is the ratio of buoyancy frequency and squared vertical shear, $R_i = N^2/S^2$, and is the main stability parameter of a stratified fluid and a dimensionless number for parameterization of turbulent flows, that quantifies the importance of stratification on mixing (Monismith, 2010).

From R_i, the flux Richardson number, a scale for mixing efficiency (Holleman et al., 2016; Greg et al., 2018; Ross et al., 2019a), can be obtained by Eq. (4) (Venayagamoorthy & Koseff, 2016):

$$R_f = 0.25\,(1 - e^{-7R_i}). \quad (4)$$

In stably stratified flow, R_f is the fraction of total TKE production that is lost to buoyancy, increasing the potential energy of water column (Kay and Jay, 2003). A mixing coefficient Γ_m can be denoted from the mixing efficiency as shown in Eq. (5):

$$\Gamma_m = \frac{R_f}{1-R_f} \ . \tag{5}$$

And, finally, as a proxy of mixing the vertical eddy viscosity can be obtained by Eq. (6) (Kay and Jay, 2003; Huguenard et al., 2015; Ross et al., 2019a):

$$A_z = \Gamma_m \frac{\epsilon}{S^2} \ . \tag{6}$$

The role of the density stratification on the turbulence can also be scaled by Eq. (7):

$$Re_b = \left(\frac{L_o}{L_k}\right)^{4/3} = \frac{\epsilon}{\nu N^2} \ , \tag{7}$$

where the ratio L_o/L_k is the ratio between the Ozmidov scale (largest scale turbulence) over Kolmogorov scale (smaller scale turbulence). The Re_b is also commonly, and synonymously, referred to as the turbulent activity parameter, activity number, strain-based Froude number, Gibson number, or buoyancy Reynolds number (Shih et al., 2005; Monismith, 2010; Holleman et al., 2016).

When Re_b > 200 small-scale turbulence is not affected by stratification. If 15 < Re_b < 200 the effect of stratification extends to smaller and smaller scales and lastly if Re_b < 15 stratification “kills turbulence” (Gargett et al., 1984; Ivey et al., 2008; Monismith et al., 2010).

6.4. Results

6.4.1. Ambient Conditions

The estimated discharge of the main tributaries of the Patos Lagoon, along with wind speed and direction, water level, and current velocities, measured at the Pilots Station over a one-week interval are presented in Figure 3. On the day of the field campaign (July 19th, 2022), the estimated total discharge was approximately 6890 $m^3\ s^{-1}$ (Fig. 3a), significantly higher than the estimated average flow for the same month, which was 3707 $m^3\ s^{-1}$. The wind was relatively weak compared to the preceding days (Fig. 3b), blowing from SSE to SE and ranging between 1.6 and 5 $m\ s^{-1}$. Water level variability during the survey was minimal, fluctuating by about 0.20 m (Fig. 3c). The current flowed seawards throughout the entire water column during the fieldwork (Fig. 3d), with velocities ranging from 0.5 to 1.0 $m\ s^{-1}$, without changing direction. There was only a slight decrease in magnitude compared to the previous day, likely due to the reduction

in wind velocity. Nevertheless, this condition represented a significant variation compared to the other days in the interval, as observed in the full plot.

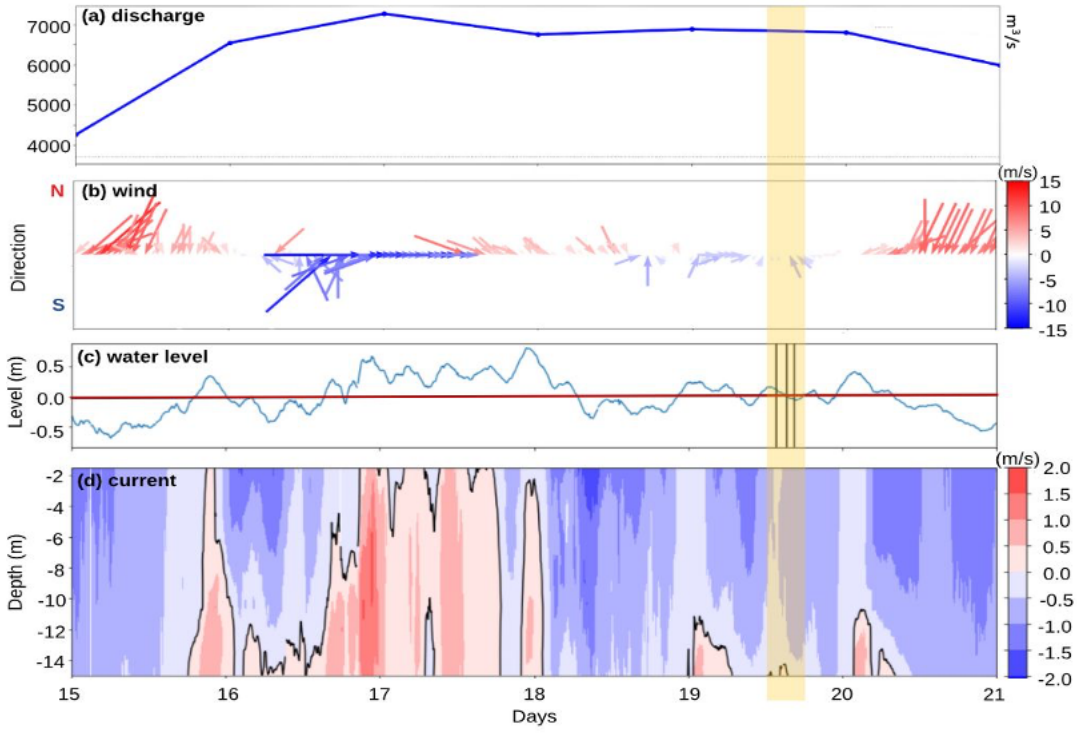


Figure 3: Ambient conditions over a one-week interval, with the vertical yellow bar representing the field period. **(a)** Estimated discharge of the main tributaries of Patos Lagoon (blue line representing the total main tributaries discharge and black dotted line at the bottom of the diagram representing the average estimated discharge for July 2022); **(b)** vector plot of wind, where blue represents northwards winds and red represents southwards winds; **(c)** water level, where the three vertical lines indicate the moments when the cross-sections were conducted; **(d)** Hovmöller diagram of current velocity, where red indicates inflow and blue indicates outflow.

6.4.2. Salinity, temperature and density

The cross-sectional distributions of salinity, temperature, and density, facing landward, are presented in Figure 4. In the upstream cross-section (T1), salinity was nearly vertically homogeneous (Fig. 4a.1), with some small lateral variability, with a maximum of 1.8 g kg^{-1} and a minimum of 1.2 g kg^{-1} in the shoal (right side). In the middle cross-section (T2), there is an increase of the salinity at the bottom with a sharp halocline, ranging from 1.4 to 10.9 g kg^{-1} (Fig. 4a.2). The stratification is more pronounced in the deeper section of the channel, indicating that this is the tip of the salt-wedge. In the downstream cross-section (T3), the stratification is even higher, with salinity varying from 1.4 to 27.5 g kg^{-1} (Fig. 4a.3).

The temperature in all cross-sections ranged between 12.5 and 13.5 °C. The temperature at cross-section T1 exhibits minimal variation across the transect (Fig. 4b.1), with a noticeable increase in temperature on the shoal of the right side of the channel. In T2, a lateral temperature gradient is observed, with warmer water on the right side of the channel (13.1°C) compared to the left side (12.8°C) (Fig. 4b.2). A vertical temperature gradient also occurs in the middle of the channel. In T3 the temperature displays vertical homogeneity on the left side of the cross-section. On the right side, there is a gradient following the salinity pattern (Fig. 4a.3). The cross-sectional density distributions (Fig. 4c) follow mainly the salinity patterns in T2 and T3, while in T1 it also follows the temperature distribution.

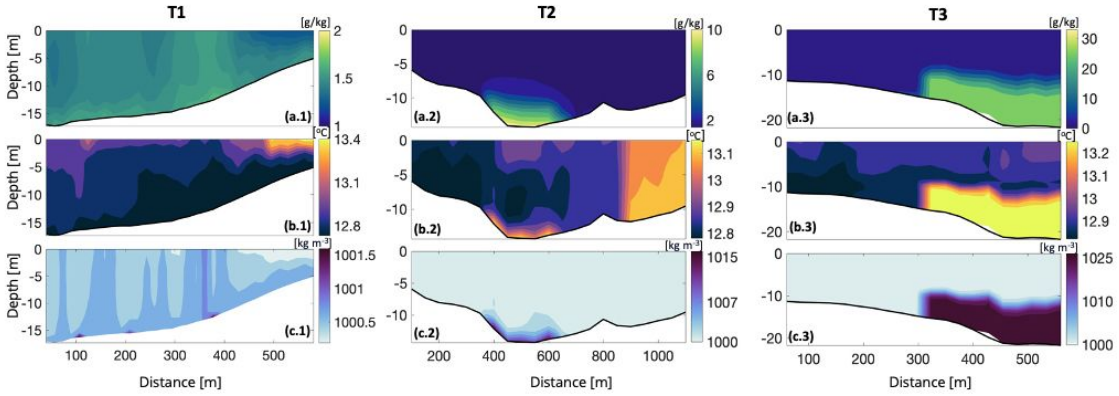


Figure 4: Cross-sectional distributions of **(a)** salinity; **(b)** temperature; and **(c)** density, looking landward in the cross-sections T1 (left), T2 (center), and T3 (right). The color bar scales are different for each transect to magnify the variability.

6.4.3. Along-channel and cross-channel velocity

The along-channel velocities in all three cross-sections were directed seawards (Fig. 5a). There is a lateral gradient in along-channel velocity at T1 (Fig. 5a.1), with higher velocities of –0.9 m s^{-1} on the deeper and left side of the channel, decreasing to smaller speeds approaching zero on the shallower, right side. In the cross-section T2, a lateral gradient in velocity is also observed, with higher velocities near the surface in the channel thalweg and lower velocities toward the banks (Fig. 5a.2). In the middle of the cross-section there is a sharp decrease in the velocity intensity, decreasing to almost zero at the bottom, where the tip of salt wedge occurs. In cross-section T3, there is no significant lateral gradient compared to the previous transects. However, there is a stronger vertical

gradient in the along-channel velocity, creating a clear separation between the upper and lower water columns across the transect. The velocity shows a pronounced outflow above the pycnocline (–2 m s^{-1}), while below the pycnocline, the outflow is much weaker (< –0.5 m s^{-1}). The stronger vertical gradient in the along-channel velocity occurs between 10 and 15m depth (Fig. 5a.3), coinciding with the depths of the pycnocline (Fig. 4c.3).

The cross-channel velocities in cross-section T1 exhibit a three-layer flow, with eastward flow at the core of the section, and westwards flow in a thin layer at the surface and at the bottom (Fig. 5b.1). Cross-section T2, presents two-layer flow, with the top layer flowing westwards, and the bottom layer flowing eastwards (Fig. 5b.2). Cross-section T3 also displays a two-layer flow, similar to T2, but with stronger velocities and a sharper vertical gradient (Fig. 5c.3).

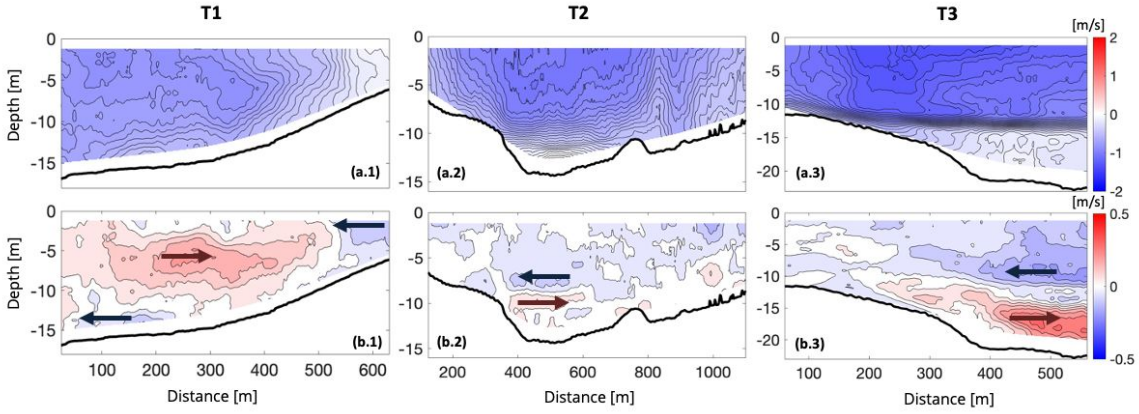


Figure 5: (a) Along-channel and **(b)** cross-channel velocities measured by vessel-mounted ADCP at the three cross-sections. Note that transects share the same color scale. In (a), positive values represent inward flow, while negative

values indicate outward flow. In (b), positive values correspond to westward flow (left to right), and negative values indicate eastward flow (right to left).

6.4.4. Mixing Parameters

The cross-channel variability of squared vertical shear (S^2), buoyancy frequency (N^2), Richardson number (Ri), turbulent kinetic energy dissipation (ϵ), vertical eddy viscosity (A_z), and buoyancy Reynolds number (Re_b) will be presented for each cross-section.

6.4.4.1. Cross-section T1 – Upstream

At the upstream cross-section (T1; Fig. 6a), higher shear values (~$10^{-1.5}$ s^{-2}) occur in regions where there is a convergence of flow as depicted in the cross-channel velocities (Fig. 5b.1, ~500 m), which coincide with the region where the isolines of velocity converge (Fig. 5a.1). Higher values of buoyancy frequency (~$10^{-1.7}$ s^{-2}) are located on the right side of the channel (Fig. 6b), where zones of lower salinity and higher temperature appear on the transect (Figs. 4a.1 and b.1). This is also the area where Richardson numbers are higher than 1 (Fig. 6c). TKE dissipation rates vary laterally in the cross-section and are lower (~10^{-7} W kg^{-1}) at the center of the thalweg, with higher values (~10^{-4} W kg^{-1}) near bottom (Fig. 6d). The vertical eddy viscosity of T1 (Fig. 6e) is maximum near bottom as well (~10^{-}

^{2} m^{2} s^{-1}), and minimum vertical eddy viscosity values ~10^{-6} m^{2} s^{-1} were found in the same area of the minimum ϵ. The buoyancy Reynold number shows two distinct zones near the surface (between 200 m and 300 m and after 500 m) with values lower than 200, which are represented by the black line on Figure 6f. This central minimum Re_b area also coincides with the zone of lower A_z values.

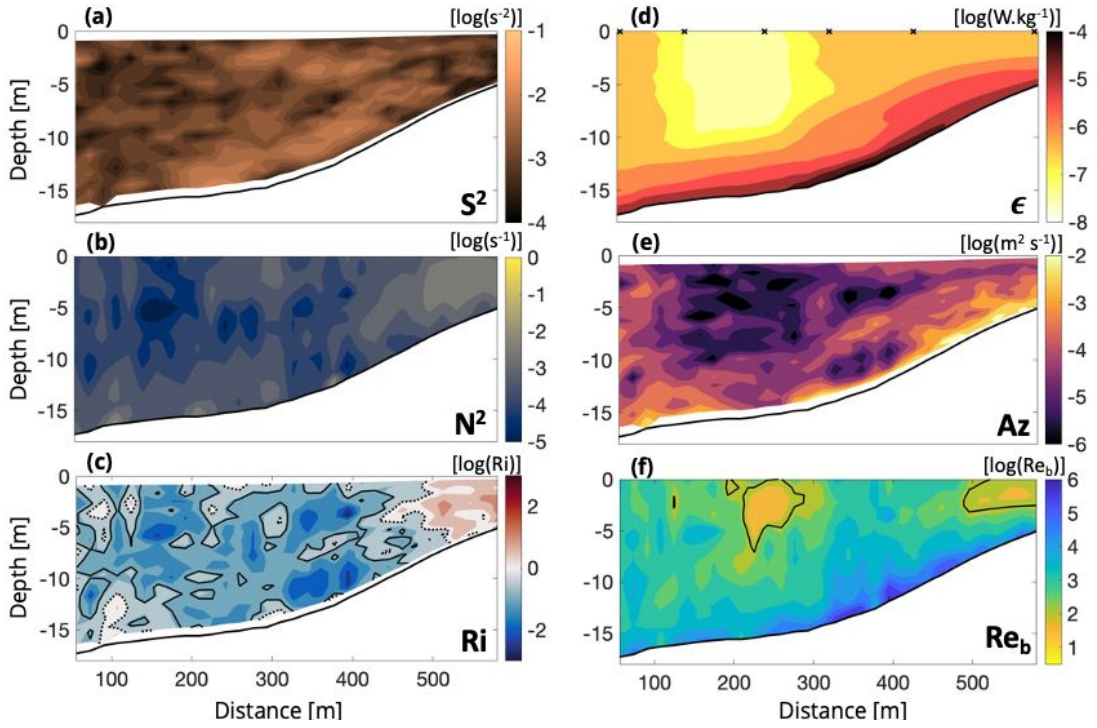


Figure 6: Calculated parameters for T1: **(a)** squared vertical shear (S^2); **(b)** buoyancy frequency (N^2); **(c)** gradient Richardson number (R_i), with the solid lines representing the values of R_i = 0.25 and the dotted lines representing R_i = 1; **(d)** TKE dissipation (ϵ). The black x's denote the MCTD stations throughout the distance (m); **(e)** vertical eddy viscosity (A_z); and **(f)** buoyancy Reynold number (Re_b), with the solid lines representing the values of Re_b = 200. All subplots show

log10 values and the x-axis depicts the distance in meters from the beginning of the transect and the y-axis depicts depth in meters.

6.4.4.2. Cross-section T2 – Mid-channel

Shear at T2 is highest (~10^{-1} s^{-2}) near bottom in the thalweg (Fig. 7a), which corresponds to the bottom circulation cell in the cross-channel velocity (Fig. 5b.2). This area with higher shear values also coincides with the convergence zone of the isolines in the along channel velocities (Fig. 5a.2), and with the region of saltier and more dense water (Figs. 4a.2 and c.2). The highest values of buoyancy frequency (~10^{-1} s^{-2}) are also in the thalweg (Fig. 7b) near bottom. The Richardson number is highest in the deeper part of the cross-section (Fig. 7c; ~500 m), and TKE dissipation rates are highest near bottom (10^{-4} W kg^{-1}, Fig. 7d), decreasing toward the surface (< 10^{-7} W kg^{-1}). Vertical eddy viscosity is maximum (~10^{-2} m^2 s^{-1}) at the bottom as well (Fig. 7e), with values as high as ~10^{-3} m^2 s^{-1} near the interface of the pycnocline, and lower values of ~10^{-6} m^2 s^{-1} just above and below the interface, which can be explained by suppression of mixing by stratification. Previous studies (Turner, 1973; Garget et al., 1984; Ivey et al., 2008; Monismith, 2010; Simpson et al., 2012; Geyer and MacCready, 2014; Huguenard et al. 2015) observed this effect of the vertical stratification suppressing mixing and it is also evident in the last subplot (Fig. 7f), with the solid black line representing Re_b = 200, showing two distinct zones with small-scale turbulence being affected by stratification.

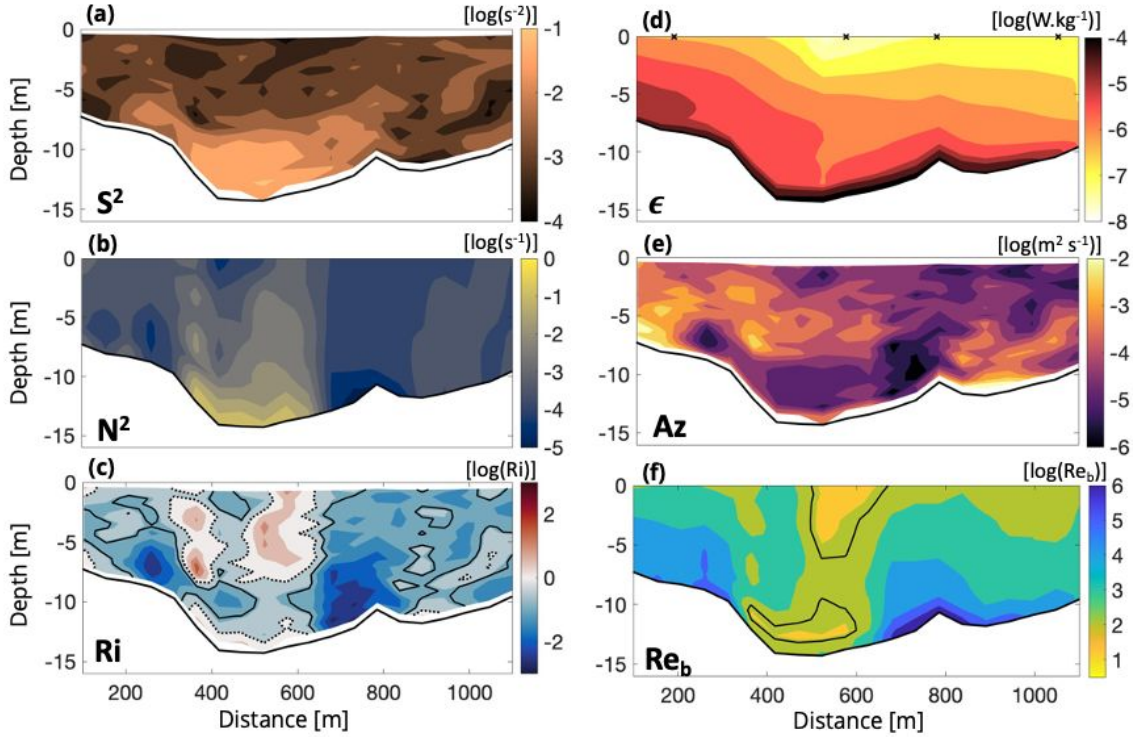


Figure 7: Calculated parameters for T2: **(a)** squared vertical shear (S^2); **(b)** buoyancy frequency (N^2); **(c)** gradient Richardson number (R_i), with the solid lines representing the values of R_i = 0,25 and the dotted lines representing R_i = 1; **(d)** TKE dissipation (ϵ). The black x's denote the MCTD stations throughout the distance (m); **(e)** vertical eddy viscosity (A_z); and **(f)** buoyancy Reynold number (Re_b), with the solid lines representing the values of Re_b = 200. All subplots show log [10] values and x-axis depicts the distance in meters from the beginning of the transect and the y-axis depicts depth in meters.

6.4.4.3. Cross-section T3 - Downstream

The pycnocline is the remarkable feature at T3 (Fig. 4c), with correspondent features in all parameters. In the shear distribution (Fig. 8a) there is a horizontal band at –10 m depth, that coincides with highest values of buoyancy frequency (Fig. 8b). On the Richardson number distribution is possible to observe a similar band (Fig. 8c) with $R_i > 1$. Larger values of TKE dissipation rate are found above and below the pycnocline (Fig. 8d), with some peaks of 10^{-4} W kg^{-1}. The vertical eddy viscosity (Fig. 8e) has a maximum value of ~10^{-2} m^2 s^{-1}, and the highest values are just above and below the pycnocline, where A_z is minimum (~10^{-6} m^2 s^{-1}). On the buoyancy Reynold number diagram, the region of $Re_b < 200$ is circled by black solid lines (Fig. 8f). Within this region, a dotted line surrounds $Re_b < 15$, over the same region where A_z is minimum, which indicates that turbulence is being completely suppressed by stratification (Gargett et al., 1984; Ivey et al., 2008; Monismith, 2010).

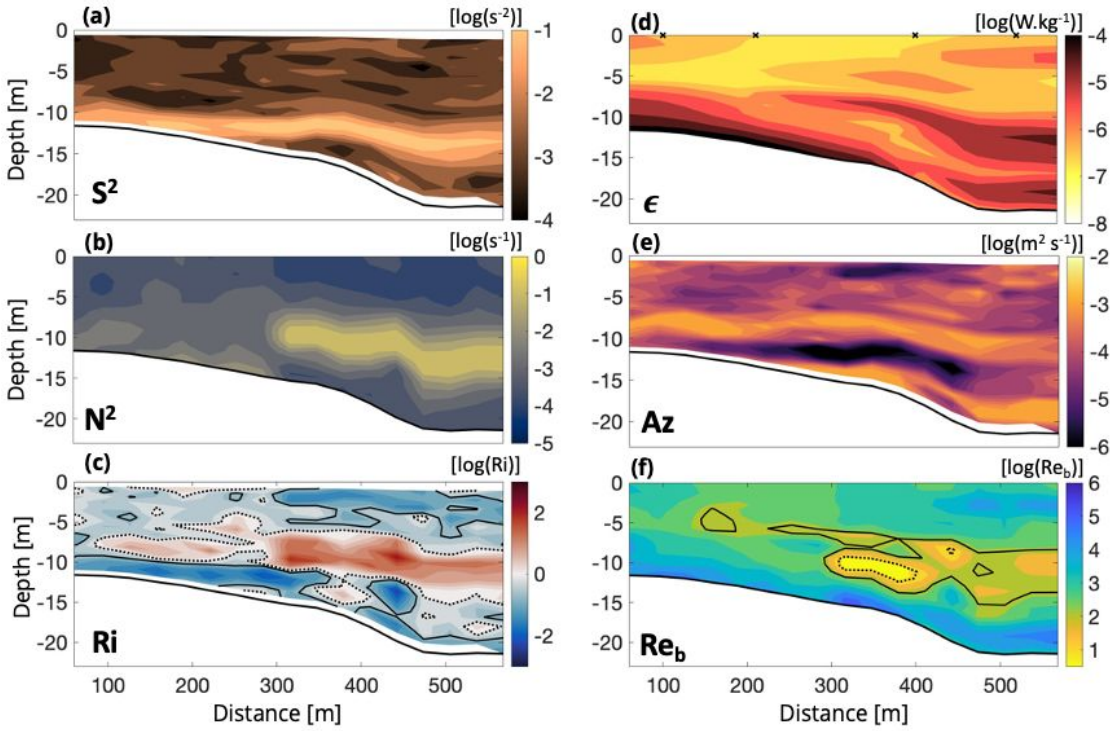


Figure 8: Calculated parameters for Transect 3: **(a)** squared vertical shear (S^2); **(b)** buoyancy frequency (N^2); **(c)** gradient Richardson number (R_i), with the solid lines representing the values of R_i = 0.25 and the dotted lines representing R_i = 1; **(d)** TKE dissipation (ϵ). The black x's denote the MCTD stations throughout the distance (m); **(e)** vertical eddy viscosity (A_z); and **(f)** buoyancy Reynold number (Re_b) with the solid lines representing the values of Re_b = 200 and dotted lines representing values = 15. All subplots show log [10] values and x-axis depict the distance in meters from the beginning of the transect and the y-axis depicts depth in meters.

6.5. Discussion

The field survey was conducted after the passage of a cold front on days 16-17 of July 2022. The cold front passage produced intense winds of 10-15 m s^{-1} veering from S-SW, producing a period of outflow in the lagoon. After the cold front passage, the wind rotated to the NE, and the current regime shifted to inflow for the next few days. This exemplifies the typical exchange regime between the lagoon and the ocean, driven primarily by the wind regime. This hydrodynamic behavior, where meteorological conditions dominate over the influence of the astronomical tide, can also be observed in the spectrum of the water level and longitudinal current velocity, for July of 2022, which shows a concentration of spectral density in the lower frequencies, or periods higher than 25 hours (Fig. 9). These frequencies are related to the time scales associated with frontal system passages, ranging from 5 to 16 days (Moeller et al., 2001; Santa-Rosa and Schettini, 2024).

The impact of the wind on circulation during periods of moderate to low river inflow, can be described as follows: southerly winds, due to the passage of cold fronts, cause an in-lagoon flow, leading to salinity intrusion. After the cold front, the wind rotates to northeasterly, favoring an out-lagoon flow, promoting saltwater transport out of the channel (Bitencourt et al., 2020). Thus, beyond being the primary driver of water level variance and current velocities, wind plays a fundamental role in salinity transport into or out of the channel. Given the limited tidal influence on circulation, the salinity distribution also lacks tidal variability,

instead showing a direct correlation with wind forcing (Garcia, 1997; Fernandes et al., 2005).

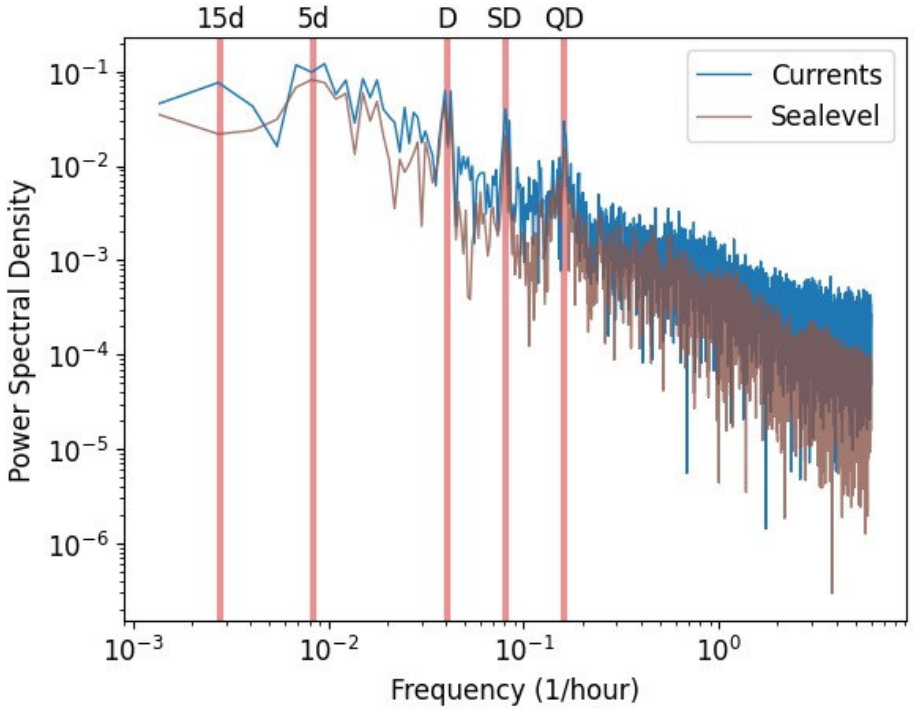


Figure 9: Spectrogram of the sea level and current velocity (sampling interval = 5 minutes) during the entire month of July 2022. The vertical red lines serve as references for various tidal cycles, including QD (quarter-diurnal), SD (semi-diurnal), and D (diurnal), as well as 3-day and 15-day cycles.

6.5.1. Circulation, Density, and Mixing Variability along the Inlet

6.5.1.1. Upstream Transect - T1

Circulation at T1 is a result of the interaction of barotropic and baroclinic forces interacting with the channel morphology. To understand the along-estuary

and transverse circulation, it is essential to revisit the passage of the cold front on the previous days (days 16-17) as depicted in Figure 3a and note the prevailing winds from the west and south. As evidenced by previous measurements and numerical experiments in Patos Lagoon (Moeller et al., 1996; Fernandes et al., 2005), SW winds tend to pile up water in the northern region of the lagoon, establishing an along-channel barotropic pressure gradient. Subsequently, as the wind velocity diminishes, the water level gradually tends to reach equilibrium through a seaward current.

Furthermore, the channel morphology induces salinity, temperature, and density gradients from the shoal at the east bank towards the center of the channel, resulting directly in lateral circulation. Fernandes et al. (2005) also observed this secondary flow pattern in their simulations and attributed it to the interaction of barotropic and baroclinic pressure gradients. The simulation observed lateral barotropic pressure gradients developing after strong southward wind which caused water to accumulate on the east bank, leading to an elevated lateral barotropic pressure gradient. Baroclinicity arises from the lateral density gradient generated by regions of sharp bathymetric changes.

In our study, the interaction between the barotropic and baroclinic pressure gradients driving the lateral circulation is illustrated in Figure 5b.1. At the surface, water tends to flow westward due to the cross-channel barotropic pressure gradient, while the water column below flows eastward as a result of the baroclinic pressure gradient. Although we lack water level measurements over the transect to assess the barotropic gradient, we can observe fresher water being trapped

on the shoal at the east side of the channel (right side of Fig. 4a.1), where warmer water is also observed (Fig. 4b.1). Solar radiation is primarily responsible for heating the water surface, being more effective in shallower areas, such as the shoal at the east side of the channel. The warmer and fresher water results in lower density (Fig. 4c.1). This three-layer lateral circulation pattern usually arises by the baroclinic pressure gradient counterbalancing the acceleration effect due to curvature (Nidzieko et al., 2009; Ross et al., 2019b). The comparison of the order of magnitude of both is described in section 5.2.4.

The squared vertical shear is highest at the interface region between cells of opposite directions of cross-channel velocity. The area with the highest buoyancy frequency values coincides with the region of highest density gradient, which is also where Richardson numbers exceed 1. This indicates that despite high shear, buoyancy forces are sufficiently strong to suppress turbulence and mixing of the fresh and saltwater layers. It is observed that the highest values of turbulent kinetic energy (TKE) dissipation occur within the bottom boundary layer, with a region of low ϵ notably located along the main axis of the channel. Vertical eddy viscosity exhibits a similar behavior to ϵ, with low values in the thalweg and higher values concentrated in the bottom boundary layer. The buoyancy Reynolds number shows two regions enclosed by a continuous black line with Re_b = 200. These regions with Re_b values lower than 200 (but still above the threshold of 15) represent areas where small-scale turbulence is already influenced by stratification, which coincides with where there is high buoyancy frequency.

As noted by Geyer (1993) and Chant (2010), the effects of stratification have a dual impact on enhancing secondary circulation. First, it amplifies the shear in the stream-wise flow, driving the secondary flow. It also inhibits mixing, thus requiring stronger lateral shears (i.e., secondary flows) to counterbalance the shear force. Consequently, despite higher shear areas in the midwater column, mixing primarily occurs in the bottom boundary layer due to its interaction with the bed.

6.5.1.2. Midstream Transect – T2

At T2, we observed the conditions at the tip of the salt wedge, where there is a slowing of the flow in the lower layer along the thalweg. There is also a lateral gradient in along channel velocity that results from differential advection, one of the major mechanisms driving secondary flow (Chant, 2010). The vertical gradient in along-channel velocity creates a convergence of the isolines of the velocities, which explains the high shear values. Vertically sheared flow with curvature will develop a secondary flow with the lower-layer flow directed toward the inside of the bend and the upper-layer flow directed away from the bend (Chant, 2002), which is observed in Fig. 5b.2. Here the upper layer is flowing towards the west, over a deeper layer in opposite direction. It's noteworthy that despite typically representing less than 10% of the strength of along-channel flows, secondary flows remain the dominant process driving lateral mixing in estuaries, with differential advection predominating in many systems, except

those in the vicinity of channel bends, where flow curvature takes precedence (Chant, 2010) as will be verified at T2 in the subsequent section 6.5.2.4.

The highest buoyancy frequency values are concentrated in the thalweg, where the density gradient is most pronounced, which is reflected in the Richardson number and TKE distributions. However, vertical eddy viscosity has maximum values at the bottom at the flanks, with suppression occurring at the bottom of the deeper part of the channel. The A_z results (Fig. 7e) are more coherent when compared with the buoyancy Reynolds number distribution (Fig. 7f), where the stratification affecting the small-scale turbulence is highlighted by the areas surrounded by higher Re_b. This explains the suppression of mixing at the bottom of the thalweg, that is also the same region of the highest buoyancy frequency values. Hence, some mixing might arise from the interface of the pycnocline, but primarily occurs in the bottom boundary layer. There are exceptions in areas where mixing is suppressed by stratification, mainly driven by the secondary flow.

6.5.1.3. Downstream Transect – T3

The results from the cross-section T3 captured a highly stratified condition, with a sharp pycnocline which affected all assessed parameters. The stratification affects the along-channel flow, with a steep reduction in the speed between the upper and lower layers. The cross-channel velocity shows the same curvature effect observed in T2, with the lower-layer flow directed toward the inside of the

bend (east) and the upper-layer flow directed away from the bend (west). This two-layer vertical profile of the secondary flow was previously observed by Fernandes et al. (2005). Their modeling results revealed that the funneling effect of the estuarine access channel amplifies the influence of river flow leading to the eventual separation of the flow into a two-layered vertical profile.

The elevated squared vertical shear values at T3 (Fig. 8a) are concentrated over the same zone of separation between fast and slow along-channel flow, also consistent with the highest values of buoyancy frequency, which peaks at the pycnocline (Fig. 8b). The spatial distribution of the Richardson number indicates conditions favorable for mixing above and below the pycnocline ($R_i < 0.25$), and the TKE dissipation rates and A_z are smallest in the pycnocline, highlighting the separation between the layers. The buoyancy Reynolds number shows a wide area of small-scale turbulence being affected by stratification (continuous black line, with $Re_b = 200$), and additionally highlights the brighter area, surrounded by the dotted black line ($Re_b = 15$). As reported by previous studies (Garget et al., 1984; Ivey et al., 2008; Monismith, 2010), stratification 'kills' mixing.

Mixing can be generated by the shear in the pycnocline (Peters, 1997; Ralston et al., 2010; Collignon and Stacey, 2013; Huguenard et al., 2015; Ross et al., 2019a), however, the effect of the stratification can also suppress mixing (Turner, 1973; Garget et al., 1984; Ivey et al., 2008; Monismith, 2010; Simpson et al., 2012; Geyer and MacCready, 2014). Results at T3 indicate that despite the high values of squared vertical shear at the pycnocline, stratification plays a major

role, acting as a physical barrier. Figure 10 illustrates this scenario, showing a vertical profile at T3 of along-channel velocity and density, and also a comparison profile of buoyancy frequency, squared vertical shear and vertical eddy viscosity. The area of higher buoyancy frequency (the pycnocline region) coincides with higher values of shear, between 11-12 m depth, and minimum A_z values ~10^{-6} m^2 s^{-1}. In contrast, maximum A_z values (> 10^{-2} m^2 s^{-1}) are found immediately above and below this layer (at ~ 8 m and 14 m depth).

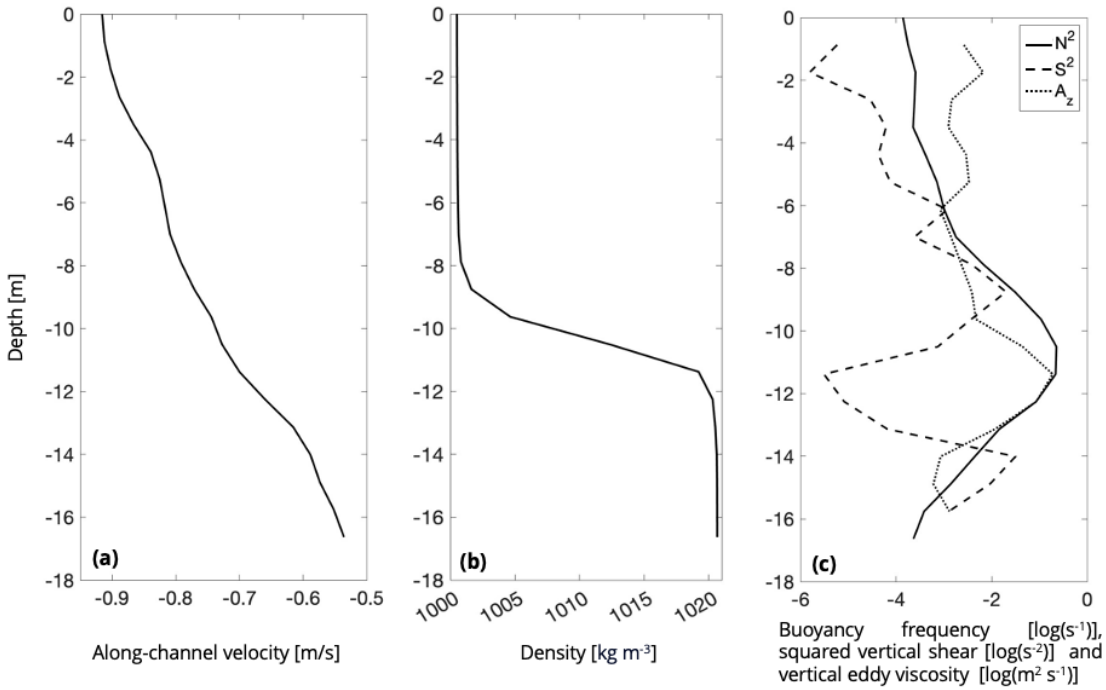


Figure 10: Comparison between mixing parameters of one vertical profile of cross-section T3. (a) Along-channel velocity; (b) density; (c) solid line representing buoyance frequency (N^2); dotted line representing squared vertical shear (S^2) and dashed line representing vertical eddy viscosity (A_z). The x-axis in subplot (c) show log [10] values of the parameters and the y-axis depicts depth in meters.

Therefore, the predominant mechanisms for mixing at T3 are the turbulence generated by the bottom boundary layer and the internal shear layer instabilities at the pycnocline interface. Nevertheless, it is important to note that while vertical shears in velocity promote mixing, on the other hand, vertical density stratification inhibits it (Turner, 1973; Huguenard et al., 2015).

6.5.1.4. Detailing and comparing lateral circulation at the 3 cross sections

Although secondary flows are much weaker than along-channel flows, they can substantially influence estuarine dynamics when interacting with axial gradients in salt and momentum (Chant, 2002). Differential advection of salt in channels with varying cross-sectional depth generates a lateral salinity gradient that drives lateral baroclinic flows across the channel. Additionally, centrifugal acceleration in a curved channel induces a distinct pattern of secondary circulation (Lacy and Monismith, 2001). To better understand the lateral circulation patterns at the three cross-sections, the orders of magnitude of the baroclinic pressure gradient and the curvature-induced acceleration were estimated.

The baroclinic pressure gradient was quantified as $g/\rho_0\,(\partial\rho/\partial y)\,z$ = $g/\rho_0(\Delta\rho/\Delta y)\,z$, where g = 9.81 m s^{-2}, ρ_0 = 1000 kg m^{-3} for the three cross-sections, while $\Delta\rho$, Δy and z varied for each cross-section according to the values shown in Table 1. The acceleration due to curvature was calculated as u^2/R, where u is the mean along channel velocity of –0.62, –0.72 and –0.89 m s^{-}

^{1} at T1, T2 and T3 respectively and R ~11500 m is the radius of curvature of the headland measured from the location of largest along-channel velocities (Ross et al., 2019b).

According to the results presented in Table 1, secondary flow is affected differently by the baroclinic pressure gradient and the curvature-induced acceleration at each cross-section. At T1, the two forces are nearly balanced, as they are of the same order of magnitude. At T2, curvature-induced acceleration is one order of magnitude greater than the baroclinic pressure gradient, making it the dominant driver of lateral circulation. Finally, at T3, a significant lateral baroclinic pressure gradient arises due to variations in stratification: the left side of the cross-section exhibits lower stratification, while the right side is more stratified. This results in a baroclinic pressure gradient that is two orders of magnitude greater than the curvature-induced acceleration.

Table 1: Order of magnitude comparison between lateral baroclinic pressure gradient, and acceleration due to curvature for the cross-sections.

	T1	T2	T3
$\Delta\rho$ (lateral density gradient) [kg m^{-3}]	0.08	0.058	9.06
Δy (cross-section width) [m]	600	1200	600
z (average depth) [m]	12.6	9.3	16
Baroclinic pressure gradient [m s^{-2}]	1.6 x 10^{-5}	4.4 x 10^{-6}	2.4 x 10^{-3}
Acceleration due to curvature [m s^{-2}]	3.3 x 10^{-5}	4.5 x 10^{-5}	6.9 x 10^{-5}

6.5.2. Consequence of convergence on flow velocity and mixing

The Venturi effect results from the application of Bernoulli's principle to a confined flow, wherein fluid velocity or flow rate increases due to a decrease in flow area, with flow rate and cross-sectional flow area being inversely proportional (Venturi, 1799). This phenomenon is currently applied in various fields, including medicine, the automotive industry, and wind engineering/urban aerodynamics (Blocken et al., 2008).

A study by Yuk & Aoki (2007), found that topographic changes, such as the narrowing of an inlet of a semi-enclosed bay, can lead to the intensification of currents, which enhances vertical mixing. The enhanced current velocities were not only due to the alterations in topography, but also from the subsequent changes in bathymetry resulting from the construction of the jetties. Consequently, this effect was expected to also affect the flow at the funnel-shaped breakwater at Patos Lagoon inlet.

Such an increase in along-channel velocity is evident when comparing the three cross-sections (Table 2). Along-channel mean velocities increases towards the cross-section T3, where the estuary experiences a reduction in cross-sectional area. The along-channel maximum velocities for each transect, observed near the surface and in the center of the cross-sections also increases toward T3, with velocities of –0.87, –1.06, and –1.34 m s^{-1}, respectively. The squared vertical shear increases in similar fashion, from T1 to T3. However, the vertical eddy viscosity does not follow this pattern. There is an increase in the

cross-section mean eddy viscosity from T1 to T2, and a decrease from T2 to T3. Although there is an apparent correlation between increased velocities and enhanced mixing, stratification can be strong enough to inhibit mixing in T3, despite higher velocities and stronger shear relative to the other sections. This indicates that variations in flow velocity and shear can affect mixing less than the effects of strong stratification at the pycnocline.

Table 2: Summary of results of along-channel velocity, velocity shear, eddy viscosity (A_Z), for the cross-sections.

	T1	T2	T3
Mean along-channel velocity [m s^{-1}]	-0.62	-0.72	-0.89
Vertical shear [s^{-2}]	-2.6	-2	-1.8
Vertical eddy viscosity [m^2 s^{-1}]	8 x 10^{-4}	1 x 10^{-3}	5 x 10^{-4}

6.6. Conclusions

This study aimed to understand the spatial variability of along-channel mixing in a micro-tidal salt wedge estuary in which currents are mainly driven by river discharge and wind. As currents can remain in a steady state direction for days, the fieldwork day was chosen to align with high river discharge conditions considering the meteorological window of low wind stress, scheduled for two days after the passage of the frontal system. We observed the structure and magnitude of current velocities and turbulence upstream of the salt wedge (T1), at the frontal

tip of the salt wedge (T2), and within the main body of the salt wedge (T3). Over a relatively short distance (~8 km) between the first and last cross-sections, the system transitions from well-mixed (T1) to highly stratified (T3).

The results showed that the main mechanisms driving mixing varied across the three cross-sections, particularly influenced by the funneling effect of the channel and the presence of the salt wedge as the cross-sections approached the ocean. The secondary flow proved to be a significant contributor to circulation and mixing in the first two transects. In T1 and T2, mixing primarily occurred within the bottom boundary layer, and although other regions experienced high velocity shear, mixing was suppressed primarily by the effects of stratification and secondary flows. However, in T3, in addition to mixing in the bottom boundary layer, the shear occurring at the pycnocline emerged as one of the main drivers of mixing. There exists a delicate balance between the effects of vertical shear, which promotes mixing on one hand but leads to vertical density stratification suppressing mixing on the other. The pycnocline, known for generating turbulence in its vicinity, however, acts as a barrier, locally blocking mixing from occurring at the flow interface.

Lastly, as expected, the funnel shape of the inlet converging towards the sea accelerated the flow from the first (T1) to the last (T3) cross-section; however, it did not result in a corresponding increase in mixing. The role of stratification in damping mixing at T3 was so pronounced that even with higher velocities and shear compared to the other transects, mixing in T3 was not superior to the previous transects, suggesting that the suppression caused by intense

stratification may be more relevant to mixing rates than an increase in flow velocity or shear. These findings are particularly relevant in microtidal estuaries at channel constrictions and choaked lagoons, where the expectation may be that strong velocity shear induced by channel narrowing would induce strong mixing and influence exchange processes.

Chapter VII: Summary of Conclusions

This thesis investigated how channel morphology, stratification, and external forcing interact to control turbulence and mixing across the estuary–shelf transition in a microtidal system. The initial hypothesis proposed that the convergent morphology at the mouth of the Patos Lagoon enhances seaward flow velocities, thereby intensifying turbulence and increasing vertical mixing.

7.1 Main Findings

The results presented in Chapters 5 and 6 evaluate this hypothesis by documenting contrasting hydrodynamic regimes under different forcing

conditions. Together, these findings demonstrate that while channel morphology exerts a strong control on flow acceleration and turbulence generation, its influence on mixing is not universal and is strongly modulated by stratification.

Under high-discharge periods (Chapter 5), the inlet behaves as a high-energy system where the convergent morphology acts as a hydraulic “nozzle,” accelerating the flow and promoting intense turbulence. Dissipation rates reach values comparable to those observed in meso- and macrotidal systems, confirming that morphological control can generate highly energetic regimes even in microtidal environments. In this scenario, inertial forcing dominates over buoyancy effects, and mixing is enhanced along the estuary–shelf transition. These results support the initial hypothesis by demonstrating that morphological convergence can intensify turbulence and contribute to mixing under weak stratification or strong momentum forcing.

However, the observations presented in Chapter 6 provide a contrasting perspective that challenges this hypothesis. Despite increased velocities and shear associated with channel convergence, mixing does not scale proportionally in the presence of strong stratification. Instead, the development of a salt wedge introduces a vertical structure in which buoyancy suppresses turbulence, limiting vertical mixing even under energetic flow conditions. This demonstrates that stratification can override the effects of shear production, acting as a primary control on mixing efficiency.

These results highlight the limitations of simplified assumptions that relate mixing directly to flow intensity, as stratification can decouple turbulence generation from effective vertical mixing. Chapter 6 provides a clear counterexample to the initial hypothesis, showing that increased flow acceleration does not necessarily result in enhanced mixing. This does not invalidate the role of morphology, but rather demonstrates that its influence is conditional and strongly dependent on the stratification regime.

Beyond these process-based insights, this thesis provides a unique spatiotemporal characterization of estuarine turbulence. The high-resolution datasets reveal a remarkable short-term variability in the Patos Lagoon system. Over timescales as short as 24 hours, the estuary can transition between a high-discharge, partially-mixed outflow regime and a highly stratified salt-wedge configuration. This variability is not governed by tidal oscillations, but primarily by changes in wind forcing and river discharge. As a result, the system exhibits rapid shifts in turbulence structure, vertical mixing, and circulation patterns, emphasizing the need to interpret estuarine dynamics in the context of transient forcing rather than periodic tidal cycles.

From a methodological perspective, this work provides the first direct in situ measurements of turbulent kinetic energy dissipation in the Patos Lagoon Estuary. By capturing rapid regime shifts through microstructure observations across contrasting conditions, it advances previous approaches based on remote sensing and modeling, offering a direct quantification of mixing processes at their

fundamental scales. These results contribute to filling a critical gap in the understanding of turbulence in non-tidal estuaries.

7.2 Broader Implications

These results have important implications for biogeochemical processes in estuarine and coastal environments, as they are fundamentally controlled by turbulence and mixing. Sediment transport, for instance, is directly influenced by turbulent resuspension and deposition in stratified flows. More broadly, variability in mixing regimes affects nutrient distribution, primary productivity, pollutant dispersion, carbon cycling, and oxygenation through its control over vertical exchange.

In particular, the strong spatial variability in mixing identified in this study highlights its potential role in regulating oxygen dynamics in these systems. Under stratified conditions, limited vertical mixing can restrict the ventilation of bottom waters, contributing to oxygen depletion and, in extreme cases, hypoxia. In this context, resolving the mechanisms that control turbulent mixing is essential for improving our understanding of how physical processes interact with biogeochemical cycles in these environments.

By providing direct measurements of turbulent kinetic energy dissipation, this work also contributes to the improvement of numerical models, which often rely on simplified parameterizations of mixing**.** The results show that turbulence

varies by several orders of magnitude within the estuarine channel, indicating that the use of uniform or overly simplified mixing coefficients may fail to capture the spatial heterogeneity of the system. Incorporating this variability into modeling frameworks may therefore lead to more realistic representations of stratified, non-tidal dynamics.

The findings of this thesis are not limited to the Patos Lagoon system and are relevant to other microtidal estuaries, coastal lagoons, and choked inlet systems where circulation is primarily driven by wind forcing and river discharge. In addition, other high-energy, partially mixed, or salt-wedge estuaries can benefit from the insights provided by this study, particularly regarding how channel morphology and stratification modulate turbulence and vertical mixing.

Finally, the Patos Lagoon represents a strategic natural laboratory for isolating the processes that control mixing in estuarine systems. The reduced influence of tides simplifies the dynamical setting, allowing the roles of wind forcing, river discharge, and channel morphology to be examined more clearly. This simplification provides insights that extend beyond microtidal environments, offering a clearer understanding of how competing physical mechanisms regulate turbulence and mixing in more complex estuarine systems.

7.3 Future Perspectives

The results presented in this thesis highlight the importance of high-resolution observations for understanding the spatial and temporal variability of estuarine turbulence. Future studies could expand on this work by combining microstructure measurements with observations under a broader range of forcing conditions, including different wind regimes and inflow scenarios, allowing turbulence to be characterized under diverse dynamical states.

Coupling microstructure observations with biogeochemical measurements (e.g., dissolved oxygen, chlorophyll, or turbidity) would also allow a direct assessment of how turbulence regulates vertical exchange and influences primary production in stratified estuarine systems. In this regard, measurements obtained alongside the CTD profiles may further support an interdisciplinary approach linking hydrodynamic processes to ecosystem functioning.

Further investigation of lateral variability in TKE dissipation, particularly in the mid- and far-field plume and at the frontal interface, would improve the understanding of the mechanisms controlling mixing across the estuary–shelf transition. Moreover, the integration of observational datasets with numerical modeling could provide a more comprehensive framework for evaluating mixing processes and their sensitivity to external forcing.

Together, these perspectives highlight the need for integrated, high-resolution approaches to advance the understanding of turbulence and mixing in complex estuarine environments.

References

ALM – Agência da Lagoa Mirim: Bacia da Lagoa Mirim, available at: https://wp.ufpel.edu.br/alm, last access: 10 September 2023.

Álvarez-Silva, O., Becker, M., Flores, R. P., Arévalo, F., Holtermann, P., Cardona, Y., and Winter, C.: The asymmetric hydrodynamic structure of a wind-dominated river plume, *Journal of Geophysical Research: Oceans*, 131, e2025JC022720, https://doi.org/10.1029/2025JC022720, 2026.

ANA – Agência Nacional de Águas e Saneamento Básico: Hidroweb database, available at: https://www.snirh.gov.br/hidroweb, last access: 10 September 2023.

Arevalo, F. M., Álvarez-Silva, O., Caceres-Euse, A., and Cardona, Y.: Mixing mechanisms at the strongly-stratified Magdalena River's estuary and plume, *Estuarine, Coastal and Shelf Science*, 277, 108077, https://doi.org/10.1016/j.ecss.2022.108077, 2022.

Ávila, R. A. and Calil, P. H. R.: Buoyancy-driven effects on turbulent diffusivity induced by a river plume in the southern Brazilian shelf, *Ocean Science Discussions*, 1–32, https://doi.org/10.5194/os-2018-66, 2018.

Armi, L. and Farmer, D. M.: Maximal two-layer exchange through a contraction with barotropic net flow, *J. Fluid Mech.*, 164, 27–51, https://doi.org/10.1017/S0022112086002458, 1986.

Barros, D.: Codebase for Barros et al. 2026 (v1.0.0), Zenodo [code], https://zenodo.org/records/18974391, 2026.

Barros, D., Bayley, T., Ross, L., and Schettini, C. A. F.: Spatial variability of turbulent mixing in a highly stratified system, *Journal of Marine Systems*, 250, 104071, https://doi.org/10.1016/j.jmarsys.2025.104071, 2025.

Bitencourt, L. P., Fernandes, E., Möller, O., and Ross, L.: The contribution of ENSO cycles to the salinity spatio-temporal variability in a bar-built microtidal estuary, *Regional Studies in Marine Science*, 40, 101496, https://doi.org/10.1016/j.rsma.2020.101496, 2020.

Blocken, B., Moonen, P., Stathopoulos, T., and Carmeliet, J.: A numerical study on the existence of the Venturi-effect in passages between perpendicular buildings, *Journal of Engineering Mechanics*, 134, 1021–1028, https://doi.org/10.1061/(ASCE)0733-9399(2008)134:12(1021), 2008.

Burchard, H., Craig, P. D., Gemmrich, J. R., Van Haren, H., Mathieu, P. P., Meier, H. E., Nimmo Smith, W. A., Prandke, H., Rippeth, T. P., Skyllingstad, E. D., Smyth, W. D., Welsh, D. J., and Wijesekera, H. W.: Observational and numerical modeling methods for quantifying coastal ocean turbulence and mixing, *Prog. Oceanogr.*, 76(4), 399–442, https://doi.org/10.1016/j.pocean.2007.09.005, 2008.

Burrage, D., Wesson, J., Martinez, C., Pérez, T., Möller Jr., O. O., and Piola, A.: Patos Lagoon Outflow within the Rio de la Plata Plume Using an Airborne Salinity Mapper: Observing an Embedded Plume, *Continental Shelf Research*, 28, 1625–1638, https://doi.org/10.1016/j.csr.2007.02.014, 2008.

Cai, W.-J., Chen, C. T. A., and Borges, A.: Carbon dioxide dynamics and fluxes in coastal waters influenced by river plumes, in: *Biogeochemical Dynamics at Major River-Coastal Interfaces*, edited by: Bianchi, T. S., Allison, M. A., and Cai, W.-J., Cambridge University Press, Cambridge, 155–173, https://doi.org/10.1017/CBO9781139136853.010, 2013.

Campos, E. J. D., Piola, A. R., Matano, R. P., and Miller, J. L.: PLATA: A synoptic characterization of the southwest Atlantic shelf under influence of the Plata River and Patos Lagoon outflows, *Continental Shelf Research*, 28, 1551–1555, https://doi.org/10.1016/j.csr.2008.03.007, 2008.

Castelão, R. M. and Möller, O. O.: A modeling study of Patos Lagoon (Brazil) flow response to idealized wind and river discharge: dynamical analysis, *Brazilian Journal of Oceanography*, 54, 1–17, https://doi.org/10.1590/S1679-87592006000100001, 2006.

Chant, R. J.: Secondary flows in a region of flow curvature: relationship with tidal forcing and river discharge, *Journal of Geophysical Research: Oceans*, 107, 3131, https://doi.org/10.1029/2001JC001082, 2002.

Chant, R. J.: Estuarine secondary circulation, in: Contemporary Issues in Estuarine Physics, edited by: Valle-Levinson, A., Cambridge University Press, Cambridge, 100–124, 2010.

Chao, S.-Y. and Boicourt, W. C.: Onset of estuarine plumes, *Journal of Physical Oceanography*, 16, 2137–2149, 1986.

Cloern, J. E.: Our evolving conceptual model of the coastal eutrophication problem, *Mar. Ecol. Prog. Ser.*, 210, 223-253, https://doi.org/10.3354/meps210223, 2001.

Cole, K. L., MacDonald, D. G., Kakoulaki, G., and Hetland, R. D.: River plume source-front connectivity, *Ocean Modelling*, 150, 101571, https://doi.org/10.1016/j.ocemod.2020.101571, 2020.

Collignon, A. and Stacey, M.: Turbulence dynamics at the shoal-channel interface in a partially stratified estuary, *Journal of Physical Oceanography*, 43, 970–989, https://doi.org/10.1175/JPO-D-12-0115.1, 2013.

Cruz, G. O. and Schettini, C. A. F.: The dynamics of the inner-shelf suspended sediments based on ADCP records and Rouse theory, *Continental Shelf Research*, 289, 105467, https://doi.org/10.1016/j.csr.2025.105467, 2025.

Delatolas, N., MacDonald, D. G., Goodman, L., Whitney, M., Huguenard, K., and Cole, K.: Comparison of structure and turbulent mixing between lateral and leading-edge river plume fronts: Microstructure observations from a T-REMUS AUV, *Estuarine, Coastal and Shelf Science*, 283, 108234, https://doi.org/10.1016/j.ecss.2023.108234, 2023.

Douglas, W., Lueck, R., and McMillan, J.: ODAS MATLAB Library Technical Manual (Version 4.3), Rockland Scientific Technical Manual, Victoria, BC, Canada, 2018.

Dorrell, R. M., Peakall, J., Sumner, E. J., Parsons, D. R., Darby, S. E., Wynn, R. B., Özsoy, E., and Tezcan, D.: Flow dynamics and mixing processes in hydraulic jump arrays: Implications for channel-lobe transition zones, *Marine Geology*, 381, 181–193, https://doi.org/10.1016/j.margeo.2016.09.009, 2016.

Dyer, K. R.: Estuarine hydrography and sedimentation: a handbook, Cambridge University Press, Cambridge, UK, 239 pp., 1979.

Efron, B. and Gong, G.: A leisurely look at the bootstrap, the jackknife and cross-validation, *The American Statistician*, 37, 36–48, 1983.

Fennel, W. and Mutzke, A.: The initial evolution of a buoyant plume, *Journal of Marine Systems*, 12, 53–68, https://doi.org/10.1016/S0924-7963(96)00088-7, 1997.

Fernandes, E. H. L., Mariño-Tapia, I., Dyer, K. R., and Moller, O. O.: The attenuation of tidal and subtidal oscillations in the Patos Lagoon estuary, *Ocean Dynamics*, 54, 348–359, https://doi.org/10.1007/s10236-004-0090-y, 2004.

Fernandes, E. H. L., Dyer, K. R., and Möller, O. O.: Spatial Gradients in the Flow of Southern Patos Lagoon, *Journal of Coastal Research*, 21, 759–769, https://doi.org/10.2112/006-NIS.1, 2005.

Fiket, Ž., Pikelj, K., Ivanić, M., Barišić, D., Vdović, N., Dautović, J., Gobac, Ž. Ž., Mikac, N., Bermanec, V., Sondi, I., and Kniewald, G.: Origin and composition of sediments in a highly stratified karstic estuary: An example of the Zrmanja River estuary (eastern Adriatic), *Regional Studies in Marine Science*, 16, 67–78, http://dx.doi.org/10.1016/j.rsma.2017.08.001, 2017.

Franzen, M. O., Silva, P., Siegle, E., and Fernandes, E. H. L.: Influence of long jetties on estuarine and coastal hydrodynamics in a microtidal estuary, *Reg. Stud. Mar. Sci.*, 59, 102809, https://doi.org/10.1016/j.rsma.2022.102809, 2023.

Garcia, C. A. E.: Environment and biota of the Patos Lagoon estuary - Hydrographic characteristics, in: Subtropical Convergence Environments - The Coast and Sea in the Southwestern Atlantic, edited by: Seeliger, U., Odebrecht, C., and Castello, J. P., Springer Verlag, New York, 18–20, 1997.

Gargett, A. E., Osborn, T. R., and Nasmyth, P. W.: Local isotropy and the decay of turbulence in a stratified fluid, *Journal of Fluid Mechanics*, 144, 231–280, https://doi.org/10.1017/S0022112084001592, 1984.

Geyer, W. R.: Three dimensional tidal flow around headlands, *Journal of Geophysical Research: Oceans*, 98, 955–966, https://doi.org/10.1029/92JC02270, 1993.

Geyer, W. R. and MacCready, P.: The estuarine circulation, *Annual Review of Fluid Mechanics*, 46, 175–197, https://doi.org/10.1146/annurev-fluid-010313-141302, 2014.

Geyer, W. R., Trowbridge, J. H., and Bowen, M. M.: The dynamics of a partially mixed estuary, *Journal of Physical Oceanography*, 30, 2035–2048, https://journals.ametsoc.org/view/journals/phoc/30/8/1520-0485_2000_030_2035_tdoapm_2.0.co_2.xml, 2000.

Geyer, W. R., Scully, M. E., and Ralston, D. K.: Quantifying vertical mixing in estuaries, *Environmental Fluid Mechanics*, 8, 495–509, https://doi.org/10.1007/s10652-008-9107-2, 2008.

Geyer, W. R., Lavery, A. C., Scully, M. E., and Trowbridge, J. H.: Mixing by shear instability at high Reynolds number, *Geophysical Research Letters*, 37, L22607, https://doi.org/10.1029/2010GL045272, 2010.

Geyer, W. R., Ralston, D. K., and Holleman, R. C.: Hydraulics and mixing in a laterally divergent channel of a highly stratified estuary, *Journal of Geophysical Research: Oceans*, 122, 4743–4760, https://doi.org/10.1002/2016JC012455, 2017.

Giddings, S. N., Fong, D. A., and Monismith, S. G.: Role of straining and advection in the intratidal evolution of stratification, vertical mixing, and longitudinal dispersion of a shallow, macrotidal, salt wedge estuary, *Journal of Geophysical Research*, 116, C03003, https://doi.org/10.1029/2010JC006482, 2011.

Goodman, L., Levine, E. R., and Lueck, R. G.: On measuring the terms of the turbulent kinetic energy budget from an AUV, *Journal of Atmospheric and Oceanic Technology*, 23, 977–999, https://doi.org/10.1175/JTECH1889.1, 2006.

Gregg, M. C., D'Asaro, E. A., Riley, J. J., and Kunze, E.: Mixing efficiency in the ocean, *Annual Review of Marine Science*, 10, 443–473, https://doi.org/10.1146/annurev-marine-121916-063643, 2018.

Grifoll, M., Jordà, G., and Espino, M.: Surface water renewal and mixing mechanisms in a semi-enclosed microtidal domain. The Barcelona harbour case, *Journal of Sea Research*, 90, 54–63, https://dx.doi.org/10.1016/j.seares.2014.02.007, 2014.

Grimm, A., Ferraz, S. E. T., and Gomes, J.: Precipitation anomalies in Southern Brazil associated with “El Niño” and “La Niña” events, *Journal of Climate*, 11, 2863–2880, https://doi.org/10.1175/1520-0442(1998)011%3C2863:PAISBA%3E2.0.CO;2, 1998.

Hartmann, C. and Schettini, C. A. F.: Aspectos hidrológicos na desembocadura da Laguna dos Patos, RS, *Revista Brasileira de Geociências*, 21, 371–377, https://doi.org/10.25249/0375-7536.1991371377, 1991.

Hetland, R. D.: Relating river plume structure to vertical mixing, *Journal of Physical Oceanography*, 35, 1667–1688, https://doi.org/10.1175/JPO2774.1, 2005.

Hetland, R. D.: The effects of mixing and spreading on density in near-field river plumes, *Dynamics of Atmospheres and Oceans*, 49, 37–53, https://doi.org/10.1016/j.dynatmoce.2008.11.003, 2010.

Holleman, R. C., Geyer, W. R., and Ralston, D. K.: Stratified turbulence and mixing efficiency in a salt wedge estuary, *Journal of Physical Oceanography*, 46, 1769–1783, https://doi.org/10.1175/JPO-D-15-0193.1, 2016.

Horner-Devine, A. R., Hetland, R. D., and MacDonald, D. G.: Mixing and transport in coastal river plumes, *Annual Review of Fluid Mechanics*, 47, 569–594, https://doi.org/10.1146/annurev-fluid-010313-141408, 2015.

Huguenard, K. D., Valle-Levinson, A., Li, M., Chant, R. J., and Souza, A. J.: Linkage between lateral circulation and near-surface vertical mixing in a coastal plain estuary, *Journal of Geophysical Research: Oceans*, 120, 4048–4067, https://doi.org/10.1002/2014JC010679, 2015.

Ibañez, C., Pont, D., and Prat, N.: Characterization of the Ebre and Rhone estuaries: A basis for defining and classifying salt-wedge estuaries, *Limnology and Oceanography*, 42, 89–101, 1997.

Ibañez, C., Saldaña, J., and Prat, N.: A model to determine the advective circulation in a three layer, salt wedge estuary: Application to the Ebre River estuary, *Estuarine, Coastal and Shelf Science*, 48, 271–279, 1999.

IBGE: Geografia do Brasil. Região Sul, Vol. 5, IBGE, 534 pp., 1977.

Ivey, G. N., Winters, K. B., and Koseff, J. R.: Density stratification, turbulence, but how much mixing?, *Annual Review of Fluid Mechanics*, 40, 169–184, https://doi.org/10.1146/annurev.fluid.39.050905.110314, 2008.

Jirka, G. H., Stolzenbach, K. D., and Adams, E. E.: Buoyant Surface Jets, *Journal of Hydraulic Engineering*, 107, 1467–1487, 1981.

Joyce, T. M.: In situ "calibration" of ship-board ADCPs, *Journal of Atmospheric and Oceanic Technology*, 6, 169–172, 1989.

Kay, D. J. and Jay, D. A.: Interfacial mixing in a highly stratified estuary: 1. Characteristics of mixing, *Journal of Geophysical Research*, 108, 3072, https://doi.org/10.1029/2000JC000252, 2003.

Kirinus, E. P., Marques, W. C., Costa, J., and Fernandes, E. H. L.: The Contribution of Waves in Mixing Processes of the Patos Lagoon Plume, *International Journal of Geosciences*, 3, 1019–1026, https://doi.org/10.4236/ijg.2012.35102, 2012.

Kjerfve, B.: Manual for investigation of hydrological processes in mangrove ecosystems, University of South Carolina, Columbia, 79 pp., 1990.

Kjerfve, B. and Magill, E. K. E.: Comparative oceanography of coastal lagoons, in: Estuarine Variability, Academic Press, 63–81, https://doi.org/10.1016/B978-0-12-761890-6.50009-5, 1989.

Krvavica, N., Gotovac, H., and Loncar, G.: Salt-wedge dynamics in microtidal Neretva River estuary, *Regional Studies in Marine Science*, 43, 101713, https://doi.org/10.1016/j.rsma.2021.101713, 2021.

Lacy, J. R. and Monismith, S. G.: Secondary currents in a curved, stratified, estuarine channel, *Journal of Geophysical Research*, 106, 31283–31302, https://doi.org/10.1029/2000JC000606, 2001.

Lohrenz, S. E., Cai, W.-J., Chakraborty, S., Gundersen, K., and Murrell, M. C.: Nutrient and carbon dynamics in a large river-dominated coastal ecosystem: the Mississippi-Atchafalaya River system, in: *Biogeochemical Dynamics at Major River-Coastal Interfaces*, Cambridge University Press, 448–472, https://doi.org/10.1017/CBO9781139136853.023, 2013.

Lueck, R.: Calculating the rate of dissipation of turbulent kinetic energy, Rockland Scientific Technical Note 028, Victoria, BC, Canada, 2013.

Lueck, R., Wolk, F., and Black, K.: Measuring tidal channel turbulence with a Vertical Microstructure Profiler (VMP), Rockland Scientific Technical Note 026, Victoria, BC, Canada, 2013.

Lueck, R., Murowinski, E., and McMillan, J.: A Guide to Data Processing, Rockland Scientific Technical Note 039, Victoria, BC, Canada, 2020.

MacCready, P., and Geyer, W. R.: Advances in estuarine physics, Annual Review of Marine Science, 2, 35–58, https://doi.org/10.1146/annurev-marine-120308-081015, 2010.

MacDonald, D. G. and Geyer, W. R.: Turbulent energy production and entrainment at a highly stratified estuarine front, *Journal of Geophysical Research*, 109, C05004, https://doi.org/10.1029/2003JC002094, 2004.

MacDonald, D. G., Goodman, L., and Hetland, R. D.: Turbulent dissipation in a near-field river plume: A comparison of control volume and microstructure observations with a numerical model, *Journal of Geophysical Research: Oceans*, 112, C05026, https://doi.org/10.1029/2006JC004075, 2007.

Machado, A. A. and Calliari, L. J.: Synoptic systems generators of extreme wind in Southern Brazil: atmospheric conditions and consequences in the coastal zone, *Journal of Coastal Research*, 75, 1182–1186, https://doi.org/10.2112/SI75-237.1, 2016.

Marques, W. C., Fernandes, E. H. L., Monteiro, I. O., and Möller, O. O.: Numerical modeling of the Patos Lagoon coastal plume, Brazil, *Continental Shelf Research*, 29, 556–571, https://doi.org/10.1016/j.csr.2008.09.022, 2009.

Marques, W. C., Fernandes, E. H. L., Moraes, B. C., Möller, O. O., and Malcherek, A.: Dynamics of the Patos Lagoon coastal plume and its contribution to the deposition pattern of the southern Brazilian inner shelf, *Journal of Geophysical Research*, 115, C10045, https://doi.org/10.1029/2010JC006190, 2010.

Marques, W. C., Stringari, C. E., and Eidt, R. T.: The exchange processes of the Patos Lagoon estuary – Brazil: a typical El Niño year versus a normal meteorological conditions year, *Advances in Water Resource and Protection*, 2, 11–20, 2014.

McPherson, R. A., Stevens, C. L., and O'Callaghan, J.: Turbulent scales observed in a river plume entering a fjord, *Journal of Geophysical Research: Oceans*, 124, 9190–9208, https://doi.org/10.1029/2019JC015448, 2019.

McPherson, R. A., Stevens, C. L., O'Callaghan, J. M., Lucas, A. J., and Nash, J. D.: The role of turbulence and internal waves in the structure and evolution of a near-field river plume, *Ocean Science*, 16, 799–815, https://doi.org/10.5194/os-16-799-2020, 2020.

Miles, J. W.: On the stability of heterogeneous shear flows, *J. Fluid Mech.*, 10, 496–508, https://doi.org/10.1017/S0022112061000305, 1961.

Miranda, L. B., Castro, B. M., and Kjerfve, B.: Princípios de oceanografia física de estuários, Editora da Universidade de São Paulo, São Paulo, 2002.

Miranda, L. P., Machado, J. P., Saraiva, J. B., Barros, D. G., Goulart, E. S., and Andrade, H. N.: Meteoceanographic patterns associated with severe coastal storms along the southern coast of Brazil, *Meteorology*, 5, 1, https://doi.org/10.3390/meteorology5010001, 2026.

Möller, O. O. and Castaing, P.: Hydrographical characteristics of the estuarine area of Patos Lagoon (30°S, Brazil), in: Estuaries of South America, edited by: Perillo, G. M. E., Pino Quivira, M. C., Piccolo, M. C., and Pino-Quivira, M., Springer, Berlin, 83–100, https://doi.org/10.1007/978-3-642-60131-6_5, 1999.

Möller, O. O. and Fernandes, E. H. L.: Hidrologia e hidrodinâmica, in: O Estuário da Lagoa dos Patos: Um século de transformações, edited by: Seeliger, U. and Odebrecht, C., FURG, Rio Grande, 17–30, 2010.

Möller, O. O., Lorenzzentti, J. A., Stech, J. L., and Mata, M. M.: The Patos Lagoon summertime circulation and dynamics, *Continental Shelf Research*, 16, 335–351, https://doi.org/10.1016/0278-4343(95)00014-R, 1996.

Möller, O. O., Castaing, P., Salomon, J. C., and Lazure, P.: The influence of local and non-local forcing effects on the subtidal circulation of Patos Lagoon, *Estuaries*, 24, 297–311, https://doi.org/10.2307/1352953, 2001.

Möller, O. O., Castaing, P., Fernandes, E. H. L., and Lazure, P.: Tidal frequency dynamics of a Southern Brazil coastal lagoon: Choking and short period forced oscillations, *Estuaries and Coasts*, 30, 311–320, https://doi.org/10.1007/BF02700173, 2007.

Monismith, S. G.: Mixing in estuaries, in: Contemporary Issues in Estuarine Physics, edited by: Valle-Levinson, A., Cambridge University Press, Cambridge, 145–185, https://doi.org/10.1017/CBO9780511676567.008, 2010.

Monteiro, I. O., Marques, W. C., Fernandes, E. H. L., Gonçalves, R. C., and Möller Jr., O. O.: On the effect of Earth rotation, river discharge, tidal oscillations, and wind in the dynamics of the Patos Lagoon coastal plume, *Journal of Coastal Research*, 27, 120–130, 2011.

Nash, J. D. and Moum, J. N.: River plumes as a source of internal gravity waves in the coastal ocean, *Nature*, 437, 400–403, https://doi.org/10.1038/nature03936, 2005.

Nash, J. D., Kilcher, L. F., and Moum, J. N.: Structure and composition of a strongly stratified, tidally pulsed river plume, *Journal of Geophysical Research*, 114, C00B12, https://doi.org/10.1029/2008JC005036, 2009.

Nidzieko, N. J., Hench, J. L., and Monismith, S. G.: Lateral circulation in well-mixed and stratified estuarine flows with curvature, *Journal of Physical Oceanography*, 39, 831–851, https://doi.org/10.1175/2008JPO4017.1, 2009.

O'Donnell, J., Ackleson, S. G., and Levine, E. R.: On the spatial scales of a river plume, *Journal of Geophysical Research*, 113, C04017, https://doi.org/10.1029/2007JC004440, 2008.

Paiva, B. P. and Schettini, C. A. F.: Circulation and transport processes in a tidally forced salt-wedge estuary: the São Francisco River estuary, Northeast Brazil, *Regional Studies in Marine Science*, 41, 101602, 2021.

Pérez-Santos, I., Castro, L., Ross, L., Niklitschek, E., Mayorga, N., Cubillos, L., Gutierrez, M., Escalona, E., Castillo, M., Alegría, N., and Daneri, G.: Turbulence and hypoxia contribute to dense biological scattering layers in a Patagonian fjord system, *Ocean Science*, 14, 1185–1206, https://doi.org/10.5194/os-14-1185-2018, 2018.

Peters, H.: Observations of stratified turbulent mixing in an estuary: Neap-to-spring variations during high river flow, *Estuarine, Coastal and Shelf Science*, 45, 69–88, https://doi.org/10.1006/ecss.1996.0180, 1997.

Peters, H.: Spatial and temporal variability of turbulent mixing in an estuary, *Journal of Marine Research*, 57, 805–846, 1999.

Peters, H. and Bokhorst, R.: Microstructure observations of turbulent mixing in a partially mixed estuary. Part I: Dissipation rate, *Journal of Physical Oceanography*, 30, 1232–1244, https://doi.org/10.1175/1520-0485(2000)030<1232:MOOTMI>2.0.CO;2, 2000.

Piola, A. R., Matano, R. P., Palma, E. D., Möller Jr., O. O., and Campos, E. J. D.: The influence of the Plata River discharge on the western South Atlantic shelf, *Journal of Geophysical Research: Oceans*, 110, C12038, https://doi.org/10.1029/2004GL021638, 2005.

Rabouille, C., Conley, D. J., Dai, M., Cai, W.-J., Chen, C. T. A., Lansard, B., Green, R., Yin, K., Harrison, P. J., Dagg, M., and McKee, B.: Comparison of hypoxia among four river-dominated ocean margins: The Changjiang (Yangtze), Mississippi, Pearl, and Rhône rivers, *Cont. Shelf Res.*, 28, 1527–1537, https://doi.org/10.1016/j.csr.2008.01.020, 2008.

Ralston, D. K., Geyer, W. R., and Lerczak, J. A.: Structure, variability, and salt flux in a strongly forced salt wedge estuary, *Journal of Geophysical Research: Oceans*, 115, C06005, https://doi.org/10.1029/2009JC005806, 2010.

Ross, L., Huguenard, K. D., and Sottolichio, A.: Intratidal and fortnightly variability of vertical mixing in a macrotidal estuary: The Gironde, *Journal of Geophysical Research: Oceans*, 124, 2641–2659, https://doi.org/10.1029/2018JC014456, 2019a.

Ross, L., Sottolichio, A., Maury, T., Lesourd, S., and Gardel, A.: Intratidal and subtidal circulation in a tropical estuary during wet season: The Maroni French Guiana, *Journal of Marine Science and Engineering*, 7, 433, https://doi.org/10.3390/jmse7120433, 2019b.

Ross, L., Alahmed, S., Smith, S. M. C., and Roberts, G.: Tidal and subtidal transport in short, tidally-driven estuaries with low rates of freshwater input, Cont. Shelf Res., 224, 104453, https://doi.org/10.1016/j.csr.2021.104453, 2021.

Santa-Rosa, P. R. A. and Schettini, C. A. F.: Daily variability of estuary-shelf exchange at the Lagoa dos Patos's mouth, *Regional Studies in Marine Science*, 77, 103633, https://doi.org/10.1016/j.rsma.2024.103633, 2024.

Schettini, C. A. F.: Ocean Data Analysis with Python/Jupyter (v1.0), Zenodo [code], https://doi.org/10.5281/zenodo.15442937, 2021.

Schettini, C. A. F., Kuroshima, K. N., Pereira Filho, J., Rörig, L. R., and Resgalla Jr., C.: Oceanographic and ecological aspects of the Itajaí-Açu River plume during a high discharge period, *Anais da Academia Brasileira de Ciências*, 70, 335–351, 1998.

Schettini, C. A. F., Ricklefs, K., Truccolo, E. C., and Golbig, V.: Synoptic hydrography of highly stratified estuary, *Ocean Dynamics*, 56, 308–319, http://dx.doi.org/10.1007/s10236-006-0066-1, 2006.

Sharples, J., Coates, M. J., and Sherwood, J. E.: Quantifying turbulent mixing and oxygen fluxes in a Mediterranean-type, microtidal estuary, *Ocean Dynamics*, 53, 126–136, https://doi.org/10.1007/s10236-003-0037-8, 2003.

Shih, L. H., Koseff, J. R., Ivey, G. N., and Ferziger, J. H.: Parametrization of turbulent fluxes and scales using homogeneous sheared stably stratified turbulence simulations, *Journal of Fluid Mechanics*, 525, 193–214, https://doi.org/10.1017/S0022112004002587, 2005.

Silva, P. D., Lisboa, P. V., and Fernandes, E. H.: Changes on the fine sediment dynamics after the Port of Rio Grande expansion, *Advances in Geosciences*, 39, 123–127, http://dx.doi.org/10.5194/adgeo-39-123-2015, 2015.

Simão, R., Tavora, J., Salama, S., Weschenfelder, J., Molano Cárdenas, S. M., Gonçalves, G. M. S., Collares, G. L., Cavalcanti, A., Mendes, C. R. B., Barros, D., Pereira, E., Galetti, J., Möller, O., Jamet, C., and Fernandes, E. H.: Unprecedented suspended solids load caused by record-breaking extremes in southern Brazil: The May 2024 event, *Front. Mar. Sci.*, 12, 1726787, https://doi.org/10.3389/fmars.2025.1726787, 2026.

Simpson, J. and Sharples, J.: Introduction to the Physical and Biological Oceanography of Shelf Seas, Cambridge University Press, Cambridge, 2012.

Sims, R. P., Bedington, M., Schuster, U., Watson, A. J., Kitidis, V., Torres, R., Findlay, H. S., Fishwick, J. R., Brown, I., and Bell, T. G.: Tidal mixing of estuarine and coastal waters in the western English Channel is a control on spatial and temporal variability in seawater CO_2, *Biogeosciences*, 19, 1657–1674, https://doi.org/10.5194/bg-19-1657-2022, 2022.

Soares, I. D., Kourafalou, V., and Lee, T. N.: Circulation on the western South Atlantic continental shelf: 1. Numerical process studies on buoyancy, *Journal of Geophysical Research*, 112, C04002, https://doi.org/10.1029/2006JC003618, 2007a.

Soares, I. D., Kourafalou, V., and Lee, T. N.: Circulation on the western South Atlantic continental shelf: 2. Spring and autumn realistic simulations, *Journal of Geophysical Research*, 112, C04003, https://doi.org/10.1029/2006JC003620, 2007b.

Spicer, P.: Mixing Processes in Tidally Pulsed River Plumes: Mechanisms, Significance, and Variability, PhD thesis, University of Maine, Orono, USA, available at: https://digitalcommons.library.umaine.edu/etd/3612, 2022.

Stacey, M. T., Monismith, S. G., and Burau, J. R.: Observations of turbulence in a partially stratified estuary, J. Phys. Oceanogr., 29, 1950–1970, https://doi.org/10.1175/1520-0485(1999)029<1950:OOTIAP>2.0.CO;2, 1999.

Stacey, M. T., Rippeth, T. P., and Nash, J. D.: Turbulence and Stratification in Estuaries and Coastal Seas, in: Treatise on Estuarine and Coastal Science, edited by: Wolanski, E. and McLusky, D., Elsevier, 121–148, https://doi.org/10.1016/B978-0-12-374711-2.00204-7, 2012.

Stech, J. L. and Lorenzzetti, J. A.: The response of the South Brazil Bight to the passage of wintertime cold fronts, *Journal of Geophysical Research: Oceans*, 97, 9507–9520, https://doi.org/10.1029/92JC00486, 1992.

Stips, A.: Dissipation measurement: Theory, in: Marine Turbulence: Theories, Observations and Models, edited by: Baumert, H. Z., Simpson, J. H., and Sündermann, J., Cambridge University Press, Cambridge, 115–126, 2005.

Thomson, R. E. and Emery, W. J.: Data Analysis Methods in Physical Oceanography, 3rd edn., Elsevier, Waltham, MA, 2014.

Thorpe, S. A.: An Introduction to Ocean Turbulence, Cambridge University Press, Cambridge, 266 pp., 2007.

Thorpe, S. A., Malarkey, J., Voet, G., Alford, M. H., Girton, J. B., and Carter, G. S.: Application of a model of internal hydraulic jumps, *Journal of Fluid Mechanics*, 834, 125–148, https://doi.org/10.1017/jfm.2017.646, 2017.

Trowbridge, J. H., Geyer, W. R., Bowen, M. M., and Williams, A. J.: Near-bottom turbulence measurements in a partially mixed estuary: turbulent energy balance, velocity structure, and along-channel momentum balance, *Journal of Physical Oceanography*, 29, 3056–3072, https://doi.org/10.1175/1520-0485(1999)029%3C3056:NBTMIA%3E2.0.CO;2, 1999.

Turner, J. S.: Buoyancy Effects in Fluids, Cambridge University Press, 367 pp., 1973.

Valle-Levinson, A., Klinck, J. M., and Wheless, G. H.: Inflows/outflows at the transition between a coastal plain estuary and the coastal ocean, *Continental Shelf Research*, 16, 1819–1847, https://doi.org/10.1016/0278-4343(96)00016-7, 1996.

Valle-Levinson, A., Huguenard, K., Ross, L., Branyon, J., MacMahan, J., and Reniers, A.: Tidal and nontidal exchange at a subtropical inlet: Destin Inlet, Northwest Florida, *Estuarine, Coastal and Shelf Science*, 155, 137–147, https://doi.org/10.1016/j.ecss.2015.01.020, 2015.

Valle-Levinson, A., Schettini, C. A. F., and Truccolo, E. C.: Subtidal variability of exchange flows produced by river pulses, wind stress and fortnightly tides in a subtropical stratified estuary, *Estuarine, Coastal and Shelf Science*, 221, 72–82, 2019.

Vaz, A. C., Möller Jr., O. O., and Almeida, T. L.: Análise quantitativa da descarga dos rios afluentes da Lagoa dos Patos, *Atlântica*, 28, 13–24, https://doi.org/10.5088/atlantica.v28i1.1724, 2011.

Venayagamoorthy, S. K. and Koseff, J. R.: On the flux Richardson number in stably stratified turbulence, *Journal of Fluid Mechanics*, 798, R1, https://doi.org/10.1017/jfm.2016.340, 2016.

Venturi, G. B.: Experimental inquiries concerning the principle of the lateral communication of motion in fluids: Applied to the explanation of various hydraulic phenomena, translated by: Nicholson, W., printed for J. Taylor, viii, 75 pp., 1799.

Wang, B., Giddings, S. N., Fringer, O. B., Gross, E. S., Fong, D. A., and Monismith, S. G.: Modeling and understanding turbulent mixing in a macrotidal salt wedge estuary, *J. Geophys. Res. Oceans*, 116, C02036, https://doi.org/10.1029/2010JC006135, 2011.

Wang, J., Yu, F., Ren, Q., Si, G., and Wei, C.: Spatial and temporal variability of turbulent mixing in the near-field of the Changjiang River, *Journal of Oceanology and Limnology*, 38, 1138–1152, https://doi.org/10.1007/s00343-020-0008-7, 2020.

Wu, D., Chen, J., Wang, K., Ni, X., Li, D., Zeng, D., Fan, W., and Xu, D.: The Changjiang River plume shifts from carbon source to sink when net community production exceeds a threshold in early autumn, *Sci. Total Environ.*, 888, 164126, https://doi.org/10.1016/j.scitotenv.2023.164126, 2023.

Yuk, J. H. and Aoki, S.: Impact of jetty construction on the current and ecological systems in the estuary with a narrow inlet, *Journal of Coastal Research*, 784–788, 2007.

Zavialov, P. O., Pelevin, V. V., Belyaev, N. A., Izhitskiy, A. S., Konovalov, B. V., Krementskiy, V. V., Goncharenko, I. V., Osadchiev, A. A., Soloviev, D. M., Garcia, C. A. E., Pereira, E. S., Sartorato, L., and Möller, O. O.: High resolution LiDAR measurements reveal fine internal structure and variability of sediment-carrying coastal plume, *Estuarine, Coastal and Shelf Science*, 205, 40–45, https://doi.org/10.1016/j.ecss.2018.01.008, 2018.

Appendix A – Microstructure Data Processing Workflow

A.1 Overview

This appendix provides a structured description of the MCTD data processing, from raw acquisition to the final turbulence estimates presented in this thesis. The primary objective is to ensure transparency and reproducibility of the turbulent kinetic energy dissipation rate (ϵ) calculations.

Processing microstructure data is a complex and multi-step procedure that is often not fully documented in scientific articles due to space limitations. Therefore, this appendix is intended as a practical, step-by-step reference for researchers working with similar datasets.

The procedures presented here reflect the methods developed and applied in this study, combining manufacturer guidelines (Rockland Scientific) with adaptations implemented for the specific conditions of the Patos Lagoon system.

Section A.2 introduces the fundamental MATLAB functions used to convert raw binary data into physical units, based on the ODAS processing library. Subsequent sections describe the processing steps in detail, including data inspection, microstructure processing, data integration, and parameter estimation.

A.2 Understanding MATLAB Functions and General Workflow

This section summarizes the key elements of the Rockland Scientific processing framework required to convert raw MCTD data into physical variables. It does not aim to replace the official manuals, but rather to highlight the essential components needed to initiate data processing. Some descriptions presented here are adapted from Rockland documentation and technical notes, with emphasis on the aspects most relevant to the analysis procedure implemented in this study.

The first step in the processing chain is the conversion of raw binary data into physical units. This is achieved using the ODAS (Ocean Data Acquisition System) MATLAB library provided by Rockland Scientific. To enable this process,

the ODAS library must be added to the MATLAB path, and the data directory must contain the corresponding field data files. Data files can be converted into physical units using the odas_p2mat or quick_look functions (Douglas et al., 2018).

A.2.1 ODAS_P2MAT

The function *odas_p2mat.m* converts raw binary data into data vectors in physical units, including both raw signals (Table 1) and derived signals (Table 2) (Lueck et al., 2020). The resulting data vectors are saved in a MATLAB (.mat) file with the same name as the original .P file.

The general syntax is:

```
>> odas_p2mat('fname', convert_info)
```

where:

`fname`: name of the file to be processed (file extension optional)

`convert_info`: optional structure containing processing parameters

If the convert_info structure is not provided, default parameters are used.

Table 1: List of main channel ids and their corresponding sensors and signals. Reproduced from Lueck et al. (2020).

ID	Name	Type	f_s	Units	Description
0	Gnd	gnd	slow	counts	Ground on first μASTP board
1	Ax	piezo	fast	counts	Piezo-vibration sensor x-axis
2	Ay	piezo	fast	counts	Piezo-vibration sensor y-axis
4	T1	therm	slow	counts	Temperature without pre-emphasis
5	T1_dT1	therm	fast	counts	Temperature with pre-emphasis
6	T2	therm	slow	counts	Temperature without pre-emphasis
7	T2_dT2	therm	fast	counts	Temperature with pre-emphasis
8	sh1	shear	fast	s^{-1}	Along-path gradient of u_1 (i.e. ∇u_1)
9	sh2	shear	fast	s^{-1}	Along-path gradient of u_2 (i.e. ∇u_2)
10	P	poly	slow	counts	Pressure without pre-emphasis
11	P_dP	poly	slow	counts	Pressure with pre-emphasis
12	PV	poly	slow	V	Voltage across pressure transducer
15	EMC_Cur	voltage	fast	V	EMC drive current reference signal
16,17	SBT1	sbt	slow	°C	Temperature from Sea-Bird SBE3F
18,19	SBC1	sbc	slow	mS cm^{-1}	Conductivity from Sea-Bird SBE3F
32	V_Bat	voltage	slow	V	Voltage of the main power supply
40	Incl_Y	inclxy	slow	°	θ_y, inclinometer; pitch
41	Incl_X	inclxy	slow	°	θ_x, inclinometer; roll
42	Incl_T	inclt	slow	°C	Temperature of inclinometer
48, 49	JAC_C	jac_c	slow	mS cm^{-1}	Conductivity from JAC CT
50	JAC_T	jac_t	slow	°C	Temperature from JAC CT
52	Chlorophyll	poly	fast	ppb	Chlorophyll from JAC Fluorometer
53	Turbidity	poly	fast	FTU	Turbidity from JAC Turbudity
64	C1	ucond	slow	counts	Conductivity without pre-emphasis
65	C1_dC1	ucond	fast	counts	Conductivity with pre-emphasis
66	C2	ucond	slow	counts	Conductivity without pre-emphasis
67	C2_dC2	ucond	fast	counts	Conductivity with pre-emphasis
80	Mz	magn	slow	µT	Vertical component of magnetic field
81	My	magn	slow	µT	Horizontal component of magnetic field
82	Mx	magn	slow	µT	Horizontal component of magnetic field
144	U_EM	aem1g_d	slow	$m\,s^{-1}$	Current speed from JAC EM digital output
255	ch255	–	slow	–	7FF0 hexi-decimal, 32 752 Decimal

Table 2: List of derived signals and parameters in the mat-files. Reproduced from Lueck et al. (2020).

Name	f_s	Units	Description
cfgobj	–	–	Parsed configuration file. (Structure)
C1_fast	fast	mS cm^{-1}	High-resolution conductivity.
C1_slow	slow	mS cm^{-1}	High-resolution conductivity.
date	–	–	Completion date of first record (String)
Day	–	–	Day of completion of first record.
filetime	–	–	Start time of the file in Matlab time format.
fs_fast	–	s^{-1}	Sampling rate of fast channels.
fs_slow	–	s^{-1}	Sampling rate of slow channels.
fullPath	–	–	Path where data is stored.
gradC1	fast	mS m^{-1}	Conductivity gradient, $\partial C_1/\partial z$.
gradC2	fast	mS m^{-1}	Conductivity gradient, $\partial C_2/\partial z$.
gradT1	fast	°C m^{-1}	Temperature gradient, $\partial T_1/\partial z$.
gradT2	fast	°C m^{-1}	Temperature gradient, $\partial T_2/\partial z$.
header	–	–	The header of every 1-second record. (Matrix)
header_version	–	–	Version of the header.
Hour	–	–	Hour of completion of first record.
input_parameters	–	–	Parameters passed to `odas_p2mat.m`. Structure.
Milli	–	–	Millisecond of completion of the first record.
Minute	–	–	Minute of completion of the first record.
Month	–	–	Month of completion of the first record.
odas_version	–	–	Version number of the ODAS Matlab library used to generate mat-file
P_fast	fast	dbar	High-resolution pressure.
P_slow	slow	dbar	High-resolution pressure.
params	–	–	Parameters used by `odas_p2mat.m`. (Structure)
Second	–	–	Second of completion of the first record.
setupfilestr	–	–	Information from the setup file. (String)
speed_fast	fast	m s^{-1}	The speed of the instrument (as per Table 1).
speed_slow	slow	m s^{-1}	The speed of the instrument (as per Table 1).
t_fast	fast	s	Fast sampling time since the start of the file.
t_fast_YD	fast	day	Fast sampling time in year-day.
t_slow	slow	s	Slow sampling time since the start of the file.
t_slow_YD	slow	day	Slow sampling time in year-day.
temperature_fast	fast	°C	Temperature to calculate kinematic viscosity.
time	–	–	Completion time of first record. (String)
T1_fast	fast	°C	High-resolution temperature.
T1_slow	slow	°C	High-resolution temperature.
T2_fast	fast	°C	High-resolution temperature.
T2_slow	slow	°C	High-resolution temperature.
vehicle_info	–	–	Vehicle-specific info used by `odas_p2mat.m`. (Structure)
W_fast	fast	m s^{-1}	The rate of change of pressure, W.
W_slow	slow	m s^{-1}	The rate of change of pressure, W.
Year	–	–	Year of completion of first record.

A.2.2 QUICK_LOOK

The function *quick_look.m* is designed as a multipurpose tool that facilitates an initial assessment of the dataset. Its main functionalities include (Lueck et al., 2020):

1. Visualization of the contents of a Rockland data file
2. Computation of spectra over a selected depth or time interval
3. Estimation of the turbulent kinetic energy dissipation rate (ϵ) profile

Regarding the visualization functionality, the data from a selected profile are displayed in a set of eight diagnostic plots, which are subsequently used for visual inspection and quality control, as described in Section A.3.

To execute *quick_look.m*, the following command is used:

```
>> diss = quick_look( 'fname', P_start, P_end, ql_info)
```

where:

`diss`: output structure containing the processed data

`fname`: name of the input file (file extension optional)

`P_start`: initial pressure defining the data segment used for spectral estimates; this argument can be left empty ([ ]) if spectral analysis is not required

`P_end`: final pressure defining the data segment used for spectral estimates; this argument can also be left empty ([ ])

`ql_info`: input structure defining processing parameters, which can be replaced by a customized configuration.

The syntax and parameter definitions are consistent with the ODAS implementation described in Lueck et al. (2020)

The input structure *ql_info* contains processing parameters associated with both *quick_look.m* and *odas_p2mat.m*. Each parameter is uniquely defined and applied to one of these functions. If *quick_look* or *odas_p2mat.m* is called without input arguments, default parameter values are automatically assigned.

A customized *ql_info* structure can be defined to adapt the processing to specific environmental conditions. In this study, a tailored configuration was developed for the Patos Lagoon environment.

A comparison between the default *ql_info* configuration and the customized *ql_info_patos* used in this study is presented in Figure 1 (Lueck, 2013; Lueck et al., 2020).

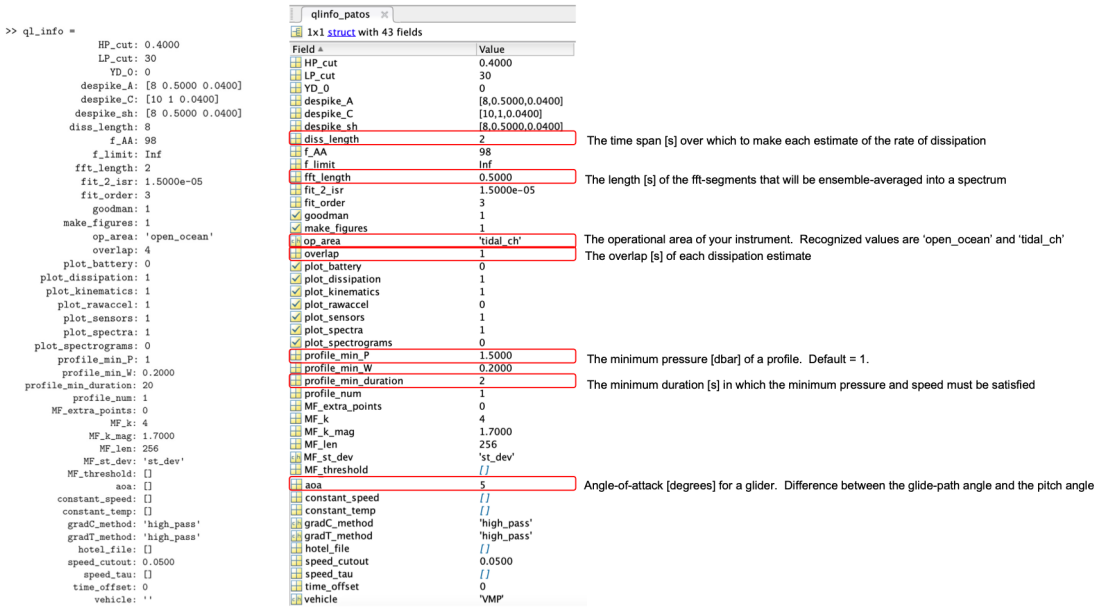


Figure 1: Comparison between the default *ql_info* configuration and the customized *ql_info_patos* used in this study. Highlighted parameters indicate the main modifications applied to adapt the processing to the conditions of the Patos Lagoon inlet. In particular, adjustments to *diss_length* and *fft_length* reflect changes in the temporal resolution of ε estimates, while modifications to *profile_min_P* and *profile_min_duration* allow the inclusion of shorter and shallower valid segments. The selection of *op_area* = *'tidal_ch'* represents the confined and high-shear conditions characteristic of the study area.

The main differences between the default and customized configurations reflect adjustments to the temporal resolution and data selection criteria used in the dissipation estimates. In particular, parameters such as *diss_length* and *fft_length* were reduced, allowing for higher spatial resolution in ϵ estimates, which is essential in a highly variable and energetic environment such as the Patos Lagoon inlet.

Additionally, the reduction of *profile_min_P* and *profile_min_duration* enabled the inclusion of shorter and shallower valid segments, increasing data usability in regions with strong vertical gradients. The selection of the operational mode (*op_area = 'tidal_ch'*) further reflects the confined and high-shear conditions characteristic of the study area. These adjustments allow the analysis to better represent the dynamic and stratified conditions observed in inlet region.

At this stage, the fundamental tools required to convert raw MCTD data into physical variables have been introduced, including the definition of a customized *ql_info* structure and the initial application of *quick_look.m*. These steps represent the preparatory stage of the data processing.

The complete processing workflow can then be described as a sequence of structured steps, outlined below.

A.2.3 General Workflow

The data processing was conducted in four main stages:

1. Initial data inspection and quality control (MATLAB)
2. Microstructure processing and ϵ estimation (MATLAB)
3. Data integration and synchronization with ADCP measurements (Python)
4. Computation of derived parameters and visualization (Python)

Each stage is described in detail in the following sections. Section A.3 focuses on the inspection and quality control of raw data through visualization routines in MATLAB. Section A.4 presents the main microstructure processing procedures. Section A.5 describes the pre-processing and synchronization of ADCP and MCTD datasets in Python, and Section A.6 details the computation of derived parameters and the generation of figures.

A.3 Initial Data Inspection and Quality Control

Processing begins with the import of raw MCTD data into MATLAB, followed by an initial execution of the *quick_look* function. This first-pass analysis provides a rapid assessment of data quality and helps identify potential issues such as signal noise, probe malfunction, or anomalous profiles.

The diagnostic plots presented in this section are generated using this routine and are described following the methodology outlined in Lueck et al. (2020). The objective here is not to reproduce the full technical documentation, but rather to highlight the key features used for data inspection and quality control within the context of this study.

A preliminary visualization routine is used to screen all profiles, after which each profile is examined individually. This inspection allows for:

- identification of noisy or contaminated signals
- detection of probe instabilities

- verification of consistent descent rates
- verification of a physically consistent angle of attack
- exclusion of invalid segments

Profiles that do not meet the established quality criteria are discarded prior to further analysis.

The primary diagnostic plots used in this stage include kinematic properties of the profile (Section A.3.2), CTD variables (Section A.3.3), spectral estimates in both frequency and wavenumber domains (Section A.3.4), and the ϵ profile computed over the full cast (Section A.3.5). Selected examples are presented below to illustrate the evaluation procedure.

A.3.1 Pressure Record and Profile Selection

The first figure generated by *quick_look.m* (Fig. 2) displays the pressure record for the entire data file, highlighting in red the specific profile selected for analysis. This visualization is useful to ensure that the correct profile has been identified prior to further processing.

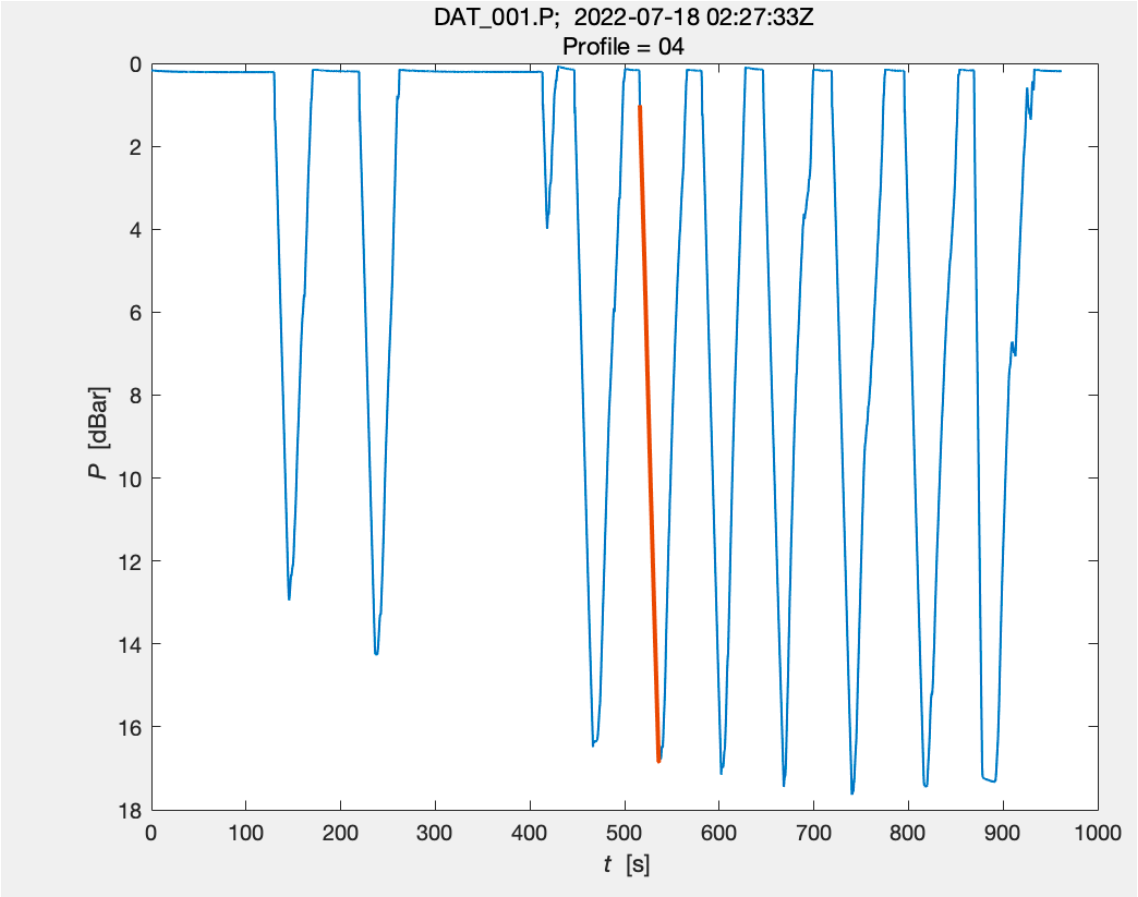


Figure 2: Pressure record for the entire data file, with the selected profile highlighted in red.

A.3.2 Kinematics (Tilt Angle and Descent Rate)

For each instrument deployment, *quick_look.m* displays the kinematic properties of an individual profile, including the descent rate and the instrument inclination (Fig. 3a–b).

For vertically profiling instruments, such as the MCTD, the first kinematic figure consists of two subpanels. The left panel shows the roll angle (θx), measured by the onboard inclinometer. A free-falling instrument such as the

MCTD is expected to descend through the water column with minimal rotation, typically within ±5°. Under calm conditions, roll angles are generally smaller than ±0.5°. Larger tilt angles may indicate that the tether is not sufficiently slack, causing the instrument to be influenced by the motion of the deployment platform.

The right panel shows the rate of change of pressure, which corresponds to the vertical descent velocity. Upon deployment, the instrument is expected to accelerate rapidly from approximately 0.6 to 0.8 dbar s^{-1}, reaching its nominal operating speed. In this study, descent rates between about 0.7 and 0.9 dbar s^{-1} were considered acceptable, with values close to 0.8 dbar s^{-1} regarded as optimal.

These kinematic conditions are governed by the instrument configuration. A mesh drag plate mounted on the upper section increases hydrodynamic resistance, stabilizes the profiler orientation, and promotes a near-vertical descent, while ballast weights at the lower end control buoyancy and ensure a stable free-fall profiling behavior.

Profiles that deviate from these expected kinematic conditions are considered unreliable and are excluded from further analysis. This selection step ensures that turbulence estimates are based on measurements acquired under stable and physically consistent profiling conditions.

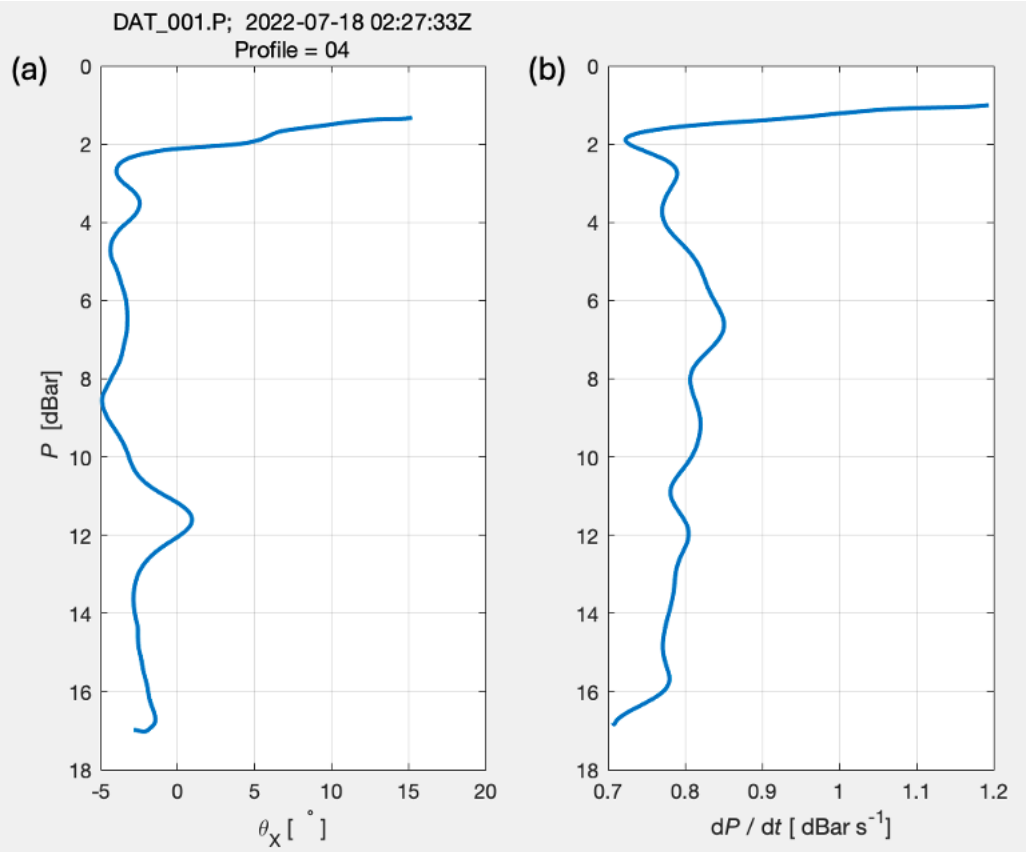


Figure 3: Kinematic properties of a representative MCTD profile. **(a)** Left panel: roll angle (θx) measured by the onboard inclinometer; acceptable values are typically within ±5°, with smaller variations indicating a stable, near-vertical descent. **(b)** Right panel: vertical descent velocity expressed as dP/dt; the instrument is expected to accelerate toward its nominal operating speed of approximately 0.8 dbar s^{-1}, with values between ~0.7 and 0.9 dbar s^{-1} considered acceptable.

A.3.3 CT (Conductivity–Temperature)

If the instrument is equipped with a conductivity–temperature (CT) sensor, such as those manufactured by Sea-Bird Electronics (SBE) or JFE Advantech

(JAC), the *quick_look.m* function generates a figure displaying vertical profiles of temperature, conductivity, salinity, and potential density as functions of pressure. The resulting figure displays, from left to right, temperature, conductivity, salinity, and potential density anomaly (Fig. 4a–d).

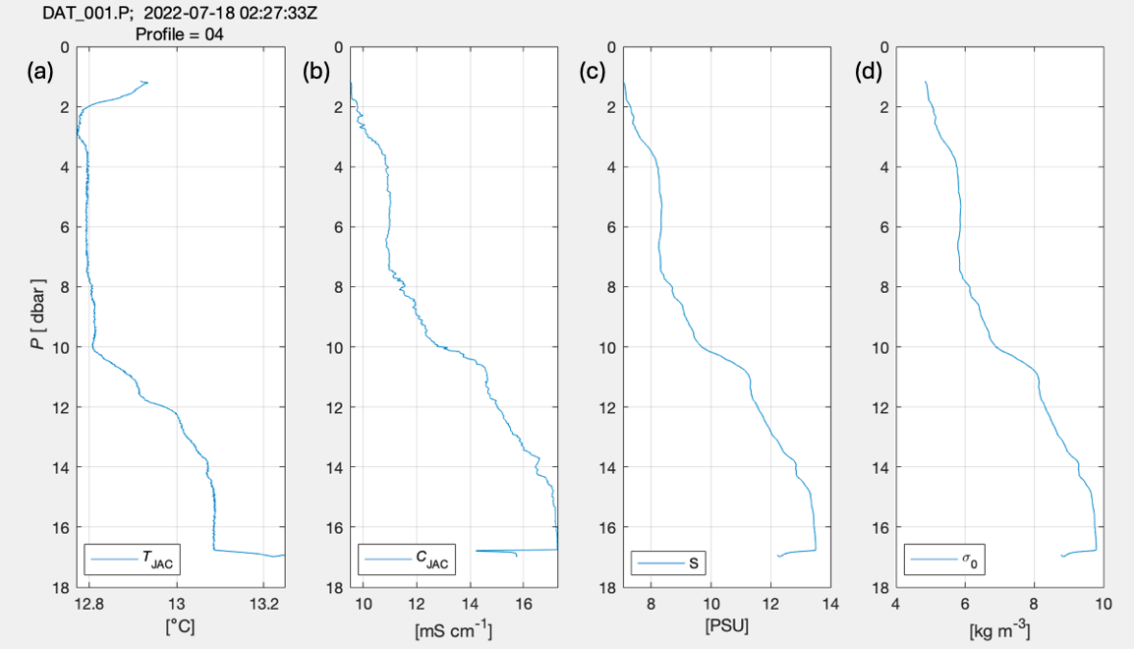


Figure 4: Vertical profiles obtained from the conductivity–temperature (CT) sensor (JFE Advantech, JAC). From left to right: (a) temperature, (b) conductivity, (c) salinity, and (d) potential density anomaly (σθ), all shown as functions of pressure.

A.3.4 Spectral Analysis

Spectral estimates are computed over a predefined depth interval specified in the *quick_look.m* call. Spectra are derived from shear probes, vibration sensors, temperature gradients, and micro-conductivity signals, and are presented in both wavenumber and frequency domains (Fig. 5 a,b).

Panel (a) shows the wavenumber spectra. The thick blue and red curves correspond to shear spectra corrected for coherent noise, while the thinner lines represent the uncorrected signals. Triangular markers indicate the upper wavenumber limits used in the integration of the spectra to estimate the turbulent kinetic energy dissipation rate (ϵ). Black curves represent the corresponding Nasmyth spectra for the estimated ϵ values, providing a reference for comparison with the observed spectra. Temperature gradient spectra are also shown and are minimally corrected for the frequency response of the thermistors.

The quality of the spectral estimates is assessed based on the agreement between the observed shear spectra and the expected Nasmyth shape, the consistency between independent shear probes, and the appropriate selection of the upper wavenumber limit used in the integration. Temperature-gradient spectra are interpreted primarily as qualitative indicators of turbulent activity because of uncertainties in thermistor response. Profiles exhibiting excessive noise, poor agreement with theoretical spectra, or strong contamination from vibration are considered unreliable and are excluded from further analysis.

Panel (b) presents the frequency spectra, computed from the measured signals using the processing parameters defined in *ql_info*. Spectra from vibration sensors (e.g., Ax and Ay) are shown as thick lines, while shear and temperature gradient spectra are displayed using the same color scheme as in panel (a). Black curves represent dimensional Nasmyth spectra for the corresponding ϵ values, providing a reference for comparison.

In the frequency domain, shear spectra are not corrected for vibrational contamination, and peaks in the vibration signals are therefore expected to appear in the shear spectra. This representation is primarily used to identify the presence and frequency range of vibration and to assess its impact on the measured shear. Profiles are considered reliable when the shear spectra exhibit a physically consistent shape and are not dominated by vibrational peaks, whereas strong or broadband vibration that propagates into the shear spectra indicates contamination and leads to the exclusion of the affected data.

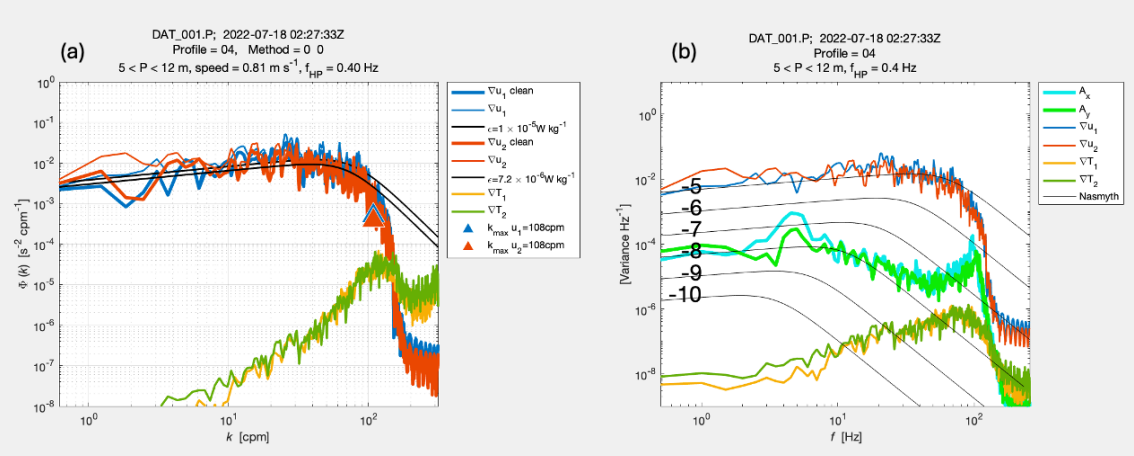


Figure 5: **(a)** Wavenumber spectra and **(b)** frequency spectra obtained from MCTD measurements. In panel (a), shear spectra are shown in blue and red, with thick lines indicating signals corrected for coherent noise and thin lines representing uncorrected spectra. Triangular markers denote the upper wavenumber limits used in the integration for ϵ estimation. Black curves represent theoretical Nasmyth spectra for the corresponding dissipation rates. In panel (b), vibration sensor spectra are shown as thick lines, while shear and temperature gradient spectra follow the same color scheme as in panel (a).

A.3.5 Turbulent Kinetic Energy Dissipation Rate (ϵ)

The turbulent kinetic energy dissipation rate (ϵ) is estimated from shear probe measurements over successive time intervals of length *diss_length*, with overlap between adjacent estimates defined by the *overlap* parameter. Each estimate is obtained from the integration of multiple spectral calculations, based on segments of length *fft_length*.

The *quick_look.m* function displays the resulting vertical profile of ϵ. Independent estimates from the two shear probes (ϵ_1 and ϵ_2) are expected to be in close agreement, with consistent profiles indicating reliable measurements (Fig. 6).

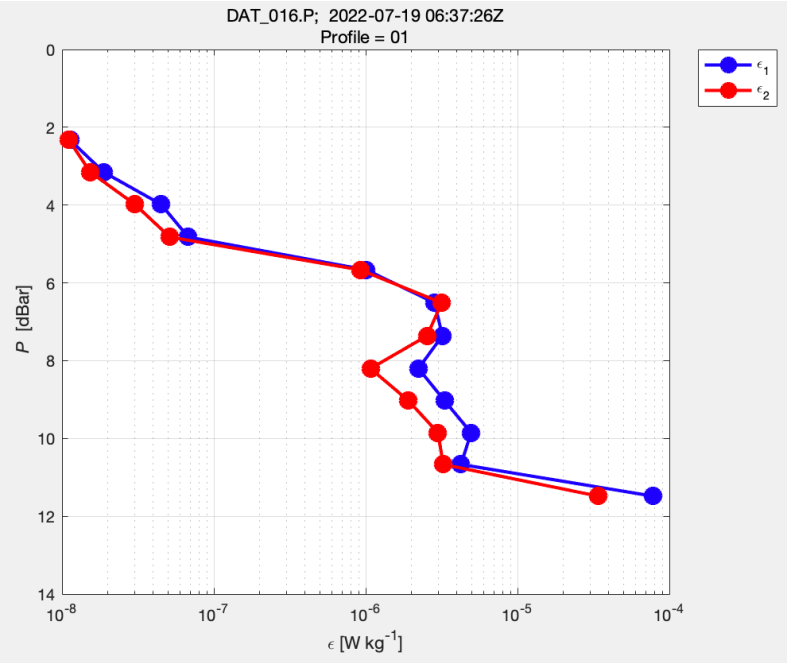


Figure 6: Vertical profile of the turbulent kinetic energy dissipation rate (ϵ) estimated from shear probe measurements. Independent estimates from the two probes (ϵ_1 and ϵ_2) are shown in blue and red, respectively; close agreement between the two indicates good data quality.

A.4 Microstructure Processing and ϵ Estimation

After quality control and the removal of invalid data, the profiles are processed to estimate the turbulent kinetic energy dissipation rate (ϵ).

The microstructure processing is based on MATLAB routines developed by Schettini (2021), which implement a standardized workflow for converting raw MCTD data into dissipation estimates. These routines are publicly available at https://doi.org/10.5281/zenodo.15442937.

The main script (*MicroCTD_Guto_RawDataExtractor.m*) processes all *.P files in the working directory and generates one output per profile, saving the resulting data structure in the same directory. The MATLAB processing produces formatted datasets that are subsequently used as input for the Python-based workflow.

A.5 Data Integration and Synchronization with ADCP Measurements (Python)

Following MATLAB processing, all datasets are handled within a Python environment, where the analysis is organized into modular scripts following the methodology described in Barros (2026). These routines are publicly available at https://doi.org/10.5281/zenodo.18974391.

The objective of this stage is to integrate MCTD and ADCP datasets into a consistent dataset, enabling a combined analysis of velocity, stratification, and turbulence.

A.5.1 Processing Steps

MCTD and ADCP data require synchronization in both space and time prior to analysis. ADCP raw data are initially exported from WinRiver II in ASCII format and pre-processed following the procedures described in Schettini (2021), as detailed in the corresponding processing guide: (https://github.com/GutoSchettini/Ocean-Data-Analysis-Python/blob/main/notebooks/14_ADCP_RDI_vessel_mounted_processing.ipynb).

The MCTD data, previously processed in MATLAB, are then imported into Python and reformatted to ensure compatibility with the ADCP dataset. The two datasets are subsequently synchronized, resulting in a unified dataset suitable for joint analysis.

The workflow is implemented through a sequence of Jupyter notebooks, which should be executed in the following order:

- **STEP1_MCTD_Preprocessing.ipynb**

  Purpose: Imports MCTD data (MATLAB *.mat files) and performs initial preprocessing prior to synchronization.
- **STEP2_ADCP_Preprocessing.ipynb**

  Purpose: Imports ADCP data (ASCII format from WinRiver II) and performs preprocessing and quality control.

- **STEP3_DRIFT_sync_MCTD+ADCP.ipynb**

  Purpose: Synchronizes MCTD and ADCP datasets in space and time, producing a unified dataset and enabling the calculation of derived turbulent parameters.

A.6 Computation of Derived Parameters and Visualization

A.6.1 Computation of Derived Parameters

The final notebook, *STEP3_DRIFT_sync_MCTD+ADCP.ipynb*, is also used to compute derived turbulence and mixing parameters, including:

• S^2 (shear)
• N^2 (buoyancy frequency)
• Ri (Richardson number)
• ϵ (TKE dissipation rate)
• Az (vertical eddy viscosity)
• Reb (buoyancy Reynolds number)

In addition, two supplementary notebooks were developed to compute other parameters used in Barros et al. (2026):

- **STEP4_Calc_Froude.ipynb**

  Purpose: Computes the internal Froude number (requires outputs from Steps 1–3).

- **STEP5_Calc_Transect_areas.ipynb**

  Purpose: Computes transect areas along the channel thalweg (requires outputs from Steps 1–3).

A.6.2 Data Visualization

To avoid unintended modification of previously processed datasets, a dedicated notebook was developed exclusively for data visualization:

- **STEP6_PlottingFigures.ipynb**

  Purpose: Provides a controlled environment for visualizing processed variables without altering the original analysis outputs, allowing for the exploration of different graphical representations, color schemes, and figure layouts used in the manuscript.

A.7 Reproducibility and Data Availability

A.7.1 Reproducibility

All processing scripts and analytical procedures were designed to ensure reproducibility. The complete codebase used in this study is publicly available at https://doi.org/10.5281/zenodo.18974391 and https://github.com/debora-barros.

This structure allows users to reproduce the full processing chain, from raw MCTD data to final turbulence estimates and figures.

A.7.2 Data Access

The data used in this study are available as follows:

- **Input data**: Additional input files required to run the notebooks are available within the repository.
- **MCTD and ADCP data**: Due to file size limitations, the raw MCTD and ADCP datasets are not publicly hosted. Access to these data can be requested for reproducibility purposes by contacting: debor@furg.br.